Micro-hydrodynamics of deformable objects

by

Nobuhiko Watari

A dissertation submitted in partial fulfillment
of the requirements for the degree of
Doctor of Philosophy
(Macromolecular Science and Engineering)
in The University of Michigan
2011

Doctoral Committee:

Professor Ronald G. Larson, Chair
Professor Mark A. Burns
Professor Michael J. Solomon
Professor Shuichi Takayama

TABLE OF CONTENTS

LIST OF FIGURES v

LIST OF TABLES xii

CHAPTER

I. Introduction 1

II. Simulation of DNA Motion in a Microchannel Using Stochastic Rotation Dynamics 7

2.1 Introduction 7
2.2 The model 8
2.2.1 SRD for pure solvent 8
2.2.2 Hybrid MD/SRD method 10
2.2.3 Boundary conditions 12
2.2.4 Simulation parameters 14
2.3 Validation of the method 14
2.3.1 Flow of solvent 14
2.3.2 Motion of a DNA molecule in a solvent 15
2.4 Migration of DNA in a microchannel 17
2.5 Conclusion 18
2.6 Appendix A: time evolution of Couette and Poiseuille flow . . 19
2.6.1 Transient Couette flow 19
2.6.2 Transient Poiseuille flow 19

III. Fluidic trapping of deformable polymers in micro-flows . . . 32

3.1 Introduction 32
3.2 Method 33
3.2.1 Taylor vortex flow 33
3.2.2 Brownian dynamics 34
3.3 Results 35

3.3.1 Trapping in a Taylor vortex flow 35
3.3.2 Effect of hydrodynamic interactions 37
3.3.3 Trapping in an electro-osmotic flow 38
3.4 Summary and Discussion 40
3.5 Appendix: Brownian Dynamics with Hydrodynamic Interactions 41

IV. Conformation Dependence of DNA Electrophoretic Mobility in a Converging Channel 52

4.1 Introduction 52
4.2 Materials and Methods 54
4.2.1 Experimental observation and measurement 54
4.2.1.1 Fabrication of the converging channel . . 54
4.2.1.2 Electrophoresis setup 55
4.2.1.3 Measurement of electrophoretic mobility 56
4.2.2 Theoretical modeling 57
4.2.2.1 A shish-kebab model 57
4.2.2.2 Model for a flexible molecule 59
4.3 Results and Discussion 66
4.3.1 Experimental results 66
4.3.2 Theoretical results 68
4.3.2.1 Electrophoretic mobilities of linear, U-shaped and W-shaped DNA 68
4.3.2.2 Comparison with the experiment 69
4.4 Concluding remarks 69
4.5 Appendix 70
4.5.1 Brownian Dynamics Simulations 70

V. The hydrodynamics of a run-and-tumble bacterium propelled by polymorphic helical flagella 77

5.1 Introduction 77
5.2 Methods 79
5.3 Results 82
5.4 Discussion 85
5.5 Appendix A 86

VI. Efficient models for micro-swimmers 96

6.1 Introduction 96
6.2 Simulation method 98
6.3 Migration speed of three-bead swimmer 100
6.4 Dipolar-flow strength of three-bead swimmer 101
6.5 Rate of energy consumption of three-bead swimmer 103
6.6 Multi-dimensional swimmers 105

6.7 Summary and future directions 108
6.8 Appendix A: Analytical Expressions for the Migration and the Dipolar-Flow Strength Induced by a Small Rectangular Cycle 109
6.9 Appendix B: Most Energy Efficient Cycle Motion of Three Bead Swimmer 111

VII. Shear-induced chiral migration of particles with anisotropic rigidity 123

7.1 Introduction 123
7.2 Method 123
7.3 Results 125
7.4 Summary 129

VIII. Summary and Future Work 137

BIBLIOGRAPHY 140

LIST OF FIGURES

Figure

2.1 Simulation system (drawn two-dimensionally, although we consider a three dimensional system). SRD particles are distributed in a cubic box of dimensions $L_s \times L_s \times L_s$. Collision processes are implemented in each SRD cell bounded by dotted lines which has a volume $a \times a \times a$. A DNA molecule is modeled with a chain with beads(stippled circles) and springs connecting them. Gray cells represent *wall-cells* which define the geometry of the wall. 21

2.2 The time evolution of Poiseuille flow. The symbols represent the results of the SRD simulation at each time and the lines represent the analytical solution at each time. 22

2.3 The time evolution of plane Couette flow. The symbols represent the results of the SRD simulation at each time and the lines represent the analytical solution at each time. 23

2.4 Flow in a *porous medium*. The acceleration of gravity 0.04 [a/τ^2] is induced in the y-direction in a system of size $30[a] \times 30[a] \times 30[a]$. . 24

2.5 Cavity flow. The left wall (the gray part of the boundary) moves in the y-direction at a velocity $0.8[\tau/\mathrm{a}]$ in a system of size $30[a] \times 30[a] \times 30[a]$. The thickness of side walls is $4[a]$. The Reynolds number is about 18. 25

2.6 The dependence of the radius of gyration(R_g) calculated using the hybrid MD/SRD method on the number of DNA beads N. Since we kept $R_0 = 2.44[a]$ constant, the number of beads is proportional to the contour length of the DNA as: $L = (N-1)R_0$. The symbols denote the results of simulations and the dotted line represents $R_g \propto N^{0.588}$, predicted by the Zimm model for a good solvent. 26

2.7 The dependence of the diffusion constant(D) of the DNA center-of-mass calculated using the hybrid MD/SRD method on the number of DNA beads N. The solid line is the prediction of the Zimm theory for a good solvent which is obtained using the values of R_g in Fig. 2.6. The dotted line represents the fitted line $D \propto N^{-0.588}$ to the simulation results. 27

2.8 Relaxation of mean-square of DNA stretch from an extended state. 28

2.9 The same as Fig. 2.6, for the relaxation time of (τ_p). The dotted line represents $\tau_p \propto N^{-0.588}$, predicted by the Zimm model for a good solvent. 29

2.10 Probability distribution of a DNA molecule of contour length 22.0[a] (10 beads) in Poiseuille flow between two parallel planes as a function of distance normal to the planes . Here, x is distance from a plane and W is the distance between two parallel planes. Due to the symmetry, only half of the distribution profile is shown. 30

2.11 The same as Fig. 2.10, except for a molecule with 20 beads(contour length 44.0[a]). 30

2.12 Relation between the Weissenberg number(Wi) and σ^2: the variance of the probability distribution of DNA around the center of the channel. 31

2.13 Relation between the Weissenberg number(Wi) and average DNA stretch. 31

3.1 Taylor vortex flow field. Drawn for the region $(x, y) = ([0, \alpha], [0, \alpha])$. The velocity component of z direction is always zero. 42

3.2 A stretch history of a polymer molecule in a Taylor vortex flow with $A\alpha = 2.0[l/\tau]$, $\alpha = 12[l]$ (top). The polymer takes two states: the trapped state (left bottom) and the tumbling state (right bottom). The polymer molecule has contour length $L = 21[l]$ (10 beads) and the stretch is defined as the largest distance between any two beads in a molecule. 43

3.3 Relationship between mean trap time of a polymer molecule and the normalized magnitude of flow field A. Here, τ_p is the relaxation time of the polymer, and α/L represents the ratio of the wavelength of the Taylor vortex flow (i.e. 2×vortex size) to the contour length of the polymer molecule. Data denoted by (+) symbols were obtained by BD simulations with hydrodynamic interactions, and others by free-draining BD simulations. Error bars indicate the standard errors. In the inserted figure, the trap ratio, which is the fraction of time a molecule is trapped, is shown for $A\tau_p/\alpha = 0.7$. 44

3.4 Local force balance along a curved polymer molecule under fluidic stretching: the spring forces (black arrows) balance the drag forces exerted on beads by a solvent flow(grey arrows) 45

3.5 Examples of stable conformations of polymer molecules in Taylor vortex flow for $A\alpha = 8.0[l/\tau]$ and $\alpha = 12[l]$. The number of beads is 10 in the top figure, 13 in the middle and 19 in the bottom. 46

3.6 The magnitude of flow perturbation velocity field ($\boldsymbol{V}_{\mathrm{HI}}(x, y)$) induced by hydrodynamic interactions in the x-y plane at $z = 0$, where a polymer molecule is trapped. The directions of the x and y axes are the same as in Fig. 3.4 with respect to the conformation of the trapped polymer, and the origin $(x, y) = (0, 0)$ is set to be the center-of-mass of the trapped polymer. Note that, in this plane, the flow perturbation velocity doesn't have z-component and has only in-plane components. 47

3.7 The z-component of the flow perturbation velocity field ($V_{\mathrm{HI},z}(x, y)$) in the $z = 1$ plane (top) and $z = 3$ (bottom) induced by hydrodynamic interactions from a polymer trapped in the $z = 0$ plane. The directions of the x, y axes and the origin are chosen as in Fig. 3.6. A positive $V_{\mathrm{HI},z}$ indicates a velocity away from the z=0 plane, where the trapped polymer resides. 48

3.8 Four configurations of two closely trapped polymers (bottom), and the z-component of the relative velocities of the two centers-of-mass $V_{12,z}$ induced by hydrodynamic interactions for each configurations (top). r_{12} is the distance between the centers-of-mass. Note that a positive $V_{12,z}$ corresponds to chains moving away from each other. . 49

3.9 Steady-state conformation of a trapped polymer in an electro-osmotic flow in a channel whose surfaces bear a sinusoidally varying charge: $\sigma^{\pm}(y) = \sigma_0 \cos(qy + \pi/4)$, where σ_0 was chosen to satisfy $\mu_0 E_y = 7.0[l/\tau]$, and $q = 2\pi/(2h)\,[l^{-1}]$, $h = 6.0[l]$. The contour length of the polymer is $L = 21[l]$ (10 beads). 50

3.10 The center-of-mass distribution marked as dark shading (left) and history of the center-of-mass position in x-direction (right) of a polymer molecule in an electro-osmotic flow in a channel whose surfaces bear a charge varying sinusoidally plus a net charge: $\sigma^{\pm}(y) = \sigma_0 \cos(qy + \pi/4) + \sigma_{\rm net}$, where σ_0 and $\sigma_{\rm net}$ were chosen to satisfy $\mu_0 E_y = 4.0[l/\tau]$ and $\mu_{\rm net} E_y = 2.0[l/\tau]$, and $q = 2\pi/(2h)\,[l^{-1}]$, $h = 10[l]$. The contour length of the polymer is $L = 63[l]$ (30 beads). . 51

4.1 (A) Schematic diagram of the microscale converging channel. (B) The calculated electric field and electric field gradient along the converging channel central line. 72

4.2 (A) Schematic diagram of shish-kebab model. (B) A freely jointed chain consisting of multiple charged "shish-kebab" segments. . . . 73

4.3 (A) Histogram of EP mobility for stretched and unstretched DNA. (B) Distribution of EP mobility versus DNA visual length. Each symbol type represents one tracked DNA molecules. 74

4.4 Distribution of EP mobility versus visual length for five DNA conformations. The fully stretched length of the DNA is around 20 μm. Different symbols correspond to DNA shapes depicted in the figure legend. (Circle: coiled, square: oval, triangle pointed upward: folded, rotated triangle pointed to the right: half-dumbbell, and diamond: extended). The three dashed lines mark three different unraveling paths typically taken by the molecules. The circled points correspond to "wiggling" conformations; see discussion in the text. 75

4.5 Theoretical estimation of the enhancement of the DNA EP mobility by stretching. Note that both μ_0 and μ_1 are negative for DNA. We expect $\mu_1 = \mu_0/4$ when $\kappa a \lesssim 1$. 76

5.1 The geometry of *E. coli* with flagella of the normal state and the discretized model. b is half the length of the long axis of the body, which is the unit length scale in our simulation, and is typically 1μm for *E. coli*. Gray open circles in the diagram of the body represent the positions of first bead of each flagellum attached by a hook. . . 88

5.2 (Top) the model of a hook and the distribution of the torques from the action of a rotary motor. (Bottom left) the decomposition of a torque $\boldsymbol{T}_{\rm tot}$ into two torques $\boldsymbol{T}_{\rm a}$ and $\boldsymbol{T}_{\rm b}$, each of which is perpendicular to a spring. (Bottom right) the decomposition of a torque $\boldsymbol{T}_{\rm c}$ into a force couple $\boldsymbol{F}_{\rm c}$ and $-\boldsymbol{F}_{\rm c}$, with which $\boldsymbol{T}_{\rm c} = \boldsymbol{r}_{\rm c} \times \boldsymbol{F}_{\rm c}$ is satisfied. . . . 89

5.3 Typical trajectory of a modeled cell in run-and-tumble motion (left) and snapshots of cell conformations in different states during the motion (right). The red line in the trajectory represents a run state and the blue line a tumble state. The trajectory contains runs for 1200τ each and tumbles for 800τ each, the latter of which each consists of a semicoiled state for 400τ and a curly 1 state for 400τ. 90

5.4 Time-averaged flow field around a modeled cell in a run. In this figure and Fig. 5.7, red arrows points into the paper and blue arrows the opposite. All arrows are unit flow-velocity vectors. In the near-field flow, all the shown velocity vectors have actual magnitude of velocity larger than $4.0\times10^{-5}\ b/\tau$. The far-field recovers the dipole flow (left), which is induced by a force dipole generated by the thrust from the rotating helical flagella and the drag force on the cell. 91

5.5 Streamlines implied by the near-field flow in Fig. 5.4. 92

5.6 The decay of the magnitude of the time-averaged flow velocity v with distance. r is the distance from the center-of-mass $\boldsymbol{r}_{\rm cm}$ to a point on a plane that is perpendicular to the swimming axis and contains $\boldsymbol{r}_{\rm cm}$. 93

5.7 Time evolution of the flow field near a modeled cell. All arrows are unit flow-velocity vectors, each of whose actual magnitude of velocity is larger than $1.6\times10^{-3}\ b/\tau$. The period of rotation of the flagellar bundle around the swimming axis is approximately 10.4τ. 94

5.8 Time-averaged flow field around a modeled cell in a run near a wall. The cell and the shown velocity field are $2.7b$ away from the wall. Red arrows point toward the wall and blue arrows the opposite. . . 95

6.1 Minimal models of one-, two- and three-dimensional micro-swimmers and the cycle histories. *Chrysomonad* and sea urchin spermatozoon are examples of one-dimensional puller and pusher, respectively. Note that tumbling is induced in the 2D- and 3D-swimmers by holding the equilibrium lengths of one (2D) or three (3D) bond-lengths fixed while varying the lengths of the other bonds. 113

6.2 (color online). Contour plot of function $g(a, L_1, L_2)$ in Eq. 6.7. . . . 114

6.3 The top three figures illustrate that since in Stokes flow no net migration is produced by any bead motions that merely reverse themselves, the migration in any single cycle can be obtained as the sum of the migrations in two cycles into which the original cycle is divided. Extending this principle, the bottom figure illustrates that the migration in a cycle of arbitrary shape approaches that of the sum of migrations in small rectangular cycles into which the original cycle is divided. 115

6.4 The migration per cycle for a CCW circular cycle centered at $(L_1, L_2) = (5a, 5a)$ with radius $0.5a < R_c < 3a$, obtained from Eq. 6.7 (Theory), simulations with the Oseen tensor and the RPY tensor. 116

6.5 (color online). Contour plot of function $h(a, L_1, L_2)$ in Eq. 6.10. . . 117

6.6 The strength of dipole flow, p_c, for a CCW circular cycle with radius $0.5a$ and centered at $(L_1, L_2) = (L_1^c, 5a)$ where $2a < L_1^c < 20a$, obtained from Eq. 6.7 (Theory), simulations with the Oseen tensor and the RPY tensor 118

6.7 The change of the swimming behaviors by an inversion of the cycle-direction or an exchange of L_1 and L_2. 119

6.8 (Top) the configuration of the five-bead model. (Middle) the torque distribution on the swimmer. (Bottom) a decomposition of a torque $\boldsymbol{T}_{\rm tot}$ on three connected beads, which represents either $\boldsymbol{T}_1$, $\boldsymbol{T}_2$, $-\boldsymbol{T}_1$ or $-\boldsymbol{T}_2$ in the middle figure, into two torques $\boldsymbol{T}_a$ and $\boldsymbol{T}_b$ acting perpendicular to adjacent bonds. 120

6.9 (color online). The time-averaged flow field around a three-bead pusher (top), around a five-bead pusher (middle) and around a detailed bead-spring model of *E. coli* in a run [1] (bottom). All arrows are unit flow-velocity vectors. Red (or light gray) arrows point into the paper, blue (or dark gray) arrows the opposite, and black arrows only have in-plane velocities. Swimming is from left to right. . . . 121

6.10 A trajectory of the five-bead swimmer near a wall. The trajectory is projected onto the wall to show the radius of the circular motion. The swimmer is initially placed $2R$ away from and parallel to the wall. Simulation parameters are a=$0.2R$, δ=$0.5R$, t_0=2.0τ, H=$1000T/R$, $k_{\rm b}$=$2000T$, $\theta_{\rm e}$=160° and Δt=$10^{-3}\tau$. 122

7.1 The ten distinguishable tetrumbbell structures constructed from four beads and six springs, each of which is either a hard (H, solid line) or soft (S, dotted line) spring. 131

7.2 History of the center-of-mass position of tetrumbbell (2b) of migration type M in the vorticity direction (R_z^{cm}). The shear rate is changed from $\Pi_s = 0.02$ to $\Pi_s = -0.02$ at time $t/\tau = 10000$. 133

7.3 History of the conformation change, the migration velocity in the vorticity direction, and the chiral deflection index of tetrumbbell (2b) of migration type M, which corresponds to the migration history in Fig. 7.2. The shear rate is $\Pi_s = 0.02$ for the plots on the left side and $\Pi_s = -0.02$ for those on the right side. The black and white bonds in the figures of the tetrumbbell conformation show the hard and soft springs, respectively. Note that the history of chiral deflection index changes sign upon reversal of the shear direction. In this case, $T_{cycle}/\tau \simeq 670$. 134

7.4 (top) The time-averaged migration velocity $|\Pi_{vz}^{ave}|$ as a function of shear rate Π_s for each type of tetrumbbell. (bottom left) The maximum of the chiral deflection index (χ_{max}) in one cycle of deformation as a function of the shear rate. The solid line has the slope of power of 1. (bottom right) The maximum stretch ratio of soft spring $(Q_{soft}^{max} - L)/L$ in one cycle of deformation as a function of the shear rate. 135

7.5 Sketch of possible migration of a droplet enclosing a solid object in shear flow. 136

LIST OF TABLES

Table

5.1 Parameters for simulations of modeled cell. 87

7.1 Types of shear migration of different tetrumbbell structures. 132

CHAPTER I

Introduction

Micron-size deformable objects in flow show rich and complex dynamics. For example, it is known that DNA molecules migrate toward the center of a channel with $\sim$10 micron width in flow [2]. A swarm of *E.coli*, which are essentially self-propelled deformable particles, induces jets and vortexes in fluid, whose length-scales are much larger than the size of individual cell [3]. Sperm cells, each of which swims by beating its flexible flagellum, synchronize the beating motion through the hydrodynamic interaction between the cells [4]. All of these phenomena result from the strong effect of the micron-scale hydrodynamics, or micro-hydrodynamics. Not only are these phenomena physically interesting, the control over the dynamics of deformable objects in micron-size (cells, bacteria, bio-polymers, droplets, etc.) is becoming practically important as we develop micro-chip for biological applications that may involve bio-polymer manipulations, droplet manipulations, mixing fluids and particle separations in flow. Also, understanding these phenomena leads to a prediction of the hydrodynamics of bacterial swimming and the optimal design of an efficient micro-swimmer. However, such dynamics is not easy to predict because the motion and deformation of the objects strongly couple with the fluid flow surrounding them. For example, when one end of a flexible molecule moves in fluid, the motion induces a flow perturbation that affects the motion of the other part of the molecule, which is called

the hydrodynamic interaction (HI). Therefore, to capture the dynamics in which the deformation and the flow couple, it is essential to take into account the effect of HI between segments of the deformable object (internal HI), between the multiple objects, and the object and the boundary wall if there is any.

In order to address such problems in micro-hydrodynamics, we need a method to deal with 1) the deformability of the object, 2) HI, 3) the boundary, and 4) the Brownian motion (thermal noise). In the following chapters, we show that the bead-spring model with hydrodynamic interactions can successfully simulate the dynamics of a deformable object in fluid.

The bead-spring model first decomposes an object to a series of spherical beads with hydrodynamic radius, connected using potentials that control the shape of object in the equilibrium and the deformability. By choosing the potentials in an appropriate way, we can easily construct a model for a deformable object of an arbitrary shape. A modeled object can deform in an external flow, or in the case of self-propelled object, by torques applied as the action of motors. To capture the dynamics of this modeled object in fluid, we take into account HI between these beads. We employ two different methods depending on the boundary condition of the problem to account for the HI, i.e. using 1) HI tensor or 2) Stochastic Rotation Dynamics (SRD).

Using HI tensor, the flow perturbation induced by a bead is analytically described up to order $1/r^3$, where r is the distance from a bead, and the flow perturbation by the motion and deformation of the object becomes the superposition of the perturbations induced by all beads. Moreover, once the HI tensor is found, the Brownian motion can be easily introduced. Also, the analytical expression for the HI tensor accounting for the presence of a planer wall has been derived by Blake [5], and this enables one to study the effect of a boundary wall on the dynamics of the object. However, there is no simple analytical HI tensor derived for a boundary condition with more than one wall. Therefore, alternative method to account for HI effect is required when we

have more than one wall or more complex boundary, such as a micro-channel with contractions.

For simulations with an arbitrary geometry of the boundary, we employ SRD to compute the fluid perturbations induced by the motion and deformation of the object under the presence of the boundary. SRD is a particle-based method and a set of fluid particles represents the fluid motion, including the thermal fluctuations. A deformable modeled object exchanges its momentum with this SRD particles, so that the dynamics of the object couples with the fluid motion. SRD has recently been applied for various systems such as the colloidal suspensions [6], polymer solution [7] and vesicles under flow [8]. In our study, we generalize the SRD algorithm to apply to the cases of complex boundary conditions.

By employing HI tensors or SRD method, we can compute the coupling of motion and deformation of deformable objects with fluid motion, which leads to un-explored realm in the micro-hydrodynamics.

In the following chapters, theoretical and computational analyses on these five phenomena will be discussed:

- DNA migration toward the center of micro-channels in flow (Chapter II)
- DNA trapping in a flow with micro-vortexes (Chapter III),
- conformation dependency of DNA electrophoretic mobility (Chapter IV),
- modeling of multiply flagellated bacteria (Chapter V),
- simplified models for micro-swimmers (Chapter VI),
- shear-induced migration of deformable particles (Chapter VII).

In Chapter II, we discuss the simulation of a DNA molecule in a micro-channel with two parallel walls. Since we have two walls, the HI tensor cannot be easily derived analytically for this system. Therefore, we employ SRD to account for the HI effect

on a DNA molecule in flow in the channel. We propose a method to simulate the DNA motion in micro-channels of complex geometry, which based on Stochastic Rotation Dynamics (SRD) using a new scheme for the boundary condition. The method enables us to define a boundary wall of arbitrary shape and to describe a wall moving at an arbitrary velocity. As an application, we simulate the motion of DNA in Poiseuille flow between two parallel planes and show that DNA molecules tend to concentrate near the center of the channel in agreement with experimental results.

In Chapter III, we report that a polymer molecule can be trapped spatially and conformationally using a micro-flow that has at least two stagnation points (or two points with equal velocity) and a net flow orthogonal to the line connecting them. Examples include a Taylor vortex flow and an electro-osmotic flow in a channel with surfaces that have a sinusoidal charge. Simulating the motion of a polymer molecule in these flows using Brownian dynamics, we find that such flows produce a curved polymer conformation, leading to an elastic force that drives migration against the flow, thus stabilizing this conformation. Simulations with hydrodynamic interactions confirm these predictions and show that there exists a repulsive interaction between two trapped polymers.

In Chapter IV, we report that the electrophoresis of λ-DNA is observed in a micron-scale converging channel where the center-of-masses trajectories of DNA molecules are tracked to measure instantaneous electrophoretic (EP) mobilities of DNA molecules of various stretch lengths and conformations. Contrary to the usual assumption that DNA mobility is a constant, independent of field and DNA length in free solution, we find DNA EP mobility varies along the axis in the contracting geometry. We correlate this mobility variation with the local stretch and conformational changes of the DNA, which are induced by the electric field gradient produced by the contraction. A "shish-kebab" model of a rigid polymer segment is developed that consists of aligned spheres acting as charge and drag centers. The electrophoretic mobility of

the shish-kebab is obtained by determining the electrohydrodynamic interactions of aligned spheres driven by the electric field. Multiple shish-kebabs are then connected end-to-end to form a freely jointed chain model for a flexible DNA chain. DNA electrophoretic mobility is finally obtained as an ensemble average over the shish-kebab orientations that are biased to match the overall stretch of the DNA chain. Using physically reasonable parameters, the model agrees well with experimental results for the dependence of electrophoretic mobility on stretch and conformation. We find that the magnitude of the electrophoretic mobility increases with DNA stretch, and that this increase is more pronounced for folded conformations. Note that this chapter is based on the collaboration study with James Lee group in Ohio State University, and all the experimental works had been conducted by the group.

In Chapter V, in order to study the swimming of a peritrichous bacterium such as *Escherichia coli*, which is able to change its swimming direction actively, we simulate the "run-and-tumble" motion using a bead-spring model to account for the hydrodynamic and the mechanical interactions between the cell body and multiple flagella, the reversal of the rotation of a flagellum in a tumble and the associated polymorphic transformations of the flagellum. The cell body and each flagellum are connected by a flexible hook, so that the flagella can take independent orientations with respect to the cell body. This simulation reproduces the experimentally observed behaviors of *E. coli*, namely, a three-dimensional random-walk trajectory in run-and-tumble motion and steady clockwise swimming near a wall. We show that the polymorphic transformation of a flagellum in a tumble facilitates the reorientation of the cell, and that the time-averaged flow field near a cell in a run has double-layered helical streamlines, with a time-dependent flow magnitude large enough to affect the transport of surrounding chemoattractants.

In Chapter VI, we propose minimal models of one-, two- and three-dimensional microswimmers at low Reynolds number with a periodic non-reciprocal motion. These

swimmers are either "pushers" or "pullers" of fluid along the swimming axis, or combination of the two, depending on the history of the swimming motion. We show this with a linear three-bead swimmer by analytically evaluating the migration speed and the strength of the dipolar flow induced by its swimming motion. It is found that the distance traveled per cycle and the dipolar flow can be obtained from an integral over the area enclosed by the trajectory of the cycle projected onto a cross-plot of the two distances between beads. Two- and three-dimensional model swimmers can tumble by breaking symmetry of the swimming motion with respect to the swimming axis, as occurs in the tumbling motion of *Escherichia coli* or *Chlamydomonas*, which desynchronize the motions of their flagella to reorient the swimming direction. We also propose a five-bead model of a "corkscrew swimmer", i.e. with a helical flagellum and a rotary motor attached to the cell body. Our five-bead swimmer is attracted to a nearby wall, where it swims clockwise as observed in experiments with bacteria with helical flagella.

In Chapter VII, we report that an achiral particle with anisotropic rigidity can migrate in the vorticity direction in shear flow. A minimal "tetrumbbell" model of such a particle is constructed from four beads and six springs to make a tetrahedral structure. A combination of two different spring constants corresponding to "hard" and "soft" springs yields ten distinguishable tetrumbbells, which when simulated in shear flow with hydrodynamic interactions between beads but no Brownian motion at zero Reynolds number, produces five different types of behavior in which seven out of ten tetrumbbell structures migrate in the vorticity direction due to shear-induced chirality. Some of the structures migrate in the same direction along the vorticity direction even when the shear flow is reversed, which is impossible for permanently chiral objects.

CHAPTER II

Simulation of DNA Motion in a Microchannel Using Stochastic Rotation Dynamics

2.1 Introduction

The dynamics of DNA in confined geometries is an important problem in designing devices to separate DNA in microchannel [9–11]. The motion of DNA is different from that in the unbound space. For example, Fang et al. [12] observed that DNA molecules migrate away from a plane wall in shear flow. In order to explain such behavior and to predict the DNA motion in microchannels, it is essential to take into account of the hydrodynamic interaction properly.

In the simulation of the Brownian motion of polymers, the conventional way of taking into account of the hydrodynamic interaction(HI) is to use the HI tensor such as the Oseen tensor. Extensive studies have been carried out to account for the effect analytically and by simulation [13–15]. This approach, however, encounters a difficulty when the DNA is placed in microchannels since the HI tensor cannot be obtained analytically. Jendrejack et al. evaluated the HI tensor using FEM method and succeeded to reproduce the migration of DNA in a microchannel with square cross section [2]. However, this method is computationally expensive to be used to simulate DNA in more complex geometries.

In order to conduct the simulation more efficiently, we have developed a code based on the Stochastic Rotation Dynamics(SRD) for dilute DNA solutions in arbi-

trary geometries . SRD was introduced by Malevanets and Kapral [16] and is also called multiparticle-collision dynamics (MPCD). It is a particle based method and a set of fluid particles(we call them SRD particles) represents the fluid motion. SRD has recently been applied for various systems such as the colloidal suspensions [6], polymer solution [7] and vesicles under flow [8]. The advantages of SRD in comparison with methods such as lattice Boltzmann and dissipative particle dynamics have been discussed by Padding et al. [6].

In this paper, we will generalize the SRD algorithm to apply to the cases of complex boundary conditions. First, we will explain our algorithm and show several examples to demonstrate its validity. Then, we will apply the method for the DNA motion in a channel.

This paper is constructed as follows. In section 2.2, the algorithm of our method is explained. In section 2.3, the algorithm is tested for simple cases. In section 2.4, the method is applied to DNA in Poiseuille flow between two parallel planes.

2.2 The model

In this section, we present the SRD algorithm for simulating a DNA molecule in the presence of a boundary of arbitrary shape.

2.2.1 SRD for pure solvent

First, we consider the situation that there is no DNA and discuss how to determine the fluid motion by SRD. In the simulation system, the space is divided into cubic cells of size $a \times a \times a$ and the macroscopic quantities such as the local fluid velocity and the local temperature are determined for each cell. The fluid motion in each cell is described by the SRD particle, each of which has mass m, position vector $\mathbf{r}_i$ and velocity vector $\mathbf{v}_i$. The fluid velocity in a cell is given by the center-of-mass velocity

of the SRD particles in the cell:

$$\mathbf{v}_{cell} = \frac{\sum_{i \in cell} \mathbf{v}_i}{N_{cell}}, \tag{2.1}$$

where $\sum_{i \in cell}$ means the summation of the SRD particles in the cell and $N_{cell} = \sum_{i \in cell}$ is the number of SRD particles in the cell. Also, the local temperature is determined by:

$$k_B T_{cell} = \frac{\sum_{i \in cell} m \left(\mathbf{v}_i - \mathbf{v}_{cell}\right)^2}{3(N_{cell} - 1)}, \tag{2.2}$$

where k_B is the Boltzmann constant. Time evolution of SRD particles is calculated by two steps, the streaming step and the collision step.

- streaming step

  This step displaces each SRD particle according to:

  $$\mathbf{r}_i(t + \delta t) = \mathbf{r}_i(t) + \mathbf{v}_i(t)\delta t. \tag{2.3}$$

  Here, δt is the time interval of a discrete time in the simulation.

- collision step

  This step exchanges the momenta of SRD particles. First, the center-of-mass velocity $\mathbf{v}_{cell}$ is calculated for all cells, and then the velocities of the particles in an SRD cell are changed according to the following equation:

  $$\mathbf{v}_i(t + \delta t) = \mathbf{v}_{cell(i)}(t) + \mathcal{R} \cdot (\mathbf{v}_i(t) - \mathbf{v}_{cell(i)}(t)), \tag{2.4}$$

  where $\mathbf{v}_{cell(i)}$ indicates the center-of-mass velocity of the cell in which the particle i is, and $\mathcal{R}$ is a random rotation matrix which satisfies $\mathcal{R} \cdot \mathcal{R}^\dagger = \boldsymbol{I}$. The matrix $\mathcal{R}$ stands for the effect of collision among the SRD particles: Eq. (2.4) represents the velocity change which keeps the local momentum and the local

energy conserved. In practice, $\mathcal{R}$ is chosen to be the rotation matrix around a randomly chosen axis with the fixed angle α.

In addition to these two processes, an operation called grid-shift was introduced to facilitate the transfer of momentum between neighboring particles [17]. In this operation, the grid defining the cells is shifted by a random vector whose components is randomly chosen from the interval $[-a/2, a/2]$, and the collision operation is performed in the cell defined by the shifted grid.

The SRD particles were initially placed randomly in the system with an average number ρ per a cell. To set the temperature to assigned value T, each velocity component is taken from a uniform distribution $[-\sqrt{3k_BT/m}, \sqrt{3k_BT/m}]$.

The transport properties in SRD simulations have been well investigated [18, 19]. It is known that the viscosity is given by:

$$\eta = \eta_{\rm kin} + \eta_{\rm col} \tag{2.5}$$

with

$$\eta_{\rm kin} = \frac{\rho k_B T \delta t}{a^3} \left[\frac{5\rho}{(\rho - 1 + e^{-\rho})\,(4 - 2\cos\alpha - 2\cos 2\alpha)} - \frac{1}{2} \right], \tag{2.6}$$

$$\eta_{\rm col} = \frac{m(1-\cos\alpha)}{18 a \delta t} \left(\rho - 1 + e^{-\rho}\right), \tag{2.7}$$

where $\eta_{\rm kin}$ and $\eta_{\rm col}$ stand for the viscosity due to the streaming step and the collision step, respectively. This result has been shown to agree well with the result of SRD simulations.

2.2.2 Hybrid MD/SRD method

Next, we explain how the above dynamics is modified when a DNA molecule is introduced. This method is basically the same as one in Refs. [18] and [20]. We

employed the bead-spring model for the DNA molecule that consists of N beads of mass M and $(N-1)$ springs connecting them. The bead positions $\boldsymbol{R}_p$ and velocities $\boldsymbol{V}_p$ $(p = 1, 2, ...N)$ are changed by the following two steps.

In the first step, the time evolution of $\boldsymbol{R}_p$ and $\boldsymbol{V}_p$ is calculated by the Newton's equation of motion for the beads using the time-reversible velocity Verlet algorithm:

$$\mathbf{R}_p(t + \delta t_{\rm MD}) = \mathbf{R}_p(t) + \delta t_{\rm MD}\mathbf{V}_p(t) + \frac{(\delta t_{\rm MD})^2}{2M}\mathbf{f}_p(t), \tag{2.8}$$

$$\mathbf{V}_p(t + \delta t_{\rm MD}) = \mathbf{V}_p(t) + \frac{\delta t_{\rm MD}}{2M}\left\{\mathbf{f}_p(t + \delta t_{\rm MD}) + \mathbf{f}_p(t)\right\}. \tag{2.9}$$

where $\mathbf{f}_p(t)$ is the force exerted by other beads. The timestep for the solvent δt was chosen to be larger than that of the molecular dynamics timestep for DNA beads $\delta t_{\rm MD}$ to improve the efficiency of the computation.

In the second step, the effect of solvent is taken into account by the following collision step [18, 20]. In the presence of DNA, the center-of-mass velocity of a cell is calculated by:

$$\mathbf{v}_{cell} = \frac{\sum_{i\in cell} m\mathbf{v}_i + \sum_{p\in cell} M\mathbf{V}_p}{\sum_{i\in cell} m + \sum_{p\in cell} M}, \tag{2.10}$$

and the velocity of the SRD particles and that of DNA beads are changed by the same equation as Eq. (2.4):

$$\mathbf{v}_i(t + \delta t) = \mathbf{v}_{cell(i)}(t) + \mathcal{R}\cdot(\mathbf{v}_i(t) - \mathbf{v}_{cell(i)}(t)), \tag{2.11}$$

$$\mathbf{V}_p(t + \delta t) = \mathbf{v}_{cell(p)}(t) + \mathcal{R}\cdot(\mathbf{V}_p(t) - \mathbf{v}_{cell(p)}(t)). \tag{2.12}$$

In Eqs. (2.8) and (2.9), the forces $\mathbf{f}_p(t)$ consists of two parts: the forces by the neighboring springs and the forces by the excluded volume potential. For the spring force, we adopted the worm-like chain(WLC) model [2, 21, 22]. The force acting on

the bead p due to the spring connecting the beads p and q is written as:

$$\mathbf{f}_{pq}^{\mathrm{sp}} = \frac{k_B T}{2b_K} \left\{ \left(1 - \frac{r_{pq}}{R_0} \right)^{-2} - 1 + \frac{4r_{pq}}{R_0} \right\} \frac{\mathbf{r}_{pq}}{r_{pq}}, \tag{2.13}$$

where $\boldsymbol{r}_{pq} = \boldsymbol{R}_p - \boldsymbol{R}_q$, b_K is the Kuhn length of DNA and $R_0 = L/(N-1)$ is the maximum spring length where L is the contour length of DNA. For the force due to the excluded volume potential, we employed the following model [2]:

$$\mathbf{f}_{pq}^{\mathrm{ex}} = -\frac{\partial U_{pq}^{\mathrm{ex}}}{\partial \boldsymbol{r}_{pq}} \tag{2.14}$$

with

$$U_{pq}^{\mathrm{ex}} = \frac{1}{2} v k_B T N_{K,s}^2 \left(\frac{3}{4\pi S_s^2} \right)^{3/2} \exp\left[-\frac{3r_{pq}^2}{4S_s^2} \right], \tag{2.15}$$

where v is the excluded volume parameter, $S_s^2 = N_{K,s} b_K^2/6$ is the radius of gyration of an ideal chain consisting of $N_{K,s}$ Kuhn segments and $N_{K,s}$ is related to the spring length R_0 by $R_0 = N_{K,s} b_K$. The force acting on bead p is $\mathbf{f}_p = \sum_q (\mathbf{f}_{pq}^{sp} + \mathbf{f}_{pq}^{ex})$. Note that Eq. (3.8) corresponds to the case that DNA is in good solvent. The electrostatic forces due to the electric charges of DNA are ignored as they are assumed to be screened by ions.

2.2.3 Boundary conditions

Fig. 2.1 shows an example of the simulation system of DNA placed in a solvent flowing between two walls denoted by gray cells. The whole system is constructed in a simulation box of size $L_s \times L_s \times L_s$ and periodic boundary conditions are imposed at the edges of the simulation box. The wall can be set in an arbitrary shape as they are described by a set of *wall-cells*. At the wall, the non-slip boundary condition is imposed.

To realize the non-slip boundary condition, Lamura et al. [23] used the *bounce-back*

boundary condition. Here, we used a different method. In our method, the velocity of the SRD particle that came into a wall-cell after the streaming step is changed to a random velocity obeying the Gaussian distribution. The mean value and the variance of the velocity $\mathbf{v}_i$ are determined by the velocity and the temperature of the wall. For example, if the wall is stationary at temperature T, $\langle \mathbf{v}_i \rangle = 0$ and $\langle \mathbf{v}_i^2 \rangle = 3k_BT/m$.

Note that, in the above procedure, the SRD particles can go into the wall-cells freely and they exchange energy with the wall. Accordingly, the wall acts as artificial heat generator or absorber. This occasionally caused an anomalous temperature profile. To overcome the problem, we used a thermostat for all cells. The local temperature T_{cell} for the *cell* is given by:

$$k_B T_{cell} = \frac{\sum_{i \in cell} m \left(\mathbf{v}_i - \mathbf{v}_{cell}\right)^2 + \sum_{p \in cell} M \left(\mathbf{V}_p - \mathbf{v}_{cell}\right)^2}{3\left(\sum_{i \in cell} m + \sum_{p \in cell} M - 1\right)}. \tag{2.16}$$

To adjust the local temperature to the system temperature T, we multiplied $(\mathbf{v}_i - \mathbf{v}_{cell})$ and $(\mathbf{V}_p - \mathbf{v}_{cell})$ by the factor $\beta = \sqrt{T/T_{cell}}$. This adjustment is carried out after each streaming step.

Although SRD particles can go into the wall-cells freely, the DNA beads cannot go into the wall-cells. To ensure this, we assumed a repulsive interaction potential between the beads and the wall-cells. Let r be the distance between a bead and the center of a wall-cell, then the bead-wall potential is given by

$$U^{\text{wall}}(r) = \begin{cases} 4\epsilon \left[\left(\frac{\sigma}{r}\right)^{12} - \left(\frac{\sigma}{r}\right)^{6} \right] + \epsilon & (r \leq 2^{\frac{1}{6}}\sigma) \\ 0 & \text{otherwise.} \end{cases} \tag{2.17}$$

To induce a flow in the channel, we consider a hypothetical gravitational acceleration $\mathbf{g}$ on SRD particles that are not in wall-cells, and carried out the following

update after each collision step:

$$\mathbf{v}_i(t+\delta t) = \mathbf{v}_i(t) + \mathbf{g}\ \delta t. \tag{2.18}$$

2.2.4 Simulation parameters

We took a and k_BT as the unit of length and energy, respectively and took $\tau = 20\delta t$ as the unit of time. The unit of mass is then given by $[k_BT \cdot \tau^2/a^2]$.

For parameters for the SRD method we chose: the system size $L = 30[a]$; the average number of SRD particles per cell $\rho = 4[a^{-3}]$; the total number of SRD particles $\rho(L/a)^3 = 4 \times 30^3 = 108\ 000$; the rotation angle of the rotation matrix $\mathcal{R}$, $\alpha = 130°$; the mass of SRD particles $m = 1.0[k_BT \cdot \tau^2/a^2]$. Using this set of parameters, the viscosity of the fluid is evaluated according to the Eq. (2.5) as $\eta = 5.64[k_BT \cdot \tau/a^3]$ and kinetic viscosity $\nu = 1.41[a^2/\tau]$. With these parameters, the Schmidt number of the solvent is about 40.

For parameters for the hybrid MD/SRD method we chose: the MD time increment for DNA motion $\delta t_{\mathrm{MD}} = 0.01[\tau]$ and the mass of DNA beads $M = 4.0[k_BT \cdot \tau^2/a^2]$. For the bead-spring model: the contour length of the portion of the DNA represented by one spring $R_0 = 2.44[a]$, Kuhn length $b_K = 0.14[a]$ and excluded volume parameter $v = 0.012[a^3]$. The parameters for the LJ potential between a bead of the DNA molecule and the boundary wall are set $\sigma = 1.0[a]$ and $\epsilon/k_BT = 1.0$, respectively.

2.3 Validation of the method

In this section, we discuss the result of SRD simulations conducted to test the validity of our algorithm.

2.3.1 Flow of solvent

First, we tested the algorithm for the system without DNA molecule.

Fig. 2.2 shows the velocity profile of a fluid confined between two parallel planes when the fluid is started to be accelerated at time $t = 0$. The velocity profile can be calculated analytically as it is shown in Appendix and the result is shown by the lines in Fig. 2.2. The symbols in the figure shows the result of the SRD simulations. Since the macroscopic velocity $\mathbf{v}_{cell}$ of SRD particles has considerable fluctuations, the velocity shown here is the ensemble average over 100 independent calculations (the same procedure is taken to obtain the velocity profile in the following). In calculating the theoretical curves, we used the viscosity given by Eq. (2.5). Therefore, no fitting parameters are used in comparison between the theoretical solutions and SRD simulations. The figure shows that the result of our simulation agrees well with the theoretical solution.

Fig. 2.3 shows the time evolution of the flow profile when the wall on the left is started to be moved at time $t = 0$. Again, the result of the SRD simulation agrees with the theoretical solutions.

The advantage of the algorithm we used here is that it can be applied to any channel flows in complex geometry since the wall can be set by choosing the wall-cells in the simulation. Fig. 2.4 shows the result of the flow through a porous medium driven by gravity. Here the gravity of 0.04 $[a/\tau^2]$ is applied.

Fig. 2.5 shows the flow in a square cavity where the left edge is moving at the constant velocity $0.8[a/\tau]$.

In the simulations shown in Figs. 2.4 and 2.5, we assumed the periodic boundary condition in all directions.

2.3.2 Motion of a DNA molecule in a solvent

Next, we test the SRD algorithm for a DNA molecule in a solvent. The comparison between SRD simulations and the Zimm theory [13, 14] was done by Kikuchi [7] and also by Ripoll et al. [19]. Here, we repeat the test again since the DNA model used

here is different from those in the previous works.

We placed a DNA molecule in a large simulation box without wall-cell in the periodic boundary conditions in all directions and conducted two kinds of simulation.

First, we simulated the motion of a DNA molecule for a long time under no-flow condition and obtained the radius of gyration R_g and the self diffusion constant D of the center-of-mass of the DNA molecule. Here, R_g is defined as:

$$R_g{}^2 = \frac{1}{2N} \sum_{p,q=1}^{N} \langle (\mathbf{R}_p - \mathbf{R}_q)^2 \rangle. \tag{2.19}$$

Fig. 2.6 shows the radius of gyration R_g plotted against the number of DNA beads N. We can see that the result of SRD agrees well with the theoretical results for a long polymer chain with excluded volume:

$$R_g \propto N^{0.588} \tag{2.20}$$

Fig. 2.7 shows the self diffusion constant D plotted against N. The solid line is the prediction of the Zimm theory in a good solvent [14]:

$$D_{\text{zimm}} = 0.2030 \frac{k_B T}{\sqrt{6}\eta R_g}, \tag{2.21}$$

which is obtained using the values of R_g in Fig. 2.6. The SRD simulation gives results in good agreement with the Zimm theory for good solvent.

The second simulation was done to obtain the longest relaxation time of the DNA molecule. We followed the same procedure used by Perkins et al. in their experiments to obtain the longest relaxation time [24]. We started from a DNA molecule stretched in x direction and observed the relaxation of the stretch s of DNA. The stretch s of

DNA is defined by the maximum difference of the x-coordinate position of beads:

$$s = \max_{p,q} |R_{px} - R_{qx}| \tag{2.22}$$

We imposed an initial stretch ratio: $s = 0.7L$ and the relaxation of the stretch was calculated. Fig. 2.8 shows the relaxation of $\langle s^2 \rangle$ averaged over 50 samples. We obtained the longest relaxation time τ_p by fitting the curve by the following.

$$\frac{\langle s^2 \rangle}{L^2} = A \exp\left(-\frac{t}{\tau_p}\right) + B \ \left(\frac{\langle s^2 \rangle^{1/2}}{L} \leq 0.3\right). \tag{2.23}$$

Fig. 2.9 shows the relaxation time τ_p plotted against N. Here, the result again agrees with the Zimm scaling:

$$\tau_p \propto N^{3 \times 0.588}. \tag{2.24}$$

Short DNA deviates from the theoretical curve, perhaps because it is not in the scaling regime.

2.4 Migration of DNA in a microchannel

As a practical application of this algorithm, we here investigate the migration of a DNA molecule in a Poiseuille flow. Initially, a DNA molecule was placed centrally between two parallel planes in a random configuration. We then traced the position of its center-of-mass to obtain the distribution profile perpendicular to the surfaces. The two parallel planes were placed with distance $W = 22[a]$. We tracked the motion of the DNA molecule for a time of 80 000$[\tau]$ (1 600 000δt) and collected 16 000 individual positions. The distribution profiles were calculated in Poiseuille flow imposed by gravity over the range: $|\mathbf{g}| = 0.0 \sim 0.2[a/\tau^2]$ for which the centerline velocity is $|\mathbf{v}_{\max}| = 0.0 \sim 9.2[a/\tau]$. The Reynolds number($Re$) is approximately $Re = 0 \sim 150$.

Fig. 2.10 shows the positional distribution of DNA of $N = 10$ across the channel.

It is seen that as the flow rate increases, the DNA migrates towards the center of the channel. Here, the flow rate is denoted by the dimensionless quantity called the Weissenberg number:

$$Wi = \dot{\gamma}\tau_p, \tag{2.25}$$

where $\dot{\gamma}$ is the shear rate at the wall which is calculated from the theoretical curve shown in Fig. 2.2, and τ_p is the relaxation time of the DNA molecule.

Fig. 2.11 shows the same plot for DNA of $N = 20$ and Fig. 2.12 shows the variance of the probability distribution around the center of the channel against the Weissenberg number. Note that the two curves can be scaled in this dimensionless plot. This suggests that the migration of DNA molecules is the intrinsic phenomenon in Poiseuille flow under the presence of the walls . We also show the averaged stretch of DNA in Fig. 2.13 that is scaled by the Weissenberg number.

2.5 Conclusion

To simulate the motion of DNA flowing through in an arbitrarily complex geometry, we employ Stochastic Rotation Dynamics(SRD) and introduce a new method to set boundary conditions using *wall-cells* into which SRD particles can enter and from which they can leave, but in which their average velocity is set to the prescribed wall velocity. After demonstrating the validity of this method of setting the boundary conditions, and replicating the predictions of the Zimm theory for long polymers in quiescent fluid, we applied the method to simulate the probability distribution of a DNA molecule in Poiseuille flow between two parallel planes. We found that DNA molecules in dilute solution tend to concentrate near the center of the channel. For future work, using this simulation method, the behavior of DNA molecules in more complex geometries will be investigated. Also, it is possible to apply this method to determine the behavior of macromolecules in semi-dilute solutions.

2.6 Appendix A: time evolution of Couette and Poiseuille flow

Let us consider the flow of fluid in a channel with parallel-sided walls separated by distance h, placed at $y = 0, h$. For rectilinear flow, or in case $\partial u_x/\partial x = 0, u_y = u_z = 0$, the Navier-Stokes equation becomes:

$$\rho\frac{\partial u_x}{\partial t} = \eta\left(\frac{\partial^2 u_x}{\partial y^2} + \frac{\partial^2 u_x}{\partial z^2}\right) - \frac{\partial p}{\partial x}. \tag{2.26}$$

2.6.1 Transient Couette flow

Assuming that the wall at $y = 0$ is set in motion parallel to itself along the x axis with constant velocity U while another wall is kept stationary, the governing equation is the Navier-Stokes equation in the absence of a pressure gradient:

$$\frac{\partial u_x}{\partial t} = \frac{\eta}{\rho}\frac{\partial^2 u_x}{\partial y^2}. \tag{2.27}$$

Using the method of separation of variables in y and t, velocity is given in terms of a Fourier series as:

$$u_x(y,t) = U\left(1 - \frac{y}{h}\right) - \frac{2U}{\pi}\sum_{n=1}^{\infty}\frac{1}{n}\sin\left(\frac{n\pi y}{h}\right)\exp\left(-\frac{n^2\pi^2\eta t}{\rho h^2}\right). \tag{2.28}$$

2.6.2 Transient Poiseuille flow

The governing equation of flow due to a pressure gradient $g_x = -\partial p/\partial x$, equivalent to a constant external force g_x per unit volume, is:

$$\rho\frac{\partial u_x}{\partial t} = \eta\frac{\partial^2 u_x}{\partial y^2} + g_x \tag{2.29}$$

Using the method of separation of variables, the equation above gives,

$$u_x(y,t) = \frac{g_x}{2\eta} y(h-y) - \frac{4g_x h^2}{\eta\pi^3} \sum_{n=1,3,\cdots}^{\infty} \frac{1}{n^3} \sin\left(\frac{n\pi y}{h}\right) \exp\left(-\frac{n^2\pi^2\eta t}{\rho h^2}\right). \qquad (2.30)$$

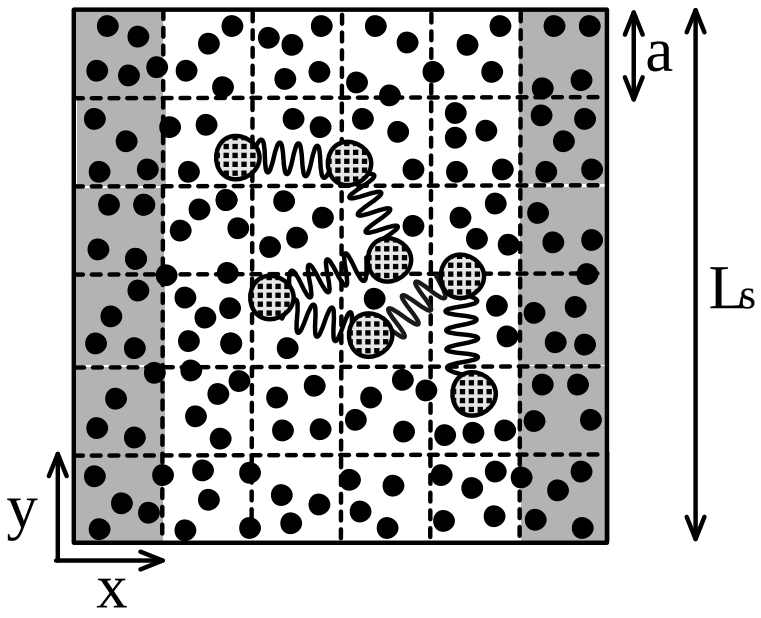

Figure 2.1: Simulation system (drawn two-dimensionally, although we consider a three dimensional system). SRD particles are distributed in a cubic box of dimensions $L_s \times L_s \times L_s$. Collision processes are implemented in each SRD cell bounded by dotted lines which has a volume $a \times a \times a$. A DNA molecule is modeled with a chain with beads(stippled circles) and springs connecting them. Gray cells represent *wall-cells* which define the geometry of the wall.

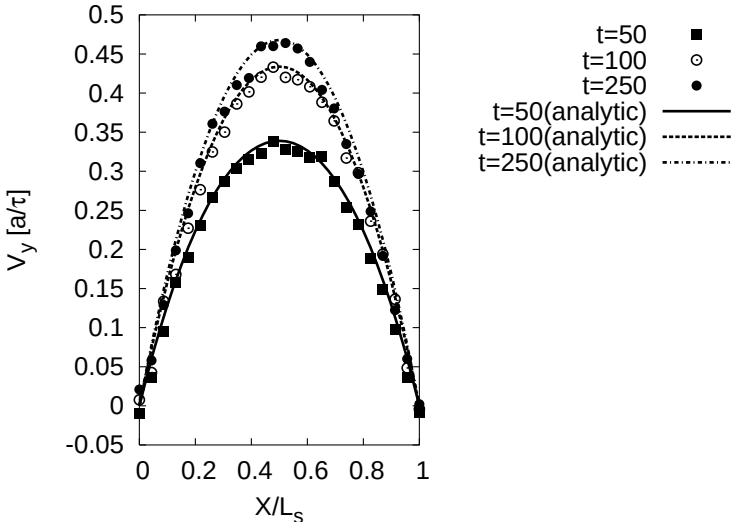

Figure 2.2: The time evolution of Poiseuille flow. The symbols represent the results of the SRD simulation at each time and the lines represent the analytical solution at each time.

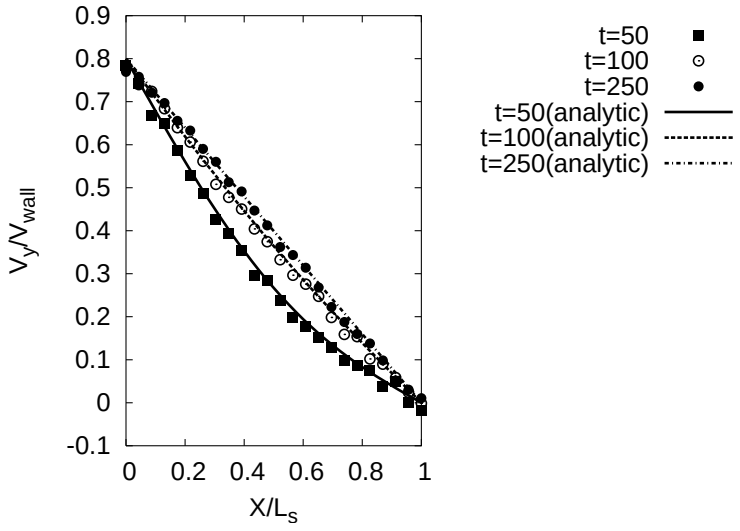

Figure 2.3: The time evolution of plane Couette flow. The symbols represent the results of the SRD simulation at each time and the lines represent the analytical solution at each time.

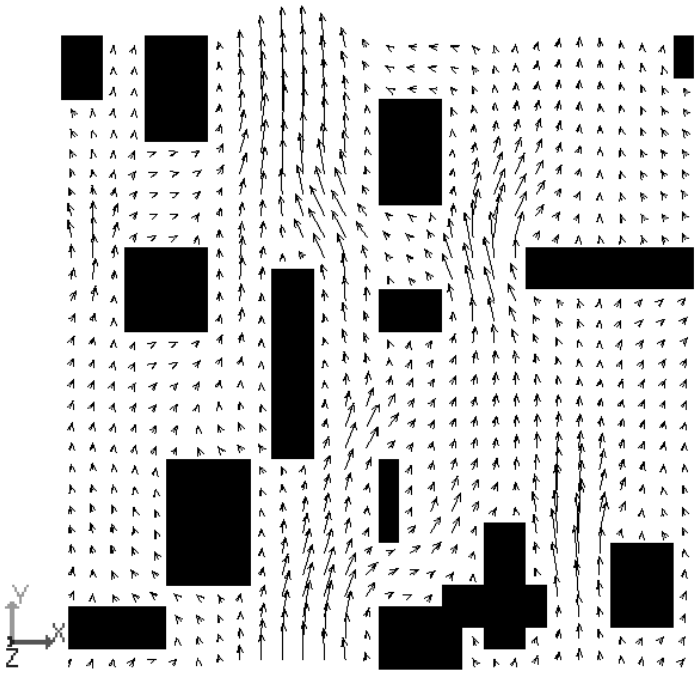

Figure 2.4: Flow in a *porous medium*. The acceleration of gravity 0.04 [a/τ^2] is induced in the y-direction in a system of size $30[a] \times 30[a] \times 30[a]$.

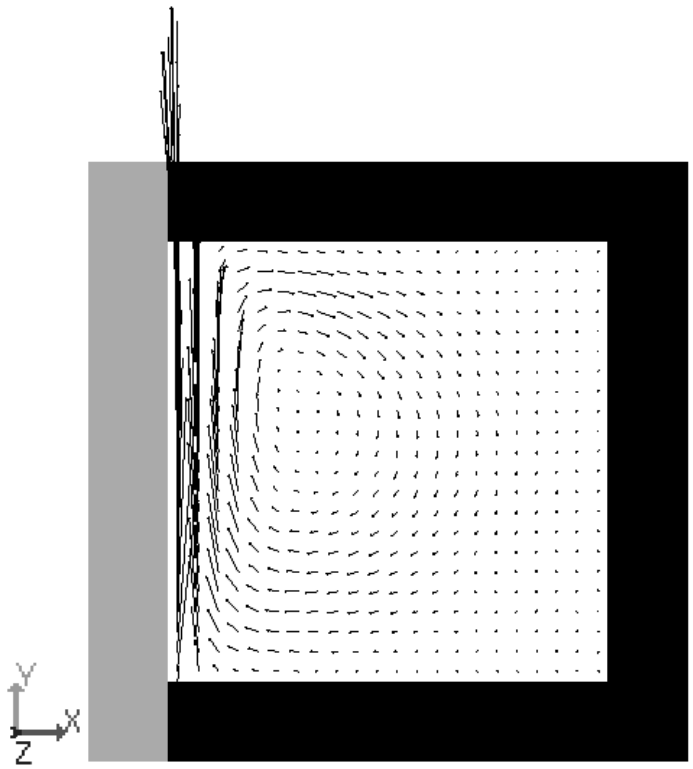

Figure 2.5: Cavity flow. The left wall (the gray part of the boundary) moves in the y-direction at a velocity $0.8[\tau/\mathrm{a}]$ in a system of size $30[a] \times 30[a] \times 30[a]$. The thickness of side walls is $4[a]$. The Reynolds number is about 18.

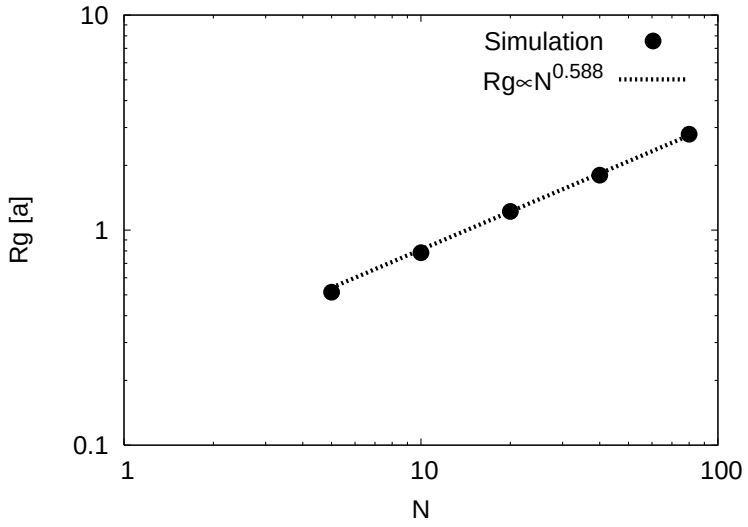

Figure 2.6: The dependence of the radius of gyration(R_g) calculated using the hybrid MD/SRD method on the number of DNA beads N. Since we kept $R_0 = 2.44[a]$ constant, the number of beads is proportional to the contour length of the DNA as: $L = (N-1)R_0$. The symbols denote the results of simulations and the dotted line represents $R_g \propto N^{0.588}$, predicted by the Zimm model for a good solvent.

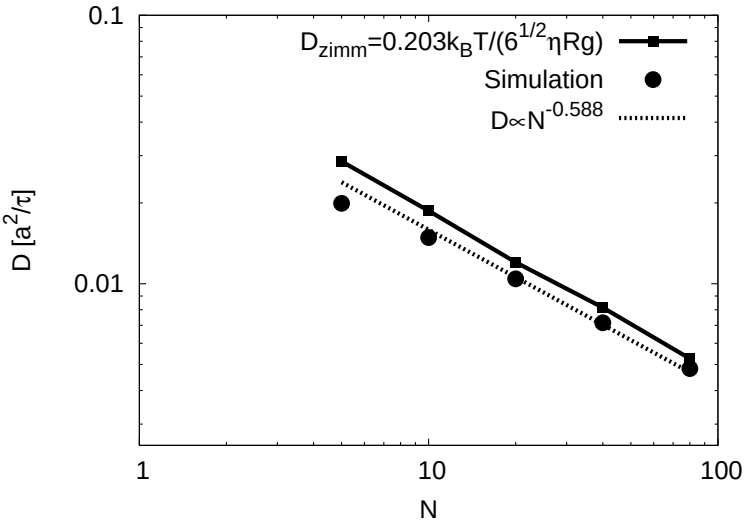

Figure 2.7: The dependence of the diffusion constant(D) of the DNA center-of-mass calculated using the hybrid MD/SRD method on the number of DNA beads N. The solid line is the prediction of the Zimm theory for a good solvent which is obtained using the values of R_g in Fig. 2.6. The dotted line represents the fitted line $D \propto N^{-0.588}$ to the simulation results.

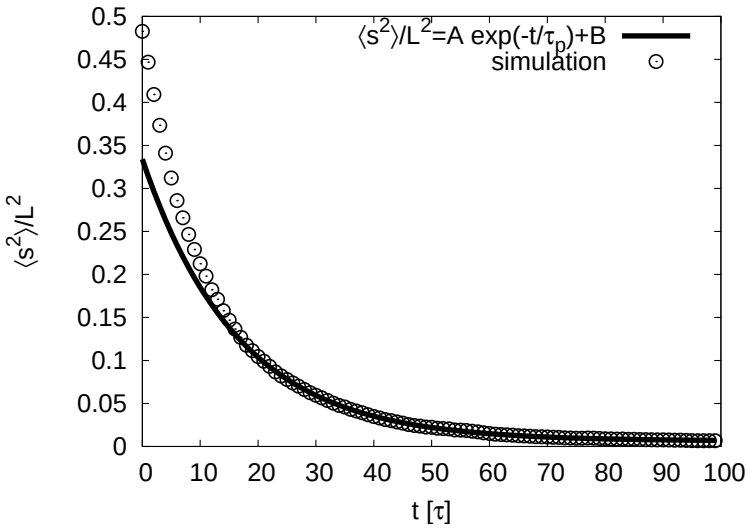

Figure 2.8: Relaxation of mean-square of DNA stretch from an extended state.

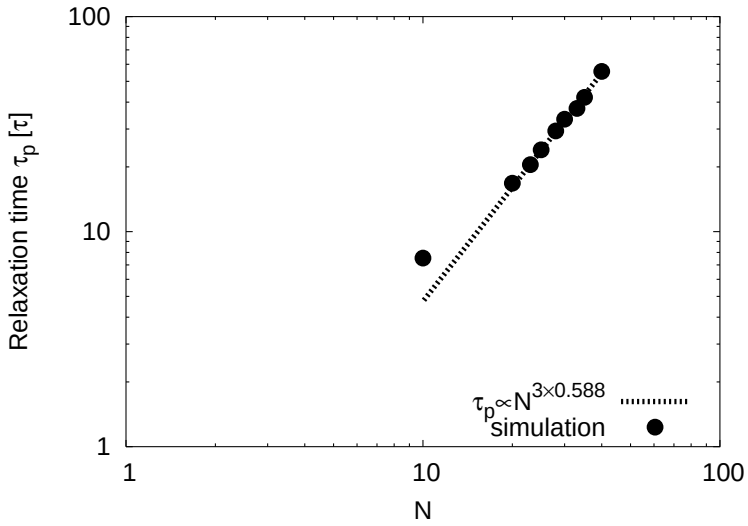

Figure 2.9: The same as Fig. 2.6, for the relaxation time of (τ_p). The dotted line represents $\tau_p \propto N^{-0.588}$, predicted by the Zimm model for a good solvent.

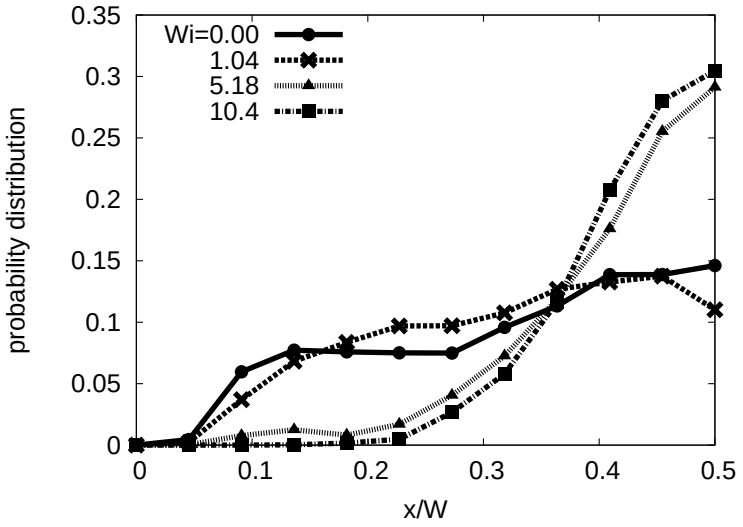

Figure 2.10: Probability distribution of a DNA molecule of contour length 22.0[a] (10 beads) in Poiseuille flow between two parallel planes as a function of distance normal to the planes . Here, x is distance from a plane and W is the distance between two parallel planes. Due to the symmetry, only half of the distribution profile is shown.

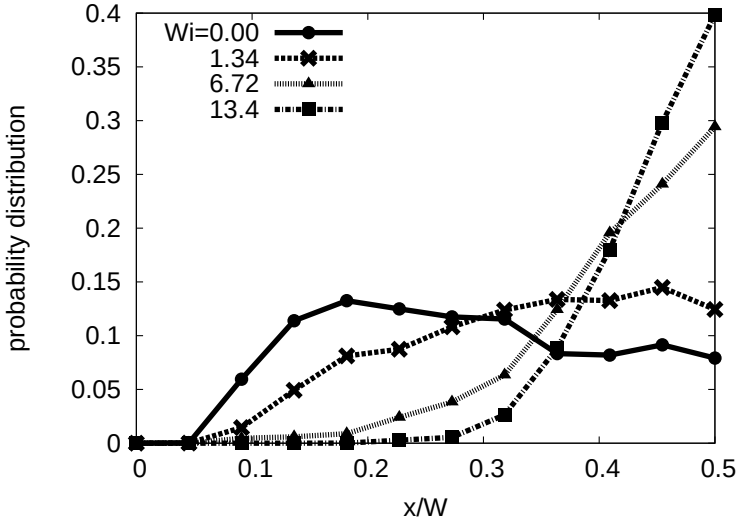

Figure 2.11: The same as Fig. 2.10, except for a molecule with 20 beads(contour length 44.0[a]).

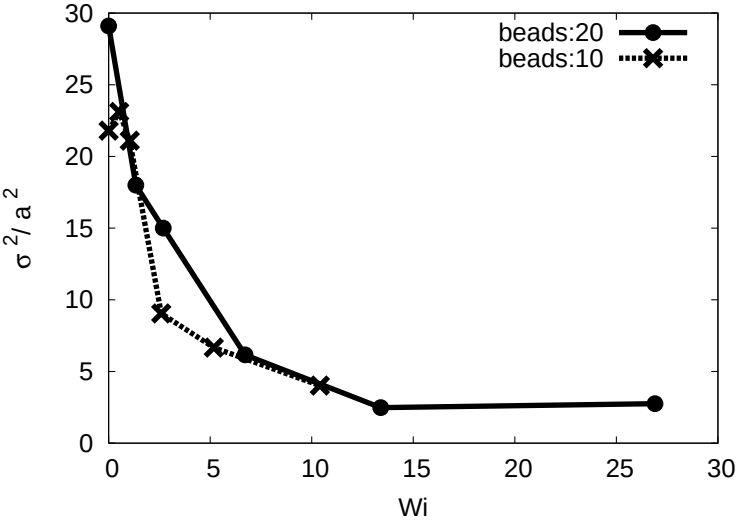

Figure 2.12: Relation between the Weissenberg number(Wi) and σ^2: the variance of the probability distribution of DNA around the center of the channel.

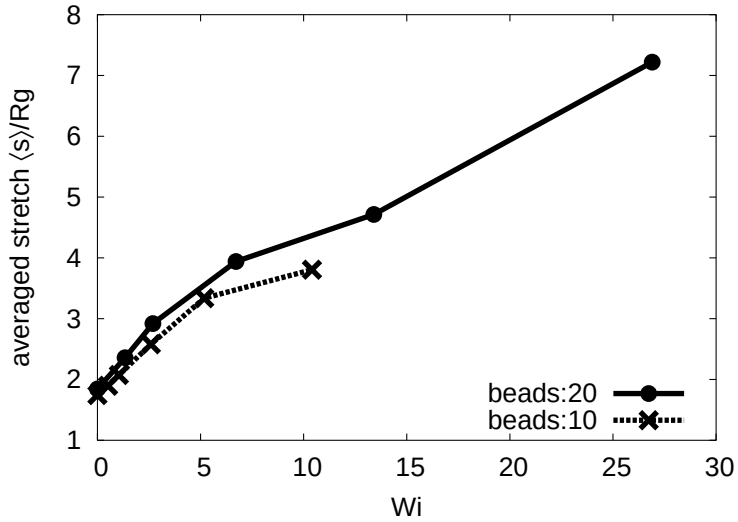

Figure 2.13: Relation between the Weissenberg number(Wi) and average DNA stretch.

CHAPTER III

Fluidic trapping of deformable polymers in micro-flows

3.1 Introduction

The dynamics of a polymer molecule in a micro-flow can be drastically different from that in a uniform flow field. Here, we refer to a micro-flow as a flow field with a significant variation of velocity gradient over length scales of microns, which are typical dimensions of long bio-polymers such as DNA. In such a flow, the conformation of a polymer molecule can be strongly affected by the the structure of the velocity gradient field, which is not uniform over the length scale of the molecule as is the case of macroscopic flows. This is because each segment of the molecule can be subjected to a different velocity gradient due to the rapid variation in velocity.

As an example of interesting phenomenon that can occur in a micro-flow, when a long polymer molecule is placed in an extensional flow, a hysteretic conformational transition (the "coil-stretch transition") can occur as a function of flow strength [25]. This transition was also demonstrated by simulations for a polymer tethered to a stagnation point in an extensional flow [26]. As another example, it was predicted by simulations that a coil-stretch transition can be controlled by a combination of counter-rotating vortexes and an attractive potential from a plane wall [27].

We report here that a polymer molecule can be trapped both spatially and conformationally using only a micro-flow which has at least two stagnation points (or two

points with equal velocity) and a net flow orthogonal to the line connecting them. Such micro-flows are likely to be common in micro-fluidic devices in which the velocity gradient can vary significantly over the length scale of the polymer. One example considered in this article is a Taylor vortex velocity field (Fig. 3.1) [28] . The spatial and conformational trapping in a micro-flow indicates that micro-flow can generate a non-uniform probability distribution of polymer in the position-conformation phase space. When this non-uniformity varies with the size of molecule, this concept can be applied for molecule separations.

Below, the simulation methods and the model for a polymer molecule are presented (Sec. 3.2.2), followed by the results in Taylor vortex flow (Sec. 3.3.1) and an electro-osmotic flow in a micro-channel (Sec. 3.3.3). Also, the effect of hydrodynamic interaction (HI) is discussed for trapping of single molecule and for simultaneous trapping of two molecules in Sec. 3.3.2.

3.2 Method

3.2.1 Taylor vortex flow

Taylor vortex flow (Fig. 3.1) is an incompressible flow field and can be expressed in terms of a scalar stream function $\Psi(x, y)$ as [28]:

$$\Psi(x,y) = \frac{A\alpha\beta}{2\pi}\cos(2\pi x/\alpha)\cos(2\pi y/\beta), \tag{3.1}$$

$$v_x(x,y) = \frac{\partial\Psi}{\partial y} = -A\alpha\cos(2\pi x/\alpha)\sin(2\pi y/\beta), \tag{3.2}$$

$$v_y(x,y) = -\frac{\partial\Psi}{\partial x} = A\beta\sin(2\pi x/\alpha)\cos(2\pi y/\beta), \tag{3.3}$$

$$v_z(x,y) = 0. \tag{3.4}$$

Although without a driving force the Taylor vortex decays with time due to viscosity, this decay is ignored here and β is assumed to be equal to α, for simplicity.

Therefore, the only parameters required to specify the flow field are the magnitude of the flow velocity A and the wavelength α.

3.2.2 Brownian dynamics

Using Taylor vortex velocity field, we compute the three dimensional motion and deformation of a polymer molecule with the Brownian Dynamics (BD) simulation. A bead-spring model is employed to represent the polymer molecule and the following equation of motion is computed for each bead [15]:

$$\boldsymbol{r}_i(t+\delta t) - \boldsymbol{r}_i(t) = \boldsymbol{v}_i(\boldsymbol{r}_i)\ \delta t + \frac{\boldsymbol{f}_i}{\xi}\ \delta t + \sqrt{6\ \frac{\delta t\ k_B T}{\xi}}\ \boldsymbol{n}. \tag{3.5}$$

Here, $\boldsymbol{r}_i$, $\boldsymbol{v}_i$ and $\boldsymbol{f}_i$ are the position, velocity and force vectors of bead $i(=0 \rightarrow N)$, respectively, where $\boldsymbol{v}_i(\boldsymbol{r}_i)$ is given by Eqs. 3.2, 3.3 and 3.4. δt is the time increment of the simulation, ξ is the drag coefficient of each bead, k_B is the Boltzmann constant, T is the absolute temperature, and $\boldsymbol{n}$ is a random vector whose components are chosen from the range $[-1, 1]$ in each time step. This is a free-draining BD simulation with hydrodynamic interactions (HIs) between beads ignored. The effect of HI is discussed in the Sec. 3.3.2.

We take the force of the spring, which connects the adjacent beads i and j, to be that of a WLC (worm-like-chain) [21, 22, 29] used to model semi-flexible polymers such as a DNA:

$$\boldsymbol{f}_{ij}^{\mathrm{sp}} = \frac{k_B T}{2 b_K} \left\{ \left(1 - \frac{r_{ij}}{R_0} \right)^{-2} - 1 + \frac{4 r_{ij}}{R_0} \right\} \frac{\boldsymbol{r}_{ij}}{r_{ij}}, \tag{3.6}$$

where $\boldsymbol{r}_{ij} = \boldsymbol{r}_i - \boldsymbol{r}_j$, b_K is the Kuhn length of the polymer, and $R_0 = L/(N-1)$ is the maximum spring length where L is the contour length of the molecule. The force due to the excluded volume of beads is modeled as [29]:

$$\boldsymbol{f}_{ij}^{\mathrm{ex}} = -\frac{\partial U_{ij}^{\mathrm{ex}}}{\partial \boldsymbol{r}_{ij}} \tag{3.7}$$

with

$$U_{ij}^{\text{ex}} = \frac{1}{2} v k_B T N_{K,s}^2 \left(\frac{3}{4\pi S_s^2} \right)^{3/2} \exp\left(-\frac{3 r_{ij}^2}{4 S_s^2} \right), \tag{3.8}$$

where v is the excluded volume parameter, and $S_s^2 = N_{K,s} b_K^2/6$ is the radius of gyration of an ideal chain consisting of $N_{K,s}$ Kuhn segments, with $N_{K,s}$ related to the spring length R_0 by $R_0 = N_{K,s} b_K$. The total conservative force acting on bead i is $\boldsymbol{f}_i = \sum_j (\boldsymbol{f}_{ij}^{sp} + \boldsymbol{f}_{ij}^{ex})$.

In what follows, we take l, $k_B T$ and τ as the units of length, energy and time, respectively, and they are typically given units of $[\mu m]$, $[k_B T]$ and $[s]$. In our simulations, the time increment of the polymer motion is $\delta t = 0.01[\tau]$. The drag coefficient of a bead is $\xi = 11.9[k_B T\ \tau/l^2]$. The contour length of the polymer molecule is $L = 21.0[l]$ and the polymer contains 10 beads. The Kuhn length is $b_K = 0.106[l]$ and excluded volume parameter $v = 0.0012[l^3]$. These parameters for the WLC spring model and the excluded volume potential were taken from Ref. [29] to model a λ-DNA molecule.

3.3 Results

3.3.1 Trapping in a Taylor vortex flow

The BD simulations for a polymer in a Taylor vortex flow show that the molecule can exist in two types of state, the conformationally trapped and the tumbling state (see Fig. 3.2). In the tumbling state, the polymer molecule rotates in a vortical region of the flow. In the trapped state, the polymer molecule is held roughly stationary both spatially and conformationally long enough to be tracked for many polymer relaxation times even in the presence of Brownian motions.

This phenomenon is analogous to the coexistence of both coiled and stretched states of a polymer tethered to a plane wall and subjected to a stagnation point flow [26]. In this micro-flow, the tethered polymer can exist in either a coiled or

stretched state, since in the stretched state, the free end of the polymer resides in a fast flow that keeps the chain stretched, while in the coiled state, the whole molecule resides near the stagnation point.

The stability of the trapped state is dependent on the parameters of flow field, A and α (See Fig. 3.3). We find that the trapped state is more stable for larger A and that there is an optimal α that maximizes stability, which is around $\alpha = 12.0[l]$ for a molecule of contour length $21.0[l]$ with 10 beads. If A is large and α is tuned for trapping, this can lead to "ergodicity breaking" where the trapped state and the tumbling state become separated from one another for very long times in the conformational phase space of the system [26]. The simplest example of ergodicity breaking was demonstrated by Schroeder *et al.* for a very long DNA molecule in extensional flow [25].

The stability of the trapped state can be explained by a simple local force balance along the molecule between the drag forces from the flow on the beads and the spring forces. As shown in Fig. 3.4, although the drag forces stretch the molecule and tend to pull it upwards, the spring forces acting along the curved contour of the molecule tend to pull the molecule back downwards and limit its stretch. The total spring force pulling the molecule toward the center of the curvature is the same force that induces radial migration of a polymer molecule in a curvilinear shearing flow such as a concentric-cylinder or a cone-and-plate flow [30, 31]. Here, however, this force is exactly balanced by the total drag force by the flow field, leading to both conformational and positional trapping.

Neglecting Brownian motion, the force balance along a polymer molecule in the trapped state can be expressed by the following equation:

$$\boldsymbol{v}\left(\boldsymbol{r}(s)\right)\xi(s) + \frac{d}{ds}\left\{\frac{f^{sp}(\lambda(s))}{\lambda(s)}\frac{d\boldsymbol{r}}{ds}\right\} = 0 \tag{3.9}$$

with boundary conditions:

$$\left.\frac{d\boldsymbol{r}}{ds}\right|_{s=0} = \left.\frac{d\boldsymbol{r}}{ds}\right|_{s=L_p} = 0. \tag{3.10}$$

Here, $\boldsymbol{r}(s)$ is the position vector at s, which is a position coordinate along the polymer contour, $\boldsymbol{v}(\boldsymbol{r}(s))$ is the velocity of solvent at position $\boldsymbol{r}(s)$, $\xi(s)$ is the drag coefficient per unit length of the polymer at s, $\lambda(s)$ is the local stretch of the polymer at s and L_p is the length of the polymer. The first term of the left side in Eq. 3.9 represents the drag force per unit length at position $\boldsymbol{r}(s)$ and the second term represents the derivative of the tension vector at the position, which produces a net migration force normal to the polymer contour. Solving Eq. 3.9 for a molecule modeled by our bead-spring model, we obtain the stable conformations in a Taylor vortex flow shown in Fig. 3.5. All of these conformations were confirmed to be stable enough to hold the molecule in fixed conformation and position even when Brownian motion is added. Note, however, that not all of these conformations were observed in the BD simulations because some of them have only a small chance of being accessed from an arbitrary starting state. When the size of the vortexes is much smaller than that of molecule (i.e. $\alpha \ll L$), the molecule can be trapped over multiple vortexes via stagnation points at the centers of the vortexes.

3.3.2 Effect of hydrodynamic interactions

BD simulations with hydrodynamics interactions were also carried out to examine the effect on the trapping behavior in a Taylor vortex flow. The HIs between beads of a polymer molecule were computed using the RPY tensor [32, 33], and the details of this simulation are described in Appendix. The simulation results show that HI doesn't significantly affect the trapping behavior but only produces a small variation from free-draining simulations in the mean trap times (Fig. 3.3). This is because the

flow perturbation induced by HIs are not large enough, even in the trapped state, to significantly change the conformation of a polymer in the Taylor vortex flow. Fig. 3.6 shows the flow perturbation by HIs in the $z = 0$ plane, where a polymer is trapped, and the velocity induced by HIs is only 15% of the magnitude of the Taylor vortex flow ($A\alpha$) at most, even very close to the polymer.

An interesting point to note here is that, when a polymer is trapped in the x-y plane at $z = 0$, the flow perturbation velocity field in a x-y plane for $z \neq 0$ has a non-zero z-component of velocity. In other words, a two-dimensionally trapped polymer pushes solvent hydrodynamically along the z axis. As shown in Fig. 3.7, the z-component of the flow perturbation is directed away from the trapping plane ($z = 0$) over most of the area, and decays with distance from the trapped polymer. Note that the flow perturbations were computed for a trapped polymer at the steady state without Brownian motion using the parameters $A\alpha = 10.0[l/\tau]$, $\alpha = 2.0[l]$ and $L = 21.0[l]$ (10 beads).

These results imply that two trapped polymers close together in a Taylor vortex flow interact repulsively due to the induced HIs. We computed the velocity of center-of-mass migration by HIs in z-direction for four different configurations of two simultaneously trapped polymers (Fig. 3.8). For all four configurations, two trapped polymers repel each other, and the repulsive velocity decays $\sim r_{12}^{-1.8}$ asymptotically, where r_{12} is the distance between centers-of-mass of two trapped polymers. Therefore, if multiple polymers were simultaneously trapped in a micro-flow, they would disperse in space and not concentrate.

3.3.3 Trapping in an electro-osmotic flow

Conformational trapping of a polymer molecule is a general phenomenon that might occur for a deformable polymer molecule in a flow field that satisfies the conditions that there are at least two stagnation points and a net flow orthogonal to the

line connecting them.

One well-defined geometry that creates such a flow is a electro-osmotic flow generated by an electric field $\boldsymbol{E}$ in a fluid bounded by surfaces bearing a charge varying sinusoidally in space, which was proposed by Ajdari [34]. Consider two flat insulating surfaces, defined as the $x = \pm h$ planes in a (x, y, z) system of Cartesian coordinates, confining an electrolyte solution of Debye length κ^{-1}, dielectric constant ϵ and viscosity η. If the surfaces have a symmetric charge distribution: $\sigma^+(y) = \sigma^-(y) = \sigma_0 \cos(qy)$, the stream function of the flow field $\phi(x, y)$, such that $\partial_x \phi = v_y$ and $\partial_y \phi = -v_x$, is expressed as:

$$\phi(x, y) = \mu_0 E_y \cos(qy) \frac{h \cosh(qh) \sinh(qx) - x \sinh(qh) \cosh(qx)}{hq - \sinh(qh) \cosh(qh)} \tag{3.11}$$

in the limit of a thin Debye layer $\kappa \gg q, h^{-1}$, where $\mu_0 = -\sigma_0/\eta\kappa$ and E_y is the y component of the electric field.

From simulations using this geometry, we find that a neutral polymer molecule can be trapped in a similar way as in a Taylor vortex flow (see Fig. 3.9). Although Panwar *et al.* previously studied the polymer stretching behavior in the same geometry, their ratio of the size of the polymer molecule to channel width $2h$ was too small ($R_g/2h \simeq 10^{-3}$) for the flow to trap a polymer conformationally [35]. In our simulation, $R_g/2h \simeq 0.03$ was used.

Moreover, when the surfaces of this channel have a net charge: $\sigma^+(y) = \sigma^-(y) = \sigma_0 \cos(qy) + \sigma_{\text{net}}$, the simulations show an inhomogeneous distribution of a neutral polymer molecule in the resulting electro-osmotic flow as shown in Fig. 3.10. The polymer molecule is trapped near either of the two streamlines that have a relatively large flow velocity and rarely seeps into the region between them. When trapped along a streamline, the molecule is stretched along the streamline most of time and we observed a conformation similar to the trapped state shown previously in the Taylor

vortex flow, but here, because of a net flow, the conformation changes periodically and the motion resembles that of a swimming sea snake.

Note that the surfaces have a sinusoidal charge plus a net charge, which is equivalent to surfaces having only a sinusoidal charge but a polymer molecule having a charge, whose electrophoretic mobility is $\mu_p = \sigma_{\text{net}}/\eta\kappa$.

3.4 Summary and Discussion

Our simulations suggest the possibility of single-molecule trapping and stretching using only a fluid flow such as a micro-flow with multiple vortexes. Using such a flow, a polymer molecule can be trapped spatially and conformationally without external force or physical constraint. The stability of the trapped state of a molecule can be optimized by tuning the parameters of the flow field, namely the magnitude and the size of the vortexes.

The trapped state is stabilized by two key dynamics of the polymer: coil-stretch transition and the center-of-mass migration in a curved streamline. The conformational trap is triggered by the coil-stretch transition that separates two conformational states of a polymer molecule in the conformation phase space. The positional trap is realized by a balance between the migration induced by the drag force on the molecule and the center-of-mass migration in a curved streamline, which is also observed in a curvilinear shear flow such as a cone-and-plane flow.

Note that micro-flows with multiple vortexes have been used to mix solutions in a micro-channel [36]. Our study suggests that this flow could also demix or concentrate polymer molecules when the length scale of the molecule size is comparable to, or larger than the vortex size. This effect could be utilized for separation of polymer molecules from small molecules, such as separation of DNA from proteins.

3.5 Appendix: Brownian Dynamics with Hydrodynamic Interactions

To describe Brownian dynamics simulations with hydrodynamics interactions between the beads of the polymer, we replace Eq.3.5 by [37]:

$$\boldsymbol{r}_i(t+\delta t)-\boldsymbol{r}_i(t)=\left\{\boldsymbol{v}_i(\boldsymbol{r}_i)+\sum_{j=1}^{N}\frac{\partial\mathcal{D}_{ij}}{\partial\boldsymbol{r}_j}+\sum_{j=1}^{N}\frac{\mathcal{D}_{ij}\cdot\boldsymbol{f}_j}{k_BT}\right\}\delta t+\sqrt{6\ \delta t}\ \sum_{j=1}^{i}\mathcal{B}_{ij}\cdot\boldsymbol{n}_j. \quad (3.12)$$

where $\mathcal{D}\left(=\mathcal{B}\cdot\mathcal{B}^T\right)$ is the RPY tensor described as [29, 32, 33]:

$$\mathcal{D}_{ii} = \frac{k_BT}{\xi}\mathcal{I}, \quad (3.13)$$

$$\mathcal{D}_{ij} = \frac{k_BT}{\xi}\ \frac{3a}{4r_{ij}}\left[C_1\mathcal{I}+C_2\frac{\boldsymbol{r}_{ij}\boldsymbol{r}_{ij}}{r_{ij}^2}\right]\ \text{if } i\neq j \text{ and } r_{ij}\geq 2a, \quad (3.14)$$

$$\mathcal{D}_{ij} = \frac{k_BT}{\xi}\left[\left(1-\frac{9r_{ij}}{32a}\right)\mathcal{I}+\frac{3}{32}\frac{\boldsymbol{r}_{ij}\boldsymbol{r}_{ij}}{ar_{ij}}\right]\ \text{if } i\neq j \text{ and } r_{ij}<2a, \quad (3.15)$$

$$C_1 = 1+\frac{2a^2}{3r_{ij}^2}, \quad (3.16)$$

$$C_2 = 1-\frac{2a^2}{r_{ij}^2}. \quad (3.17)$$

Here, $\boldsymbol{r}_{ij}=\boldsymbol{r}_i-\boldsymbol{r}_j$, $\mathcal{I}$ is the 3×3 identity matrix, a is the radius of a bead and ξ is the drag coefficient of a bead. The parameters $a=0.077[l]$ and $\xi=15.4[k_BT\ \tau/l^2]$ were used to make the relaxation time and the diffusivity of the polymer equivalent to those of the free-draining BD simulation [29]. Note that the gradient of $\mathcal{D}_{ij}$ (the second term in the right-hand side of Eq. 3.12) vanishes for the RPY tensor.

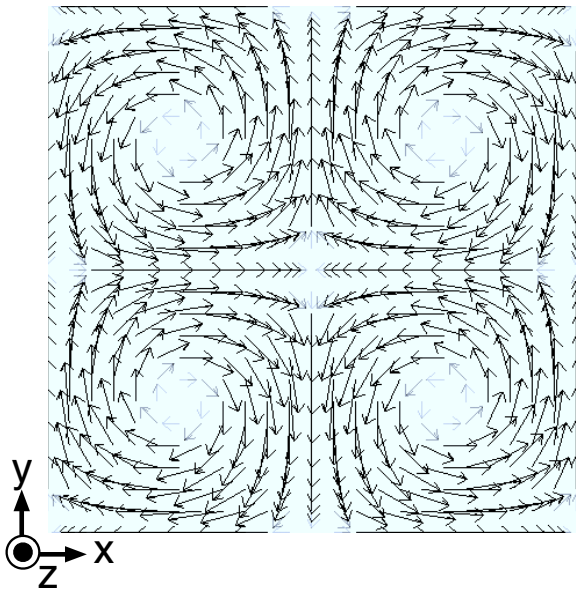

Figure 3.1: Taylor vortex flow field. Drawn for the region $(x, y) = ([0, \alpha], [0, \alpha])$. The velocity component of z direction is always zero.

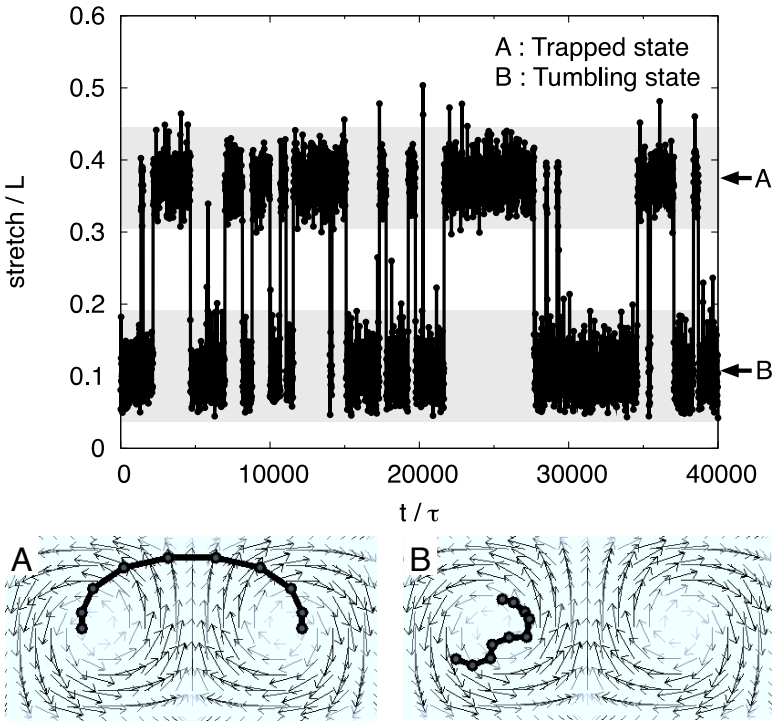

Figure 3.2: A stretch history of a polymer molecule in a Taylor vortex flow with $A\alpha = 2.0[l/\tau]$, $\alpha = 12[l]$ (top). The polymer takes two states: the trapped state (left bottom) and the tumbling state (right bottom). The polymer molecule has contour length $L = 21[l]$ (10 beads) and the stretch is defined as the largest distance between any two beads in a molecule.

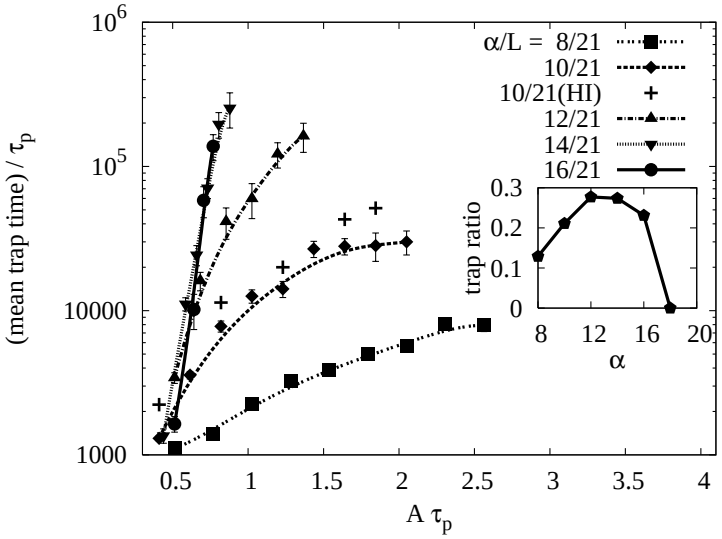

Figure 3.3: Relationship between mean trap time of a polymer molecule and the normalized magnitude of flow field A. Here, τ_p is the relaxation time of the polymer, and α/L represents the ratio of the wavelength of the Taylor vortex flow (i.e. 2×vortex size) to the contour length of the polymer molecule. Data denoted by (+) symbols were obtained by BD simulations with hydrodynamic interactions, and others by free-draining BD simulations. Error bars indicate the standard errors. In the inserted figure, the trap ratio, which is the fraction of time a molecule is trapped, is shown for $A\tau_p/\alpha = 0.7$.

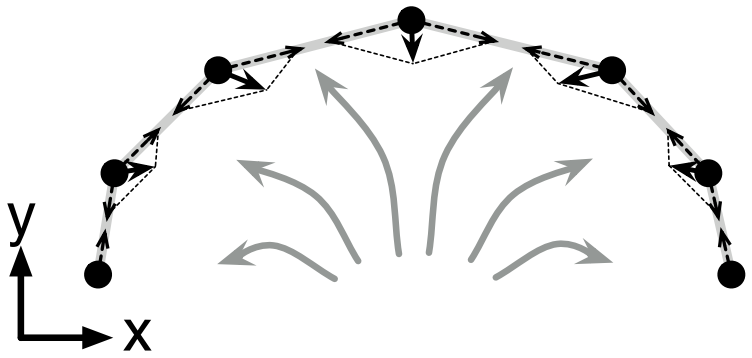

Figure 3.4: Local force balance along a curved polymer molecule under fluidic stretching: the spring forces (black arrows) balance the drag forces exerted on beads by a solvent flow(grey arrows)

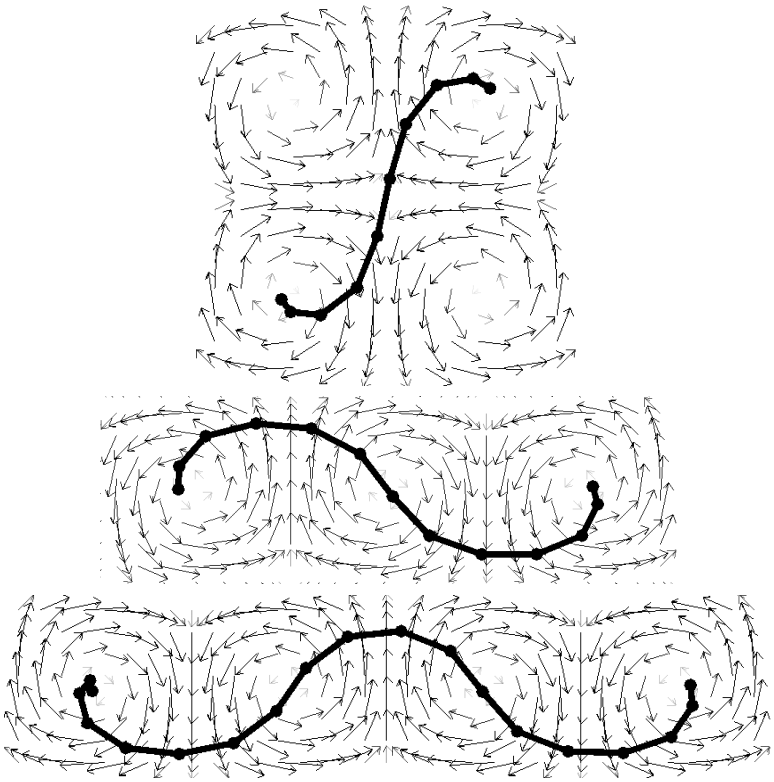

Figure 3.5: Examples of stable conformations of polymer molecules in Taylor vortex flow for $A\alpha = 8.0[l/\tau]$ and $\alpha = 12[l]$. The number of beads is 10 in the top figure, 13 in the middle and 19 in the bottom.

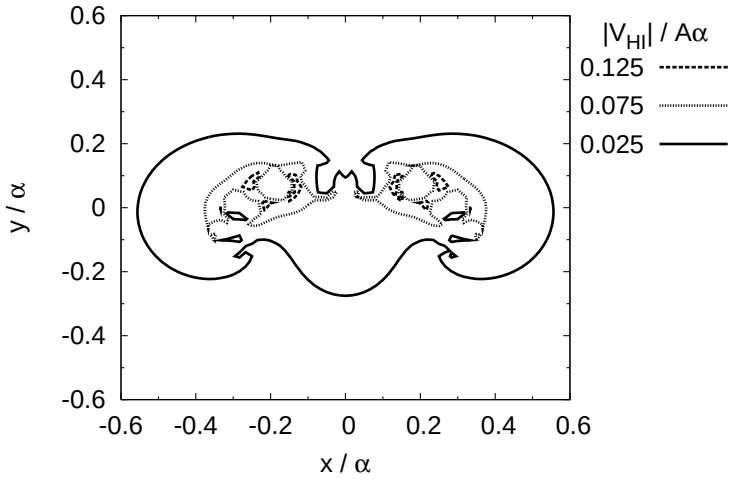

Figure 3.6: The magnitude of flow perturbation velocity field ($\boldsymbol{V}_{\mathrm{HI}}(x, y)$) induced by hydrodynamic interactions in the x-y plane at $z = 0$, where a polymer molecule is trapped. The directions of the x and y axes are the same as in Fig. 3.4 with respect to the conformation of the trapped polymer, and the origin $(x, y) = (0, 0)$ is set to be the center-of-mass of the trapped polymer. Note that, in this plane, the flow perturbation velocity doesn't have z-component and has only in-plane components.

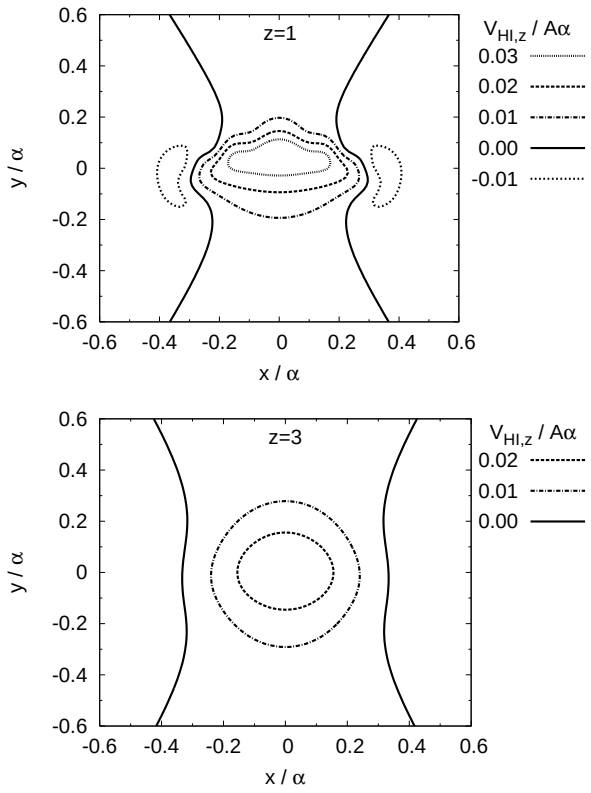

Figure 3.7: The z-component of the flow perturbation velocity field ($V_{\mathrm{HI},z}(x, y)$) in the $z = 1$ plane (top) and $z = 3$ (bottom) induced by hydrodynamic interactions from a polymer trapped in the $z = 0$ plane. The directions of the x, y axes and the origin are chosen as in Fig. 3.6. A positive $V_{\mathrm{HI},z}$ indicates a velocity away from the z=0 plane, where the trapped polymer resides.

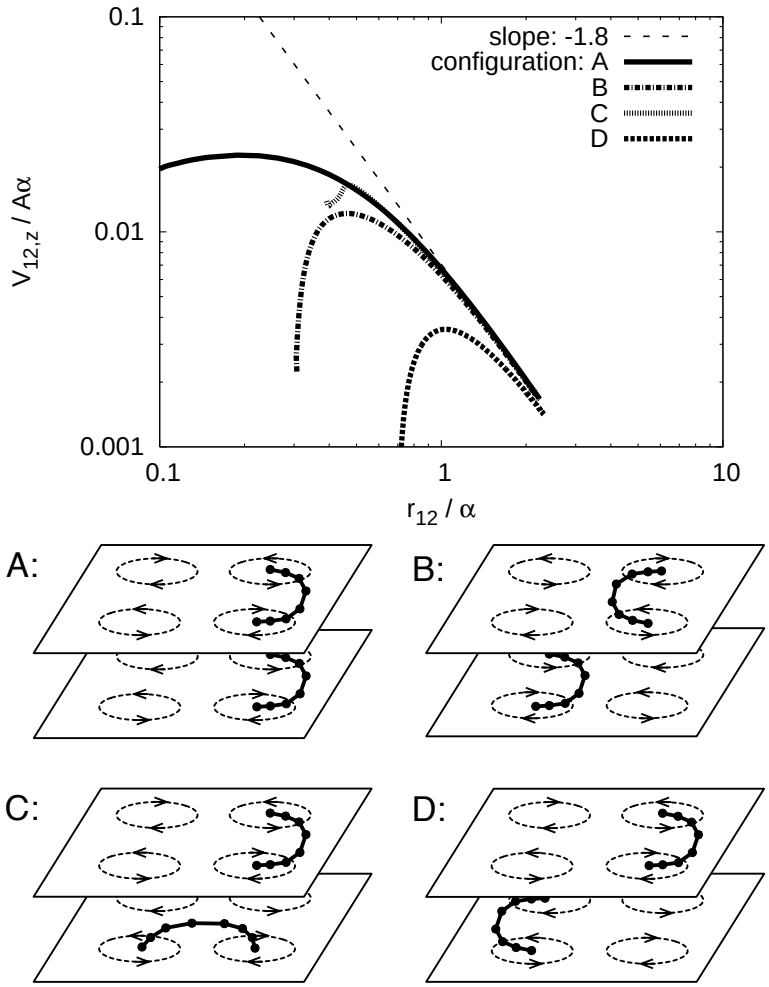

Figure 3.8: Four configurations of two closely trapped polymers (bottom), and the z-component of the relative velocities of the two centers-of-mass $V_{12,z}$ induced by hydrodynamic interactions for each configurations (top). r_{12} is the distance between the centers-of-mass. Note that a positive $V_{12,z}$ corresponds to chains moving away from each other.

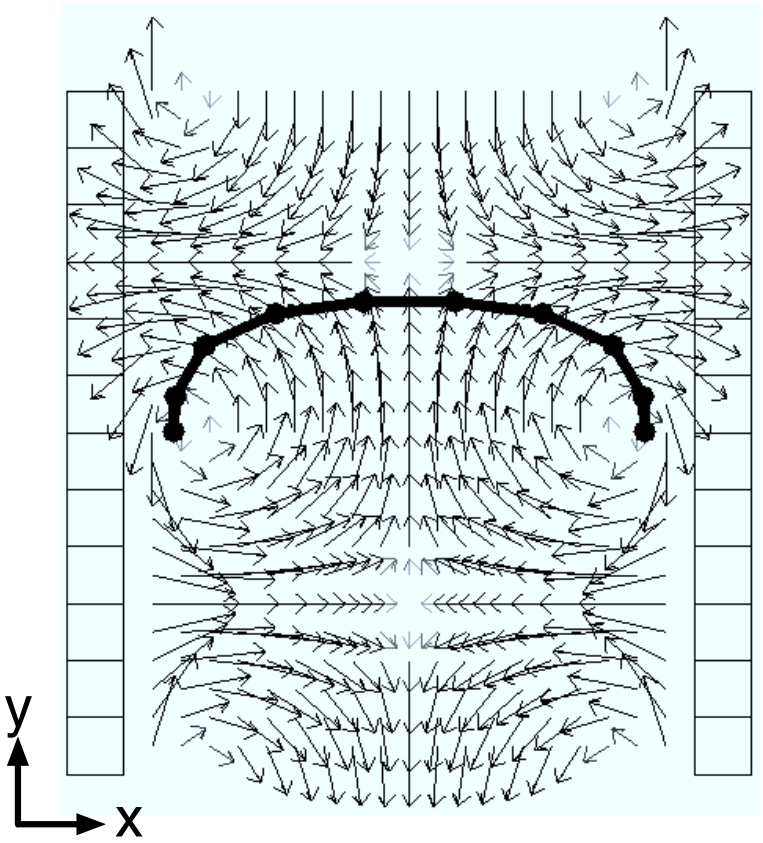

Figure 3.9: Steady-state conformation of a trapped polymer in an electro-osmotic flow in a channel whose surfaces bear a sinusoidally varying charge: $\sigma^{\pm}(y) = \sigma_0 \cos(qy + \pi/4)$, where σ_0 was chosen to satisfy $\mu_0 E_y = 7.0[l/\tau]$, and $q = 2\pi/(2h)\,[l^{-1}]$, $h = 6.0[l]$. The contour length of the polymer is $L = 21[l]$ (10 beads).

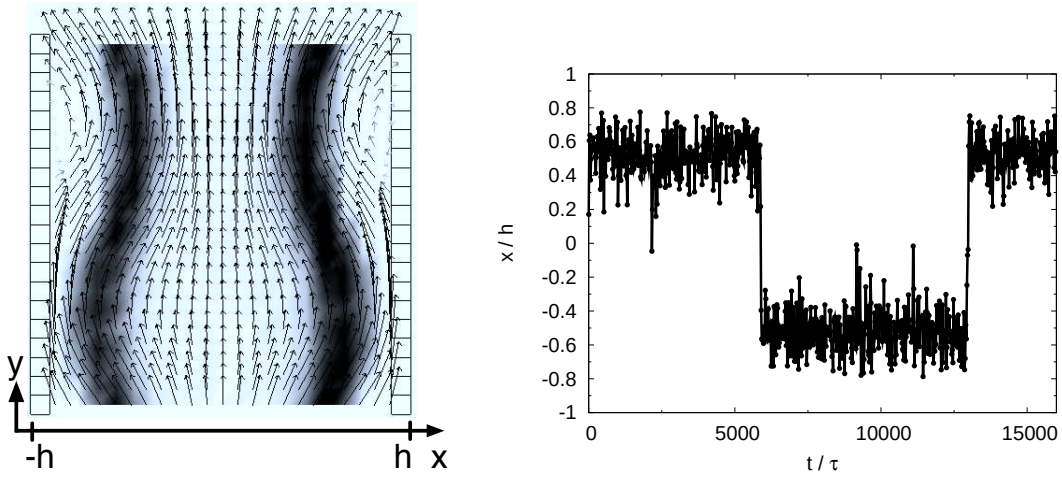

Figure 3.10: The center-of-mass distribution marked as dark shading (left) and history of the center-of-mass position in x-direction (right) of a polymer molecule in an electro-osmotic flow in a channel whose surfaces bear a charge varying sinusoidally plus a net charge: $\sigma^{\pm}(y) = \sigma_0 \cos(qy + \pi/4) + \sigma_{\text{net}}$, where σ_0 and σ_{net} were chosen to satisfy $\mu_0 E_y = 4.0[l/\tau]$ and $\mu_{\text{net}} E_y = 2.0[l/\tau]$, and $q = 2\pi/(2h)\,[l^{-1}]$, $h = 10[l]$. The contour length of the polymer is $L = 63[l]$ (30 beads).

CHAPTER IV

Conformation Dependence of DNA Electrophoretic Mobility in a Converging Channel

4.1 Introduction

Electrophoresis is the migration of charged species in a medium under an applied electric field. This phenomenon has been widely utilized in electrokinetics-related research and applications such as gel electrophoresis separation [38], study of polyelectrolyte dynamics in electrokinetic flows [39, 40], and in electroporation for gene delivery [41]. DNA is a primary material used in many of these applications because of its important role in both biological science and single macromolecule dynamics. In gel electrophoresis, DNA separation is achieved due to the dependence of mobility on molecular size of DNA molecules in the gel. In recent years, many microfluidic devices have been designed to separate DNA molecules by taking advantage of the similarity between the size scales typical in microfluidic geometries and the size of the DNA molecule itself. Examples of such devices include micro-obstacle arrays [42], entropy traps [43], and molecular ratchets [44].

Electrophoretic (EP) mobility (μ_{EP}), defined as the migration velocity obtained under a unit electric field strength ($\mu_{EP} = U_{EP}/E$), is usually set by the size, shape, and charge density of charged species and the ionic strength and viscosity of the medium. In general, electrohydrodynamic interactions are strongly screened in the

electrophoresis of dilute polyelectrolytes because of the movement of surrounding counterions [45]. However, as shown by Long and Ajdari, screening of electrohydrodynamic interactions is not complete, and despite the presence of mobile counterions there should remain a rather steep power-law decay of electrohydrodynamic microflows near the DNA [46]. Transverse migration has also been found in simulations [47] and experimental observations [48, 49] of DNA electromigration in thin channels, which again shows the importance of electrohydrodynamic interactions.

There are several ways to measure the EP mobility of DNA, including the use of capillary zone electrophoresis (CZE) [50], electrophoretic light scattering (ELS) [51], and optical velocimetry. These approaches all rely on the relation $\mu_{EP} = \Delta d/E\Delta t$, where E is the local electric field strength, and Δd the displacement of charged species within a time interval of Δt. In CZE, Δd is the distance between the injection and detection locations (> 10cm) and the traveling time (Δt) is determined by the UV signal carried by the DNA molecules. ELS determines Δd and Δt by measuring the Doppler shift of light scattered from moving DNA molecules. Both CZE and ELS provide an average value of EP mobility from multiple DNA molecules. The recently developed microscale particle tracking velocimetry (μPTV) [52] can obtain the instantaneous velocity of a single charged particle. Observation of the dynamics of individual, fluorescently-stained DNA molecules enables the identification of conformations taken on by DNA molecules during the coil-stretch transition. By combining μPTV with single-molecule DNA measurements, we will here obtain both the velocity and conformation of individual DNA molecules in a well-defined electric field.

In free-solution electrophoresis (i.e. with no gel or other barrier to DNA motion), DNA molecules mostly remain in their coiled conformation and the EP mobility usually remains constant during migration. However, in cross-slot and converging geometries, due to the gradient in field strength, the DNA molecule can undergo a

coil-stretch transition [53]. Here, we investigate the impact of DNA conformational change on EP mobility. To do so, we use a microscale converging channel to create an electric field gradient that stretches DNA molecules and investigate whether or not this stretch induces a change in the EP mobility. Because of "molecular individualism" [54], we can observe multiple DNA conformations in a single experiment and the time dependence of the conformation as it traverses the geometry. We will calculate the instantaneous DNA EP mobility of each molecule and correlate this with its instantaneous conformation. A theoretical analysis will also be employed to estimate the center-of-mass electrophoretic migration of DNA, including the effects of electrohydrodynamic interactions alluded to above.

Note that this chapter is based on the collaboration study with James Lee group in Ohio State University, and all the experimental works had been conducted by the group.

4.2 Materials and Methods

4.2.1 Experimental observation and measurement

4.2.1.1 Fabrication of the converging channel

To study the dependence of EP mobility on the DNA conformation in free solution, a microscale converging channel was designed and fabricated on a poly(methyl methacrylate) (PMMA) plate. The dimensions of the channel are shown in Fig. 4.1, where L, W, l, w_1, and w_2 are 1.5 cm, 300 μm, 300 μm, 20 μm, and 130 μm, respectively. Upon application of a DC voltage across the channel, the magnitude of the electric field $\boldsymbol{E}$ increases in the converging section because of the tapered contraction in the cross-section area. The increased electric field can stretch and consequently change DNA conformation when DNA migrates through the converging channel. The PMMA microfluidic chip was fabricated first by patterning the

microfluidic structure on the silicon wafer using photolithography. A negative photoresist, SU-8 50 (Microchem, Inc) was used to fabricate the female mold of the channel. A poly(dimethylsiloxane) PDMS male mold was then made by casting the mixture of 10:1 ratio (by weight) of PDMS precursor and curing agent (Sylgard 184, Dow Corning) on the patterned SU-8 structure using soft lithography. The mixture was degassed in vacuum for an hour and then cured overnight at 65°C in an oven. The patterned PDMS mold was thus the negative replica of the microscale converging channel. The PMMA converging channel was then fabricated by using the PDMS as the soft mold in the hot embossing process. In the hot embossing, the PDMS mold and the PMMA plate were sandwiched between two glass plates in a heating press (Carver, Inc, IN) at 180°C. The inlet and outlet of the channel were created by drilling holes with diameter of 1.6 mm. Finally, a 50 μm thick PMMA film was thermally laminated onto the surface of the microfluidic plate to form the closed channel.

4.2.1.2 Electrophoresis setup

λ-DNA (48.5 kbps, New England Biolab) is used to study DNA EP mobility. A dilute solution ($\sim$0.03 μg/ml) of λ-DNA in a 10 mM tris-HCl, 2mM EDTA, and 10 mM NaCl buffer at pH 8.0 was labeled with fluorescent YOYO-1 dye at a dye-to-base-pair molar ratio of 1:5. Under these conditions, λ-DNA attains a contour length of about 21 μm when fully stretched [55]. To increase the viscous drag, the bulk viscosity of DNA solution was adjusted by adding glucose and sucrose. In this work, 18% (w/w) glucose and 40% (w/w) sucrose were added so that the final bulk viscosity of DNA solution is 30 cp. To study the electrophoretic migration of DNA molecules in the converging channel, the whole chip was first mounted onto the stage of an inverted epi-fluorescence microscope (TE 2000S, Nikon, Japan). Then, the DNA solution was pumped to fill to channel from the inlet. Electrodes were placed in the wells of inlet and outlet with applied voltage of 100 V applied along the 1.5 cm

long microchannel. An electric field $\boldsymbol{E}$ was generated along the converging channel, which gives a high enough field gradient to induce conformational changes in the DNA molecules. The dynamics of DNA were observed with a $100x/1.3$ NA oil immersion objective lens and recorded by a Coolsnap HQ CCD camera (Roper Scientific, Inc, Tempe, AZ). Single DNA dynamics were studied recently by Brownian dynamics simulations and compared with experimental results [53]. For simplicity, a constant DNA EP mobility was used in the previous simulations. Our goal here, however, is to track each DNA molecule and determine the relationship between EP mobility and DNA conformation.

4.2.1.3 Measurement of electrophoretic mobility

The EP mobility is determined by applying the finite difference scheme to the trajectory of the DNA center-of-mass. From the measured distance traveled by the DNA between two video frames, the time interval between the frames, and the electric field strength computed by the finite element method [53] as shown in Fig. 4.1, a transient mobility can easily be calculated. The EP mobility obtained in this way is an "instantaneous EP mobility" that changes as the DNA molecule migrates. Within the time interval between frames of 0.052 sec, DNA molecules travel a distance of $5\pm2\mu$m. Over this distance, the electric field gradient varies by only a few percent and can be taken to be constant. Also, the electric field varies at most by around 18% over the length of the DNA molecule, and so the field at the molecules center is used to compute the instantaneous mobility. As mentioned in our early work, the deformation of DNA molecules under an extensional electric field is similar to that under a hydrodynamic extensional flow. The angle that the stretched DNA molecule makes with respect to the axis of the device (the x direction) is zero along the center line of the channel and is small in the contraction zone away from the center line [53]. Thus, only DNA located near the central line is chosen for investigation so that DNA

is stretched mainly along the x-direction with minimal wall effects. It can be seen in Fig. 4.1 that the electric field strength develops steep gradient near the end of channel. DNA chain tumbling was observed in this region. Therefore, the tracking of DNA was stopped when the DNA arrived close to the small end ($x = 280\ \mu$m) of the contraction, before the region of steep gradients. The contribution of center-of-mass diffusion to the noise in the distance traveled over the time interval between viewing frames can be estimated from the DNA diffusion coefficients measured by Smith et al. [56]. The root mean square displacement of λ-DNA is thereby determined to be about 0.04 μm over the 0.052 time interval, which is 100 times smaller then the average distance traveled by the DNA molecule over that time interval. Therefore, the contribution of Brownian diffusion to the noise in the measurement of EP mobility is negligible. In total, 32 DNA molecules were traced. The number of captured frames per DNA molecule varied from 9 to 27 depending on the migration speed in the contraction zone. A total of 340 EP mobility data points were obtained in this study.

4.2.2 Theoretical modeling

4.2.2.1 A shish-kebab model

The EP mobility of a charged spherical particle μ_0 is determined by its radius a, carried charge Q, the Debye length κ^{-1} and the viscosity of the solvent eta (i.e. $\mu_0 = \mu_0(a, Q\kappa, \eta)$) [57], and the "far-field" flow perturbation induced by the electrophoresis of a charged spherical particle decays with distance from the particle r as $\sim 1/r^3$ [46], i.e. the velocity perturbation at position r_i results from the EP motion of a charged particle at r_j is

$$\boldsymbol{v}^{\mathrm{EPHI}}(\boldsymbol{r}_i, \boldsymbol{r}_j) = \mathcal{S}(\boldsymbol{r}_{ij}) \cdot \boldsymbol{E}(\boldsymbol{r}_j), \tag{4.1}$$

$$\mathcal{S}(\boldsymbol{r}_{ij}) = \frac{Q}{4\pi\eta\kappa^2 r_i^3} \left(3\frac{\boldsymbol{r}_{ij}\boldsymbol{r}_{ij}}{r_{ij}^2} - \mathcal{I} \right), \tag{4.2}$$

where $\mathcal{I}$ is the unit tensor, and $\boldsymbol{r}_{ij} = \boldsymbol{r}_i - \boldsymbol{r}_j$. We propose a simple "shish-kebab" model for the EP mobility of a short, rigid, segment of a longer, semi-flexible, charged, polymer chain. We generate a shish-kebab by connecting charged spherical particles with thin rods on a straight line as shown in Fig. 4.2. Assuming that each particle has charge Q and radius a, and that the distance between two adjacent particles is b, the center-of-mass velocity of a shish-kebab, which consists of N_{SK} spheres in the electric field $\boldsymbol{E} = (E, 0, 0)^T$ can be expressed as the following for $N_{\mathrm{SK}} \gg 1$:

$$\begin{aligned}
\boldsymbol{v}^{\mathrm{SK}} &= \mu_0 \boldsymbol{E} + \frac{1}{N_{\mathrm{SK}}} \sum_{i=1}^{N_{\mathrm{SK}}} \sum_{j \neq i} \boldsymbol{v}^{\mathrm{EPHI}}(\boldsymbol{r}_i, \boldsymbol{r}_j) && (4.3)\\
&= \mu_0 \boldsymbol{E} + \frac{1}{N_{\mathrm{SK}}} \sum_{i=1}^{N_{\mathrm{SK}}} \sum_{j \neq i} \frac{QE}{2\pi\eta\kappa^2 (b|i-j|)^3} \begin{pmatrix} 3\cos^2\theta - 1 \\ 3\cos\theta\sin\theta\cos\phi \\ 3\cos\theta\sin\theta\sin\phi \end{pmatrix} && (4.4)\\
&= \mu_0 \boldsymbol{E} + \frac{1}{N_{\mathrm{SK}}} \frac{QE}{\pi\eta\kappa^2 b^3} \sum_{i=1}^{N_{\mathrm{SK}}} \left(\frac{1}{1^3} + \frac{1}{2^3} + \cdots + \frac{1}{n^3} \right) \begin{pmatrix} 3\cos^2\theta - 1 \\ 3\cos\theta\sin\theta\cos\phi \\ 3\cos\theta\sin\theta\sin\phi \end{pmatrix} && (4.5)\\
&\cong \mu_0 \boldsymbol{E} + \frac{1.2QE}{\pi\eta\kappa^2 b^3} \begin{pmatrix} 3\cos^2\theta - 1 \\ 3\cos\theta\sin\theta\cos\phi \\ 3\cos\theta\sin\theta\sin\phi \end{pmatrix} && (4.6)\\
&= \mu_0 \boldsymbol{E} + \mu_1 E \begin{pmatrix} 3\cos^2\theta - 1 \\ 3\cos\theta\sin\theta\cos\phi \\ 3\cos\theta\sin\theta\sin\phi \end{pmatrix}, && (4.7)
\end{aligned}$$

where θ and ϕ are angles describing the orientation of the shish-kebab as defined in Fig. 4.2, μ_1 is defined as $\mu_1 \equiv 1.2QE/\pi\eta\kappa^2 b^3$, and the approximation from the third line to the fourth is correct within 4% error for $N_{\mathrm{SK}} > 10$. From the second term of Eq. 4.7, the electrophoretic velocity of the center-of-mass in the direction

of the electric field is highest : $(\mu_0 + 2\mu_1)E$ at $\theta = n\pi$, and smallest : $(\mu_0 - \mu_1)E$ at $\theta = \pi(2n+1)/2$, where n is an integer. Moreover, a migration perpendicular to the electric field is induced when $\theta \neq n\pi/2$. These results qualitatively agree with theoretical and experimental studies on the electrophoresis of spheroidal particles [58] and charged polymers under deformation in the Poiseuille flow [47]. Also, according to Ref. [58], the ratio of the electrophoretic mobilities of an infinite cylinder oriented parallel to the field, perpendicular to the field, and a sphere of the same charge density is $1 : 1/2 : 2/3$ in the regime $\kappa a \lesssim 1$ where a is the radius of a cylinder or a sphere, while this ratio converges to $1 : 1 : 1$ when κa is large ($\sim 10^2$). By comparing this ratio in the regime $\kappa a \lesssim 1$ with our result in Eq. 4.7 for a shish-kebab, i.e. $1 : 1/2 : 2/3 = (\mu_0 + 2\mu_1) : (\mu_0 - \mu_1) : \mu_0$, we find the relation: $\mu_1 = \mu_0/4$ ($\kappa a \lesssim 1$). In the regime $\kappa a \lesssim 1$, μ_1 decreases from $\mu_0/4$ as κa increases. Our experimental condition satisfies $\kappa a \lesssim 1$ with a being the local radius of DNA chain, which allows us to take $\mu_1 = \mu_0/4$.

4.2.2.2 Model for a flexible molecule

To estimate the electrophoretic velocity of a charged polymer, we connect together shish-kebabs, each of length equal to Kuhn step length of the polymer chain, to assemble a flexible sub-chain, just as rods are connected to form a freely jointed chain, as shown in Fig. 4.2. The freely jointed sub-chain is considered to be a single "spring" representing a portion of the whole chain. Each sub-chain, or spring, contains enough shish-kebabs to form a micro-canonical "ensemble" of shish-kebabs over which averages can be taken, but is a small enough portion of the whole chain that each shish-kebab within that spring has behavior that is, on average, identical to that of any other shish-kebab in the same spring. That is, variations in electric field gradient and stretching force are negligible over the small size of the sub-chain represented by a single spring. This is the standard approximation used in bead-spring

modeling of polymer chains. Therefore, we model a chain with four hierarchical levels, which from the smallest to the largest are: 1) spheres, 2) shish-kebab, 3) sub-chain, and 4) chain. In the above Section, Eq. 4.7 describes level 2 (shish-kebab) of the hierarchy, deriving the mobility at this level from the electrokinetics of level 1, given by Eq. 4.1. We now extend our model to level 3 that a sub-chain composed of many connected shish-kebabs. When disconnected from each other, the shish-kebabs have differing velocities that depend on the orientation angles of the individual shish-kebabs. When connected, forces are exerted between shish-kebabs that equalize their migration speeds. This connector force exerted on one shish-kebab to bring its speed up (or down) to that of the whole sub-chain is countered by an equal and opposite connector force that this shish-kebab exerts on the rest of the sub-chain, bringing the velocity of the rest of the sub-chain down (or up) to that of the one shish-kebab. Since the translational drag coefficient of a thin filament moving orthogonal to its axis is roughly twice that of one moving parallel to its axis [59], this effect can easily be accounted for by including a weighting factor that is calculated using this drag coefficient in the averaging of the velocities of the isolated shish-kebabs. The ensemble-averaged center-of-mass mobility of the sub-chain can be evaluated as follows. Since each shish-kebab, say shish-kebab i, in a sub-chain, if isolated from the others, would have an orientation-dependent electrophoretic velocity which would differ from the velocity of the other shish-kebabs in the sub-chain, there must be a connector force $\boldsymbol{f}_i$ on shish-kebab i, which forces it to move at the center-of-mass velocity $\boldsymbol{V}$ of rest of the sub-chain. This connector force is just the drag force required to change the velocity of the shish-kebab from its velocity when isolated, namely $\boldsymbol{v}_i^{\mathrm{SK}}$, to the velocity of the rest of the sub-chain, namely $\boldsymbol{V}$. This drag force $\boldsymbol{f}_i$ is therefore proportional to $\boldsymbol{v}_i^{\mathrm{SK}} - \boldsymbol{V}$, and is dependent on the orientation of shish-kebab i. We can obtain it from the formula for the orientation-dependent drag force on a moving

cylinder, which is given by [59]

$$\begin{aligned} \boldsymbol{f}_i &= \zeta_{||}\boldsymbol{u}_i\boldsymbol{u}_i \cdot (\boldsymbol{v}_i^{\mathrm{SK}} - \boldsymbol{V}) + \zeta_{\perp}(\mathcal{I} - \boldsymbol{u}_i\boldsymbol{u}_i) \cdot (\boldsymbol{v}_i^{\mathrm{SK}} - \boldsymbol{V}) \quad (4.8) \\ &= \left[\zeta_{||}\boldsymbol{u}_i\boldsymbol{u}_i + \zeta_{\perp}(\mathcal{I} - \boldsymbol{u}_i\boldsymbol{u}_i)\right] \cdot (\boldsymbol{v}_i^{\mathrm{SK}} - \boldsymbol{V}) = \mathcal{Z}_i \cdot (\boldsymbol{v}_i^{\mathrm{SK}} - \boldsymbol{V}), \quad (4.9) \end{aligned}$$

where $\zeta_{||}$ and $\zeta_{\perp}$ are the drag coefficient of a shish-kebab parallel and perpendicular to the axis of the shish-kebab and satisfy $\zeta_{\perp} = 2\zeta_{||}$. Here,

$$\boldsymbol{u}_i \equiv (\cos\theta_i, \sin\theta_i \cos\phi_i, \sin\theta_i \sin\phi_i)^T \quad (4.10)$$

is the unit orientation vector of the shish-kebab, and we define

$$\mathcal{Z}_i \equiv \left[\zeta_{||}\boldsymbol{u}_i\boldsymbol{u}_i + \zeta_{\perp}(\mathcal{I} - \boldsymbol{u}_i\boldsymbol{u}_i)\right] \quad (4.11)$$

to be the drag tensor of the shish-kebab. The term $\boldsymbol{u}_i\boldsymbol{u}_i$ can be explicitly written as:

$$\boldsymbol{u}_i\boldsymbol{u}_i = \begin{pmatrix} \cos^2\theta_i & \cos\theta_i \sin\theta_i \cos\phi_i & \cos\theta_i \sin\theta_i \sin\phi_i \\ \cos\theta_i \sin\theta_i \cos\phi_i & \sin^2\theta_i \cos^2\phi_i & \sin^2\theta_i \cos\phi_i \sin\phi_i \\ \cos\theta_i \sin\theta_i \sin\phi_i & \sin^2\theta_i \cos\phi_i \sin\phi_i & \sin^2\theta_i \sin^2\phi_i \end{pmatrix}, \quad (4.12)$$

Since these connector forces are all internal forces, they must balance each other out (by Newtons third law) and sum to zero: $\sum_{i=1}^{N_K} \boldsymbol{f}_i = 0$, where N_K is the number of Kuhn steps in a sub-chain. Therefore, we find

$$\sum_{i=1}^{N_K} \mathcal{Z}_i \cdot \boldsymbol{V} = \sum_{i=1}^{N_K} \mathcal{Z}_i \cdot \boldsymbol{v}_i^{\mathrm{SK}}. \quad (4.13)$$

Since each shish-kebab in the sub-chain sees the same orientation distribution and $\mathcal{Z}_i$ becomes uncorrelated with $\boldsymbol{V}$ when N_K is large, we can replace the summations in

the above by N_K times the ensemble average of the orientation of each shish-kebab, giving

$$N_K\langle \mathcal{Z} \rangle \cdot \boldsymbol{V} \quad = N_K\langle \mathcal{Z} \cdot \boldsymbol{v}^{\mathrm{SK}} \rangle, \tag{4.14}$$

$$\text{or} \quad \langle \mathcal{Z} \rangle \cdot \boldsymbol{V} \quad = \langle \mathcal{Z} \cdot \boldsymbol{v}^{\mathrm{SK}} \rangle, \tag{4.15}$$

where we omit the index i as a result of the ensemble averaging:

$$\langle A \rangle = \int_0^{2\pi} \int_0^{\pi} P(\theta, \phi) A \sin\theta d\theta d\phi, \tag{4.16}$$

and $P(\theta, \phi)$ is the orientation probability distribution for a shish-kebab. Note here that we neglect the orientation-correlation between neighboring shish-kebabs caused by the bending elasticity of the chain. To obtain the ensemble averages, we now assume that this sub-chain is under a fixed stretching force $F^{\mathrm{str}}(s)$ that stretches the sub-chain to an average stretch ratio s/L (L: maximum stretch) in the x-direction (i.e. the field direction). As mentioned above, the electric field $\boldsymbol{E}$ is assumed to be spatially uniform over this sub-chain (or spring), although the field is varying over the length of the whole molecule, which is what leads to polymer stretching. The ensemble average of shish-kebab angles can be calculated from a Boltzmann distribution:

$$P(\theta, \phi) = \frac{1}{Z} \exp\left\{ F^{\mathrm{str}}(s) L_K \cos\theta / k_B T \right\}, \tag{4.17}$$

where L_K is the Kuhn step length. For DNA, we employ the worm-like chain (WLC) spring law [60, 61] for the stretch force:

$$F^{\mathrm{str}}(s) = \frac{k_B T}{L_K} \left\{ \left(1 - \frac{s}{L}\right)^{-2} - 1 + 4\frac{s}{L} \right\}, \tag{4.18}$$

Now, $\langle \mathcal{Z} \rangle$ can be calculated as follows (using $\zeta_\perp = 2\zeta_{||}$):

$$\begin{aligned}
\langle \mathcal{Z} \rangle &= \zeta_{||} \langle \boldsymbol{uu} \rangle + \zeta_\perp (\mathcal{I} - \langle \boldsymbol{uu} \rangle) && (4.19)\\
&= \zeta_{||} (2\mathcal{I} - \langle \boldsymbol{uu} \rangle) && (4.20)\\
&= \begin{pmatrix} 2 - \langle \cos^2\theta \rangle & 0 & 0 \\ 0 & 2 - \langle \sin^2\theta \cos^2\phi \rangle & 0 \\ 0 & 0 & 2 - \langle \sin^2\theta \sin^2\phi \rangle \end{pmatrix}. && (4.21)
\end{aligned}$$

Using the electrophoretic velocity of a shish-kebab in Eq. 4.7, the term $\langle \mathcal{Z} \cdot \boldsymbol{v}^{\mathrm{SK}} \rangle$ is evaluated as,

$$\begin{aligned}
\langle \mathcal{Z} \cdot \boldsymbol{v}^{\mathrm{SK}} \rangle_x &= \langle \zeta_{||} (v_x^{\mathrm{SK}} \cos^2\theta + v_y^{\mathrm{SK}} \cos\theta \sin\theta \cos\phi + v_z^{\mathrm{SK}} \cos\theta \sin\theta \sin\phi)\\
&+ \zeta_\perp \left\{ v_x^{\mathrm{SK}} (1 - \cos^2\theta) - v_y^{\mathrm{SK}} \cos\theta \sin\theta \cos\phi - v_z^{\mathrm{SK}} \cos\theta \sin\theta \sin\phi \right\} \rangle\\
&= \zeta_{||} \langle v_x^{\mathrm{SK}} (2 - \cos^2\theta) - v_y^{\mathrm{SK}} \cos\theta \sin\theta \cos\phi - v_z^{\mathrm{SK}} \cos\theta \sin\theta \sin\phi \rangle\\
&= \langle \left\{ \mu_0 E + \mu_1 E (3\cos^2\theta - 1) \right\} (2 - \cos^2\theta) \rangle \zeta_{||}\\
&- \mu_1 E \langle 3\cos^2\theta \sin^2\theta \cos^2\phi \rangle \zeta_{||} - \mu_1 E \langle 3\cos^2\theta \sin^2\theta \sin^2\phi \rangle \zeta_{||}, && (4.22)\\
\langle \mathcal{Z} \cdot \boldsymbol{v}^{\mathrm{SK}} \rangle_y &= 0, && (4.23)\\
\langle \mathcal{Z} \cdot \boldsymbol{v}^{\mathrm{SK}} \rangle_z &= 0. && (4.24)
\end{aligned}$$

From the relation $\langle \mathcal{Z} \rangle \cdot \boldsymbol{V} = \langle \mathcal{Z} \cdot \boldsymbol{v}^{\mathrm{SK}} \rangle$, we find

$$\begin{aligned}
V_x &= \mu_0 E + \mu_1 E \left\{ \frac{\langle (3\cos^2\theta - 1)(2 - \cos^2\theta) \rangle}{\langle 2 - \cos^2\theta \rangle} - 2 \frac{\langle \frac{3}{2} \cos^2\theta \sin^2\theta \rangle}{\langle 2 - \cos^2\theta \rangle} \right\}\\
&= \left[\mu_0 + 2\mu_1 h \left\{ F^{\mathrm{str}}(s) L_K / k_B T \right\} \right] E, && (4.25)\\
V_y &= 0, && (4.26)\\
V_z &= 0, && (4.27)
\end{aligned}$$

where the function $h(x)$ is defined as $h(x) = -2 + 3x^2/\{-2 + x^2 + 2x\coth(x)\}$. The function $h(x)$ monotonically increases from -0.2 to 1 when x varies from 0 to infinity. If we define $\mu_{\mathrm{EP,HI}}$ to be the EP mobility with the effect of electrohydrodynamic interactions included, we can conclude from Eq. 4.25 that

$$\mu_{\mathrm{EP,HI}} = \mu_0 + 2\mu_1 \; h\left\{F^{\mathrm{str}}(s)L_K/k_BT\right\}. \tag{4.28}$$

Since $h(x)$ is negative when $0 < x < 2.4$, $\mu_{\mathrm{EP,HI}}$ becomes smaller than μ_0 when the stretch of a sub-chain is small. This occurs because for small stretch there are many shish-kebabs oriented perpendicular to the field, and these have a reduced contribution to the EP mobility relative to the mobility μ_0 of isolated spheres (see Eq. 4.7), and also have larger weighting factors for the overall center-of-mass velocity of a sub-chain than ones parallel to the field. From Eq. 4.28, and the fact that $h(x)$ varies between -0.2 to 1 as the chain is stretched, we find that the EP mobility of a highly stretched sub-chain can be enhanced by 66% over the EP mobility of a coiled (or unstretched) sub-chain when $\mu_1 = \mu_0/4$, which should hold when $\kappa a \lesssim 1$. Note that the hydrodynamic interaction from the elastic forces under uniform stretch of the sub-chain can be ignored because they do not induce any center-of-mass migration of the sub-chain. With this expression for the mobility of each sub-chain, the dynamics of the full polymer chain, which is the fourth and final level of the hierarchical description, can be written down. This can include the effects of Brownian motion, which would allow one to simulate the detailed stretching dynamics of ensembles of chains electrophoresing in a non-uniform field (see Appendix A). Here, however, we are only interested in estimating the stretch dependence of the mobility, and in comparing this estimate with our experimental results. To keep the estimate simple, we will therefore assume that the stretch and the field $\boldsymbol{E}$ are uniform along the whole chain (not just the sub-chain), and use Eq. 4.28 to estimate the stretch dependence of the mobility.

In reality, since it is a gradient in the electric field that stretches the chain, the chain stretch is not expected to be completely uniform along the molecule. Accounting for this non-uniformity is beyond the scope of this paper, however. By examining the predicted field gradient in the channel, we find that even when the molecule is stretched to the largest degree observed here (around $14\mu m$), the electric field varies by only around 18% over the length of the molecule. This modest variation in field helps justify our neglect of the non-uniformity of the stretch and our calculation of the mobility of the molecule using the magnitude of the field at the center of the molecule.

We note that a related approach to inclusion of electrohydrodynamic interactions has been presented by Butler et al. [62]. Their approach was directed towards explaining the electric-field-induced migration of DNA chains towards or away from the walls of thin channels, rather than towards the stretching phenomenon considered here. Their equations, while similar to ours (including the use of our Eq. 4.1 for the electrohydrodynamic disturbance field), were applied globally to a dumbbell model of the polymer, rather than locally to small segments within a single Kuhn length of the chain, as we do here. It is noteworthy that the paper of Butler et al. addressed experiments conducted at very low salt concentrations (much lower than the 10mM used in our experiments). Since we choose μ_0 and μ_1 for a shish-kebab to be consistent with the ratio of the electrophoretic mobilities of an infinite cylinder oriented parallel to the field and perpendicular to the field, which holds over a wide range of salt concentration ($\kappa a \lesssim 1$), our model should be applicable to salt concentrations below millimolar, as well. However, if the salt concentration becomes so low that the Debye length becomes larger than the Kuhn step length L_K, then the electrohydrodynamic interactions between shish-kebabs becomes non-negligible, and our modeling approach, which neglects hydrodynamic interactions between shish-kebabs, is no longer appropriate. For DNA ($L_K \cong 100$nm), κL_K becomes order of one when

the salt concentration is reduced to 10μM.

4.3 Results and Discussion

4.3.1 Experimental results

Since DNA is negatively charged, the DNA EP mobility is by definition negative. To analyze our experimental data, we first divide all EP mobility data into two groups based on the "visual length" of DNA, which is the length observed by microscopy and represents the degree of molecular stretch. The visual length of unstretched coiled DNA we observed in the experiment is less than around $3\mu m$. Therefore, we first choose the cutoff of $3\mu m$ to classify DNA into "unstretched" and "stretched". We present a histogram of EP mobilities for these two groups in Fig. 4.3. The percentage of chains within each mobility bin is given by the height of the corresponding bar. It is clear that the EP mobility increases, on average, when the DNA is stretched. Although the range of DNA mobilities spans from -0.05 to -0.37 $(10^{-8}m^2/sV)$, the average values in the stretched and unstretched states are -0.226 ± 0.060 and -0.147 ± 0.055, respectively. We next scatter plot the EP mobilities versus the visual extended DNA length for all DNA data in Fig. 4.3. (Note that the *magnitude* of the EP mobility increases downwards along the ordinate of Fig. 4.3, because it is negative in sign.) The EP mobility is clearly not monotonic with respect to the visual length in the coil-stretch transition.

There is a large scatter in the data in Fig. 4.3 that can be partially reduced by correlating EP mobility with molecular conformation. In a hydrodynamically driven elongational flow, Perkins et al. [63] observed seven different DNA conformations: coiled, dumbbell, half-dumbbell, folded, uniform, kinked, and extended. In our study, five similar, but not necessarily identical, conformation types are found in the converg-

ing electrophoretic flow. We therefore classify our EP mobility data into five groups according to their conformations: 1- coiled, 2- oval, 3- folded, 4- half-dumbbell, and 5- extended, with individual snapshots illustrating these conformations in Fig. 4.4. Because of resolution limits, the folded conformation is not clearly distinguishable from a partially extended conformation. Some of transitions between these conformations observed in the experiments are given in the supplementary material. Based on this categorization, we examine the relationships between the conformation transition and the EP mobility. A slight elongation transforms a DNA conformation from a coiled sphere to an oval shape. Further elongation can unwind DNA into folded, half-dumbbell, and finally extended shapes. The EP mobility depends strongly on the instantaneous DNA conformation. According to Fig. 4.4, DNA with an oval shape has a much higher mobility than a coiled one. With increased visual length, the folded DNA attains a higher mobility magnitude than does the half-dumbbell or the extended ones.

In addition to the five conformations identified, we also highlight four EP mobility variation patterns in Fig. 4.4. Three dashed lines track data points with the increased visual length from the coiled shape to explain the EP mobility variation owing to a conformation transition: (i) from coiled to oval, (ii) from coiled to folded, and (iii) from coiled to folded to half-dumbbell and then extended. The change of EP mobility depends on these conformational transitions as shown in Fig. 4.4. The EP mobility varies the most in pattern (i), followed by pattern (ii) and then pattern (iii). Therefore, "molecular individualism" affects not only the conformation transition in the coil-stretch process but also the EP mobility variation in electrophoresis. The fourth pattern (iv) highlighted by the dashed circle is a "chain wiggling" phenomenon observed in extended DNA molecules. A movie showing this is provided in the supplementary material. The wiggling motion leads to a lower EP mobility, presumably because of higher energy dissipation.

4.3.2 Theoretical results

4.3.2.1 Electrophoretic mobilities of linear, U-shaped and W-shaped DNA

Since we assume that all shish-kebab segments have the same ensemble average orientation for a linearly stretched DNA, our theory does not apply directly to conformations with non-uniform stretch such as dumbbell, half-dumbbell, or partially folded shapes. However, we still can calculate the mobility as a function of stretch ratio for evenly folded DNA chains such as a DNA with a U-shaped or a W-shaped stretch. If a U-shaped DNA at the steady state, which has a sharp bend at the middle of the chain, is cut at the middle into two pieces, then both pieces should migrate without changing their stretches at the same speed as the original U-shaped DNA, since the two pieces maintain the same force distribution in every section as the original. The only the difference in mobility between a linearly stretched and a U-shaped molecule should then be the contour length. Therefore, the EP mobility of a U-shaped DNA is calculated simply by cutting the maximum stretch L down to$L/2$ in Eq. 4.18. Similarly, the EP mobility of a W-shaped DNA is calculated by cutting the maximum stretch down to $L/4$. If we assume that the linearly stretch, U-shaped, and W-shaped conformations in the modeling can be interpreted, respectively, as the extended, folded, and oval shapes observed in the experiments, we can compare the results of experiment and modeling. Figure 4.5 shows the enhancement of the EP mobility by for linear, U-shaped, and W-shaped stretch based on our theory, whose trend agrees well with the experimental result in Fig. 4.4. Note that both μ_0 and μ_1 are negative for DNA. We also find that a more condensed structure (W and U-shape) has a higher mobility than does the straight stretch shape, again in agreement with our experimental observations.

4.3.2.2 Comparison with the experiment

Since the Debye thickness κ^{-1} is around the range of $1 \sim 3$nm [45], which is comparable to the local radius of DNA chain, in our experimental condition, κa is order of one. Therefore, we expect $\mu_1 = \mu_0/4$ and the EP mobility of a highly stretched DNA is enhanced by 66% from the EP mobility of an unstretched DNA. By choosing $(\mu_0, \mu_1) = (0.2, 0.05) \times 10^{-8} m^2/sV$, the EP mobilities of unstretched and fully stretched DNA become $0.18 \times 10^{-8} m^2/sV$ and $0.30 \times 10^{-8} m^2/sV$, respectively, with 66% enhancement. Also, the calculated EP mobility time dependence for W- and U-shaped molecules are close to the experimental EP mobility patterns (i) and (ii), respectively, in Fig. 4.4, if we interpret the "oval" experimental configuration to be a "W" shape and the "folded" configuration to be a "U" shape. The calculated EP mobility profile of the linearly stretched molecule, however, does not agree very well with pattern (iii) because the actual conformational transition in pattern (iii) is more complicated than the simple linear stretch, and "chain wiggling" is not considered in the model.

4.4 Concluding remarks

DNA mobility in free solution is usually assumed to be a constant because DNA remains unstretched in a coiled configuration in free solution if the electric field is uniform. In this study, however, we have investigated theoretically and experimentally the effect of electrohydrodynamic interactions on λ-DNA EP mobility in free solution in a microscale converging channel, which produces conformational changes that induce changes in DNA conformation and hence in its mobility. DNA molecules were stretched by the electric field gradient in the converging section, and the resulting conformations were observed and instantaneous DNA EP mobility was calculated. We found that stretching increased the EP mobility and the change of EP mobility

was conformation dependent. A shish-kebab model was proposed for each charged rigid charged "Kuhn step" of the DNA molecules and the shish-kebabs were linked into a freely-jointed chain model for the flexible DNA polymer. We ensemble averaged the orientations of each shish-kebab rod using a field-dependent Boltzmann distribution and the worm-like-chain spring law to relate the stretching force on the shish-kebabs to the overall chain stretch. Our modeling analysis shows that electrohydrodynamic interactions can enhance the EP mobility by stretching the DNA chains in a conformation-dependent manner. The results are qualitatively consistent with the experimental observations, and show that EP mobility changes in a history-dependent manner, depending on whether the DNA unravels in a linear shape, or in a "U" or "W" shape. These findings should be useful in interpreting and manipulating DNA mobility in complex geometries, including those used in biotechnological applications, such as gene delivery or DNA sequencing. In addition, we have presented equations for a more precise bead-spring model for DNA stretching and mobility in a non-uniform electric field.

4.5 Appendix

4.5.1 Brownian Dynamics Simulations

The dynamics of a charged polymer chain can be computed using a Brownian dynamics method by connecting sub-chains with stretch-dependent EP mobility $\mu_{\mathrm{EP,HI}}$ in Eq. 4.28, where now the field $\boldsymbol{E}$ varies from one sub-chain to the next. By modeling a polymer with beads with hydrodynamic drag and springs that connect beads and represent sub-chains (i.e. the bead-spring model), the dynamics of the full chain can be computed according to the following equation of motion of each bead including

the Brownian motion:

$$\boldsymbol{r}_i(t+\delta t) = \boldsymbol{r}_i(t) + \left\{ \sum_{j=1}^{N_b} \frac{\mathcal{H}_{ij} \cdot \boldsymbol{f}_j}{k_B T} + \mu_i \boldsymbol{E}(\boldsymbol{r}_i) \right\} \delta t + \sqrt{6\delta t} \sum_{j=1}^{i} \mathcal{B}_{ij} \cdot \boldsymbol{n}_j \qquad (4.29)$$

where $\boldsymbol{r}_i(t)$ is the position of a bead i at time t, $\mathcal{H}_{ij} = (\mathcal{B}_{ij} \cdot \mathcal{B}_{ij}^T)$ is the Rotne-Prager-Yamakawa (RPY) hydrodynamic interaction tensor, $\boldsymbol{f}_j$ is the spring force on bead j, N_b is the total number of beads in the polymer, μ_i is here the average EP mobility of the sub-chains adjacent to bead i, δt is the time increment in the simulation, $\boldsymbol{n}_j$ is a random vector whose components are chosen from the range $[-1, 1]$ in each time step, and $\boldsymbol{E}(\boldsymbol{r}_j)$ is the local electric field at bead j. With the above Eq. 4.29, it would be possible to simulate an ensemble of polyelectrolyte chains traversing a tapered channel. Results could then be binned together depending on stretch and conformation type (such as "U" or "W" conformations) and the average mobility for each bin could be computed and compared to experimental values. Given the limitations of the data reported here, however, such detailed simulations are beyond the scope of this work.

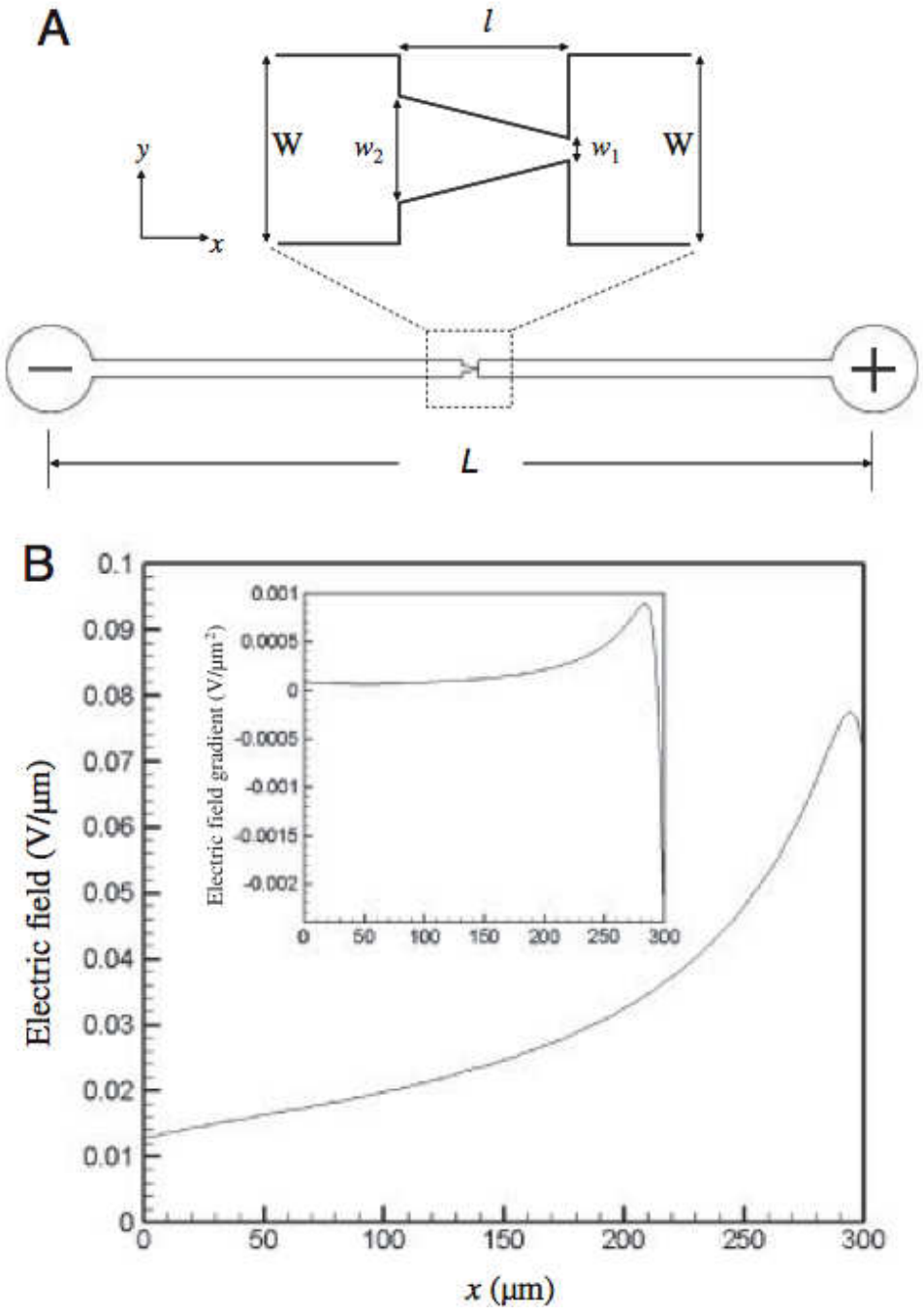

Figure 4.1: (A) Schematic diagram of the microscale converging channel. (B) The calculated electric field and electric field gradient along the converging channel central line.

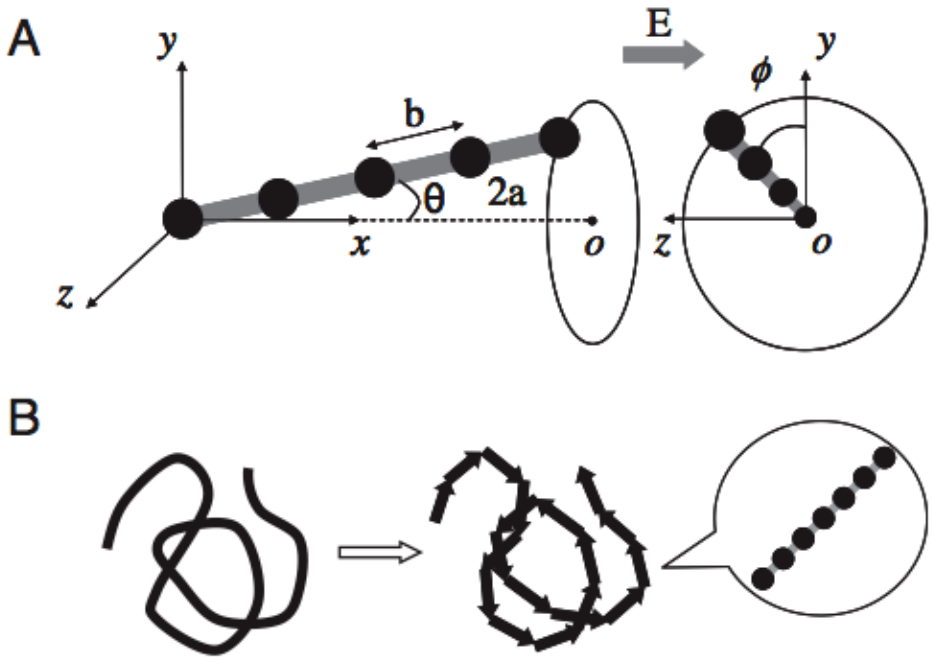

Figure 4.2: (A) Schematic diagram of shish-kebab model. (B) A freely jointed chain consisting of multiple charged "shish-kebab" segments.

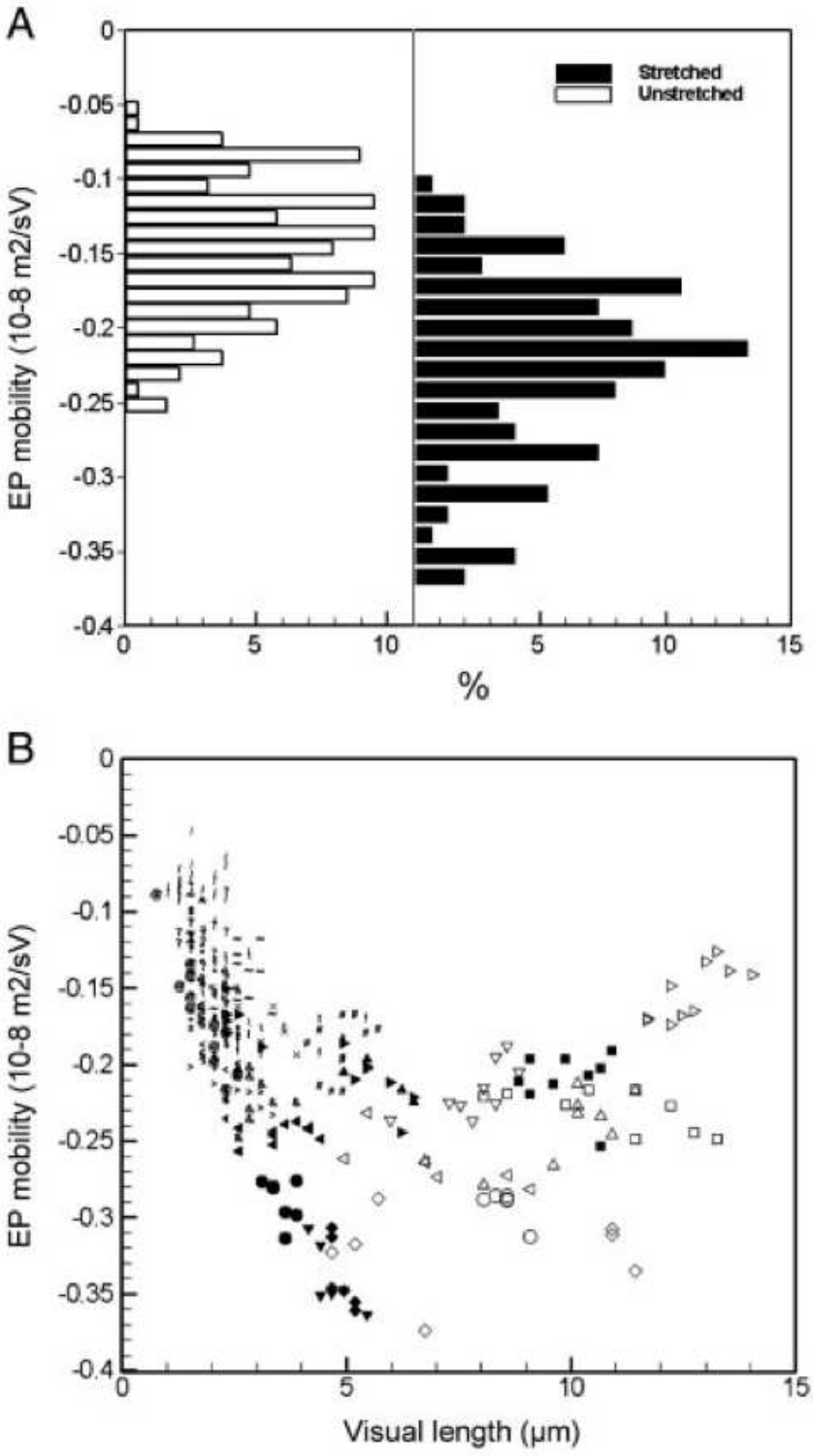

Figure 4.3: (A) Histogram of EP mobility for stretched and unstretched DNA. (B) Distribution of EP mobility versus DNA visual length. Each symbol type represents one tracked DNA molecules.

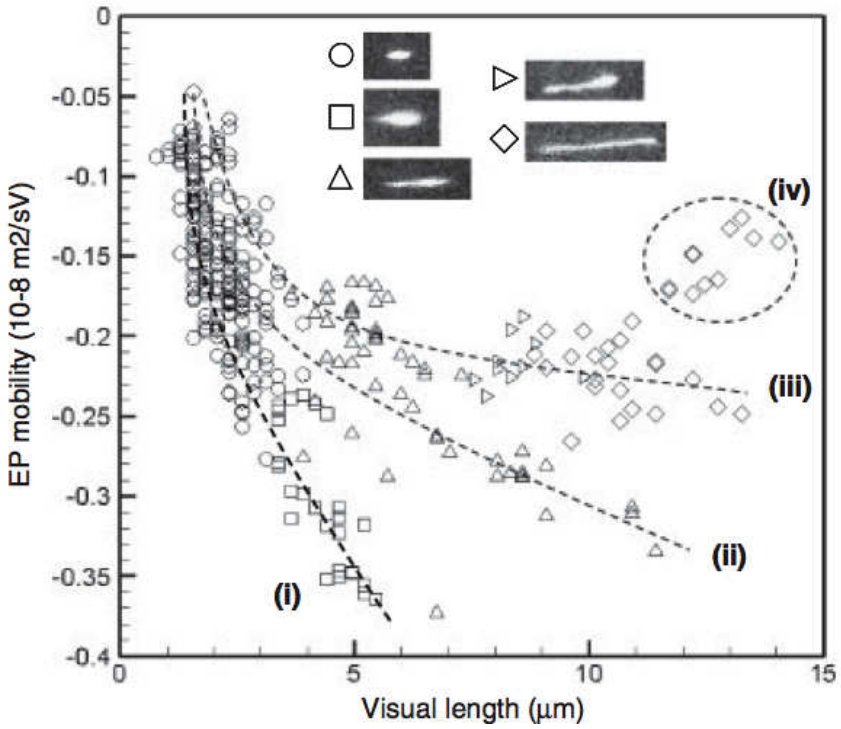

Figure 4.4: Distribution of EP mobility versus visual length for five DNA conformations. The fully stretched length of the DNA is around 20 μm. Different symbols correspond to DNA shapes depicted in the figure legend. (Circle: coiled, square: oval, triangle pointed upward: folded, rotated triangle pointed to the right: half-dumbbell, and diamond: extended). The three dashed lines mark three different unraveling paths typically taken by the molecules. The circled points correspond to "wiggling" conformations; see discussion in the text.

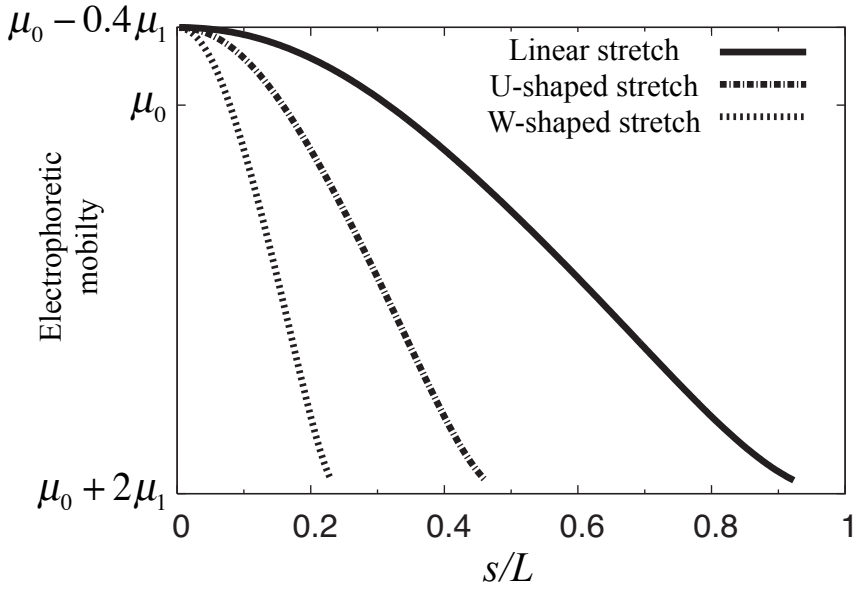

Figure 4.5: Theoretical estimation of the enhancement of the DNA EP mobility by stretching. Note that both μ_0 and μ_1 are negative for DNA. We expect $\mu_1 = \mu_0/4$ when $\kappa a \lesssim 1$.

CHAPTER V

The hydrodynamics of a run-and-tumble bacterium propelled by polymorphic helical flagella

5.1 Introduction

The peritrichous bacterium *Escherichia coli* is a well-studied example of a micro-swimmer in nature, which is able to change its swimming direction actively, showing "run-and-tumble" motion. A cell swims by rotating multiple helical flagella each attached by a hook to a rotary motor on the body [64, 65]. When all rotary motors rotate in the same direction, the cell swims forward (a"run" state). The cell changes direction by reversing the rotation of at least one of the motors (a"tumble" state). Although a tumble reorients the cell in a random direction, it is able to migrate stochastically towards a more favorable environment by changing the frequency of the reorientation depending on the gradient of the temperature or concentration of molecules of interest (i.e. sugars, amino acids, dipeptides) [64, 66].

The shape of the body of *E. coli* approximates a prolate spheroid with short and long axes of length 1μm and 2μm, respectively. A cell has an average of 3.4 flagella [65], each of which in the "normal" state is a left-handed helix with pitch of about 2.5μm and helix diameter of about 0.5μm [67]. Under a reversal of motor rotation direction, the flagellum transforms from normal to semicoiled (a right-handed helix with half the normal pitch but retaining the normal diameter) and then to curly 1 (a right-handed helix with half the normal pitch and half the normal diameter) [65,

67].

The hydrodynamics of a swimming *E. coli* is complex because of (i) the interactions of a cell body and multiple flagella, (ii) the translation-rotation coupling induced by the helical shape of the flagellum [68], and (iii) the polymorphic transformation of a flagellum under a reversal of the rotation of a motor. Although the swimming and the collective behavior of flagellar bacteria have been studied using the dipole model [69], the two-bead swimmer model [3, 70], the three-bead swimmer model [71, 72], the single-flagellum model [73–76], and the three-flagella model without a body and without polymorphic transformations [77], there has been no versatile model to deal with all these complexities.

Here, we discretize a flagellated cell with a bead-spring model and simulate its swimming process to obtain (a) the trajectories of a cell undergoing "run-and-tumble" motion, (b) the flow field around a cell in a run, (c) the effect of a nearby wall on its trajectory and hydrodynamics, and (d) the effect of polymorphic transformations on the efficiency of the reorientation.

The simulation results show the following: (a') The reversal of rotation of one rotary motor reorients a cell, thus the run-and-tumble motion leads to a random-walk trajectory. (b') The time-averaged flow field near a cell has double-layered helical streamlines, and the instantaneous flow has strong time-dependency and much larger magnitude than that of the time-averaged flow, large enough to make the Péclet number (ratio of flow advection to rate of diffusion of a particle) for sugar molecules larger than unity near a cell. (c') A cell near a wall swims clockwise when viewed perpendicular to the wall through the solvent and stays close to the wall in agreement with experiments and a theory for a single-flagellum model [74, 78, 79]. (d') The polymorphic transformation speeds the reorientation in a tumble motion.

5.2 Methods

We construct a bead-spring cell model with a body and multiple flagella by connecting beads with hydrodynamic radius a using three kinds of potentials: a spring potential ϕ_{s} that controls the distance between two adjacent connected beads, a bending potential ϕ_{b} that controls the bending angle formed by three connected beads, and a torsional potential ϕ_{t} that controls the torsional angle formed by four connected beads in a helical flagellum:

$$\boldsymbol{F}_{\mathrm{FF}}(\boldsymbol{r}_{ij}) = -\frac{\partial \phi_{\mathrm{s}}(r_{ij})}{\partial \boldsymbol{r}_{ij}} = H \, \frac{r_{ij}/L - 1}{1 - (1 - r_{ij}/L)^2 / s^2} \frac{\boldsymbol{r}_{ij}}{r_{ij}} \qquad (5.1)$$
$$\text{for } (1-s) < r_{ij}/L < (1+s),$$

$$\phi_{\mathrm{b}}(\theta_{ijk}^{\mathrm{bend}}) = -\frac{1}{2} k_{\mathrm{b}} \left(\cos\theta_{ijk}^{\mathrm{bend}} - \cos\theta_0^{\mathrm{bend}} \right)^2, \qquad (5.2)$$

$$\phi_{\mathrm{t}}(\theta_{ijkl}^{\mathrm{torsion}}) = -\frac{1}{2} k_{\mathrm{t}} \left(\theta_{ijkl}^{\mathrm{torsion}} - \theta_0^{\mathrm{torsion}} \right)^2, \qquad (5.3)$$

where i, j, k and l are indices of beads, $\boldsymbol{r}_{ij}$ is a vector connecting $\boldsymbol{r}_j$ (position vector of bead j) to $\boldsymbol{r}_i$, $\boldsymbol{F}_{\mathrm{FF}}(\boldsymbol{r}_{ij})$ is FENE-Fraenkel spring [80] with equilibrium length L and spring constant H, whose deformed spring length r_{ij} is restricted to a range set by the parameter s, k_{b} is the bending potential constant, $\theta_{ijk}^{\mathrm{bend}}$ is the bending angle formed by beads i, j and k, θ_0^{bend} is the equilibrium bending angle, k_{t} is the torsional potential constant, $\theta_{ijkl}^{\mathrm{torsion}}$ is the torsion angle formed by beads i, j, k and l which is computed with the method proposed in Ref. [81], and $\theta_0^{\mathrm{torsion}}$ is the equilibrium torsion angle. Additionally, we employ a spring-spring interaction potential ϕ_{ss} to prevent two springs from crossing each other [82], which is $\phi_{\mathrm{ss}}(D) = A_{\mathrm{ss}} \exp(-D/\alpha_{\mathrm{ss}})$, where A_{ss}, α_{ss} and D are the strength, the characteristic range of this potential, and the closest distance between springs, respectively. A discretized geometry is shown in Fig. 5.1, which contains 15 beads in the cell body and 15 in each of three flagella attached to

the body. Note that the shape of a body and each flagellum are kept nearly rigid with the employed potentials[1]. Although this level of discretization is too coarse to recover the theoretical mobility tensors quantitatively, the qualitative behavior of the motion is captured. The quantitative accuracy can be improved progressively by increasing the number of beads used, and we have found that using more beads does not change the qualitative results presented here. See the Appendix for an evaluation of the mobility tensors of the body and flagellum for different levels of discretization.

A hook that connects the body to a flagellum is modeled with three beads, one of them a body bead and the other two the first two flagellum beads (see Fig. 5.2). As long as the bending angle formed by these three beads $\theta_{\rm hook}^{\rm bend}$ is larger than 90°, no bending potential is applied to the flagellar hook because of its flexibility [66]. A bending potential $\phi_{\rm b}^{\rm hook}$ is applied for $\theta_{\rm hook}^{\rm bend} \leq 90°$ to keep the flagellum from intersecting the body:

$$\phi_{\rm b}^{\rm hook}(\theta_{\rm hook}^{\rm bend}) = 0 \qquad \text{if } \theta_{\rm hook}^{\rm bend} > 90°, \tag{5.4}$$

$$= -\frac{1}{2} k_{\rm b} \cos^2 \theta_{\rm hook}^{\rm bend} \qquad \text{otherwise.} \tag{5.5}$$

A hook propagates the twist generated by a rotary motor. A rotary motor twists the base of a flagellum and counter-rotates the body. Since the flagellum and the body are rigid enough to retain their shapes during swimming [65], we simply apply torques on each flagellum and the body to represent the action of a motor, and we don't explicitly model the mechanics of the motor or the time-dependent distortion of the hook that the motor produces. For the total torque and force to be zero, torques from a motor are distributed on three beads of a hook as shown in Fig. 5.2. First, torques $\boldsymbol{T}_1$ and $\boldsymbol{T}_2$ of identical magnitude T are applied, each of which points outward

[1] In a run, the time-average spring deformation is $(0.6 \pm 2.2)\%$, the time-average bending angle fluctuation is $(-0.1 \pm 4.2)°$, and the time-average torsional angle fluctuation is $(-1.3 \pm 2.7)°$. The values are the means $\pm$ standard deviations for simulation data of a cell in a run for 240τ.

from an end of the hook and tangent to this end. These torques represent the twist and the counter-twist induced by a rotary motor. Since these two torques are not colinear due to the variable bending angle of the hook, torques $-\boldsymbol{T}_1$ and $-\boldsymbol{T}_2$ are also applied on the hook so that the total torque is zero. A torque can be decomposed into a distribution of forces on three beads easily as shown in Fig. 5.2, and all four torques induced by a motor are distributed as forces on beads in and adjacent to the associated hook. An equivalent way of representing the torque balance would be to combine torques $-\boldsymbol{T}_1$ and $-\boldsymbol{T}_2$ into a single redirecting torque $\boldsymbol{T}_3$, which represents the torque generated by deformation of the hook that reorients the motor torque $\boldsymbol{T}_1$ into a torque $\boldsymbol{T}_2$ that rotates the flagellum. Our model assumes that the hydrodynamics of swimming controls the orientation of the flagella and the body; the elasticity of the hook merely serves to keep torques in balance[2].

The motion of each bead of a modeled cell at low Reynolds number is computed according to the following equation with the force distribution on beads obtained by adding forces associated with the torques from motors and all potential forces,

$$\boldsymbol{r}_i(t+\Delta t) = \boldsymbol{r}_i(t) + \left\{ \sum_{j=1}^{N} \mathcal{H}_{ij} \cdot \boldsymbol{f}_j \right\} \Delta t, \tag{5.6}$$

where $\boldsymbol{r}_i(t)$ is the position vector of bead i at time t, $\boldsymbol{f}_j$ is the summation of forces originating from the torques and potential forces on bead j, N is the total number of beads in a modeled cell, $\mathcal{H}_{ij}$ is the Rotne-Prager-Yamakawa (RPY) hydrodynamic interaction tensor [32, 33, 83], and Δt is the time increment in the simulation. By superposing the hydrodynamic interactions between beads, this equation with the force distribution on beads captures the dynamics of a discretized cell, which can change its geometry in the response to deformation of the flexible hooks, the distribution of

[2]It is assumed that the time required for the actual hook to bend and twist enough to generate this redirecting torque is small compared to the time for a run or tumble. This assumption is likely to be true, since otherwise the counter-rotation of the motor during a tumble would mainly undo the twist of the hook built up during a run rather than producing a counter-rotation of the flagellum.

torque-originated forces in and around the hooks, and the polymorphic transformation of the flagellum. Note that we ignore the effect of the Brownian motion.

For a run, all torques are applied in such a way that all flagella rotate counterclockwise when viewed from behind the cell. For a tumble, the torques $\boldsymbol{T}_1$ and $\boldsymbol{T}_2$ for one flagellum are inverted so that the flagellum rotates in the opposite way from the others. At the beginning of a tumble, the equilibrium bending and torsional angles of the flagellum attached to the motor are switched to the angles of semicoiled state, and at the middle of a tumble to the angles of curly 1 state in order to mimic the polymorphic transformations (see Table 5.1 for the angles).

We choose three input parameter with physical units: b (half the length of the long axis of the body, which is typically 1μm for *E. coli*), η (solvent viscosity), and T (magnitude of the torque given by a motor to each end of hook). Therefore, we scale length, time and energy with b, $\tau = \eta b^3/T$ and T, respectively. All parameters used in simulations are shown in Table 5.1.

5.3 Results

A typical trajectory of the center-of-mass position of a cell that undergoes run-and-tumble motion based on our simulations is shown in Fig. 6.10 with snapshots of the conformation of the cell in different states during the motion (see also Movie S1 in the Supporting Material). Since our simulated hook is flexible, the flagella can all take independent orientations with respect to the cell body, and the hydrodynamics of swimming dictate the flagellar orientations. In a run, three flagella spontaneously form a bundle and the cell swims straight[3], while in a tumble a reversal of a motor and the transformations of the associated flagellum trigger unbundling of the

[3]The period of rotation of the flagellar bundle around the swimming axis in a run is approximately 10.4τ and that of the cell body 22.4τ. The difference in rotation rate between the cell body and the flagellar bundle has been experimentally observed [65], and produces complex quasi-periodicity in the propulsion of a cell and in the associated flow field.

flagellum and reorientation of the cell. When the motor reverts to regular rotation, the flagella promptly rebundle and start a new run. This bundling-unbundling-rebundling sequence of flagella in run-and-tumble motion agrees with experimental observations [65]. Moreover, we find that the average change in direction during a tumble is enhanced by approximately 28% and 17% by the polymorphic transformations in tumbles of duration 200τ and 800τ, respectively, relative to the change in direction without these transformations[4].

By taking a time-average of the flow field near a cell with three flagella during a run, we obtain the time-averaged streamlines (see Figs. 5.4 and 5.5). The flow has a double-layered helical structure with three axisymmetric vortices, whose inner and outer streamlines around the body, the middle and the end of flagellar bundle all have different combinations of helicity and rotation. This flow decays as r^{-3} in the near field, and as r^{-2} in the far field (see Fig. 5.6) in agreement with that of the three-bead swimmer, and also when viewed from the direction perpendicular to the swimming axis, the time-averaged flow field is surprisingly similar to that of the three-bead swimmer model [71, 72], except that ours has an angular component of velocity around the swimming axis. In fact, the double-layered helical structure is a combination of the time-averaged flow of this three-bead swimmer and the angular velocity induced by the rotation of the bundle of flagella and the counter-rotation of the cell body. We find a similar flow field with the three-vortex structure when we shorten the flagella by a factor of two, lengthen it by 50%, change the geometric distribution of flagella on the body, refine the model of flagella using twice as many beads, or reduce the number of flagella to two. This time-averaged flow has a stagnation point behind the swimming cell and the far-field flow recovers the flow of the dipole model or two-bead swimmer model, which pushes fluid behind the swimmer opposite to the

[4]The change in direction produced by a tumble increases from $(12.5 \pm 0.4)^\circ$ to $(16 \pm 6)^\circ$ when the polymorphic transitions are added to a tumble of duration 200τ, and from $(62 \pm 6)^\circ$ to $(72 \pm 5)^\circ$ in a tumble of duration 800τ. The values are the means $\pm$ standard deviations averaged over 39 separate tumbles.

migration direction. This is because, in far-field, a swimming cell is a moving force dipole generated by the thrust from the rotating helical flagella and the drag force on the cell that is equal in magnitude and opposite in direction to the thrust.

We also visualized the instantaneous flow field around a swimming cell (Fig. 5.7 and Movie S2 in the Supporting Material) and found that this field is strongly time-dependent, and the magnitude of flow, which decays only as r^{-2}, is much larger in magnitude ($\times 10^{1\sim 2}$) than the time-averaged flow. It has been pointed out that the flow perturbation by swimming *E.coli* is too small compared to the rate of diffusion of chemoattractants, such as sugar molecules, to affect their transportation; in other words, the Péclet number (Pe) is less than unity ($Pe \simeq 10^{(-2)\sim(-1)}$) [84]. However, this Pe was calculated using the swimming velocity of *E.coli*, which is equivalent to the near-field time-averaged flow velocity. If we instead use the instantaneous velocity of the flagella, which is equivalent in magnitude to the instantaneous flow velocity near a swimming cell, we obtain,

$$Pe = \frac{\lambda\ 2\pi R f}{k_{\mathrm{B}} T/(6\pi\eta_{\mathrm{w}} a_{\mathrm{s}})} \simeq 2.3, \tag{5.7}$$

where λ and R are the pitch (2.5μm) and the helical radius (0.25μm) of a flagellum, respectively, f is the rotation rate (130Hz) [65], k_{B} and T are the Boltzmann constant and room temperature, η_{w} is the viscosity of water, and a_{s} is the radius of a sugar molecule ($\sim$nm). Thus, the time-dependent flow produced by flagellar motion can affect the migration of sugar molecules near a cell. There is a difference in magnitude between the swimming velocity and the instantaneous flow velocity near a cell because not all of the momentum of flagellar motion can be converted into the thrust of the cell, but some of it only agitates fluid near the cell.

Simulations were also performed for a cell near a wall by employing the RPY tensor with the wall effect included [85] and a short-range repulsive potential between each

bead and the wall with cut-off length $0.2b$. The simulation shows that a cell in a run near a wall swims clockwise when viewed perpendicular to the wall through the solvent and stays close to the wall in agreement with experiments [78]. It is also found that the time-averaged flow around a cell near a wall is complex, and when viewed from the direction perpendicular to the wall, the flow on the right side of the cell is different from that on the left side (see Fig. 5.8). This asymmetry in flow is likely the origin of the clockwise motion of the cell.

5.4 Discussion

Our simulation of a discretized cell thus reproduces the behavior of *E. coli* observed in experiments (i.e. the three-dimensional random-walk trajectory in run-and-tumble motion and the steady clockwise swimming near a wall) accounting for the essential mechanics of its swimming, such as the torque produced by a rotary motor, the torque redirection through flexible hooks and the polymorphic transformations of flagella. We also find that the time-averaged flow field near a cell has double-layered helical streamlines. Moreover, the instantaneous flow field has much larger magnitude than the time-averaged flow, so that the flow near a cell can enhance the transport of small-molecule chemoattractants. This new model, which can be refined by using more beads if more quantitative predictions are desired, strikes a balance between accuracy and simplicity that will permit it to be used to determine the migration behavior of particles near a swimming cell, cell-cell hydrodynamic interactions, the effect of the number and geometric distribution of flagella on migration, the mechanism of circular swimming near a wall, details of the tumbling motion, and the effect of the Brownian motion on swimming by adding a Brownian noise term [80] in Eq. 7.2.

5.5 Appendix A

To estimate the accuracy of the discretized model, the components of the mobility tensors of a discretized body along the long axis and of a flagellum along the axial direction were separately computed by applying a force or a torque, and then compared with the analytical solution for a prolate spheroid [86] and with the result of the resistive force theory (RFT) for the equivalent geometry of a flagellum of *E. coli* [74], respectively. The velocity and angular velocity of the body along the long axis or of the flagellum along the axial direction in the response to a force $F_{\rm m}$ and a torque $T_{\rm m}$ in the same direction can be written as,

$$\begin{pmatrix} V \\ \Omega \end{pmatrix} = \begin{pmatrix} \beta & \gamma \\ \gamma & \alpha \end{pmatrix} \begin{pmatrix} F_{\rm m} \\ T_{\rm m} \end{pmatrix}. \tag{5.8}$$

For a body of the geometry shown in Fig. 5.1, we found $\alpha^{\rm bs}/\alpha^{\rm th} = 1.7$, $\beta^{\rm bs}/\beta^{\rm th} = 1.1$ and $\gamma^{\rm bs} = \gamma^{\rm th} = 0.0$, where values with "bs" and "th" mean those obtained from the bead-spring model and from the theory, respectively. For a flagellum represented by a coarse model using 15 beads, we find $\alpha^{\rm bs}/\alpha^{\rm th} = 0.56$, $\beta^{\rm bs}/\beta^{\rm th} = 0.90$ and $\gamma^{\rm bs}/\gamma^{\rm th} = 0.12$. We can refine the discretized model by using more beads to obtain better agreement with the theoretical values of the mobility tensor. For example, for a flagellum with 75 beads of hydrodynamic radius $0.02b$, we find $\alpha^{\rm bs}/\alpha^{\rm th} = 0.76$, $\beta^{\rm bs}/\beta^{\rm th} = 1.1$ and $\gamma^{\rm bs}/\gamma^{\rm th} = 0.47$.

Parameter type	Symbol	Meaning	Value
Common	a	Radius of bead	0.1 b
	H	Spring constant	10 T/b
	s	Spring stretch parameter	0.1
	k_{b}	Bending potential constant	20 T
	k_{t}	Torsional potential constant	10 T
	-	Number of flagella on a cell	3
	Δt	Time increment in simulations	10^{-3}
Body	-	Number of beads	15
	L	Equilibrium spring length	$*$
	θ_0^{bend}	Equilibrium bending angle	$*$
Flagellum	-	Number of beads	15
	L	Equilibrium spring length	0.58 b
	θ_0^{bend}	Equilibrium bending angle	142°/90°/105° †
	$\theta_0^{\mathrm{torsion}}$	Equilibrium torsional angle	−60°/65°/120° †
	A_{ss}	Spring-spring potential constant	1.0 T
	α_{ss}	Characteristic range of spring-spring potential	0.2 b
	-	Cut-off length of spring-spring potential	0.2 b

$*$ See Fig. 5.1.

† Values for normal/semicoiled/curly 1 conformation, respectively.

The symbols b and T are half the length of the long axis of the body and the magnitude of the torque applied by a motor to each end of the hook.

Table 5.1: Parameters for simulations of modeled cell.

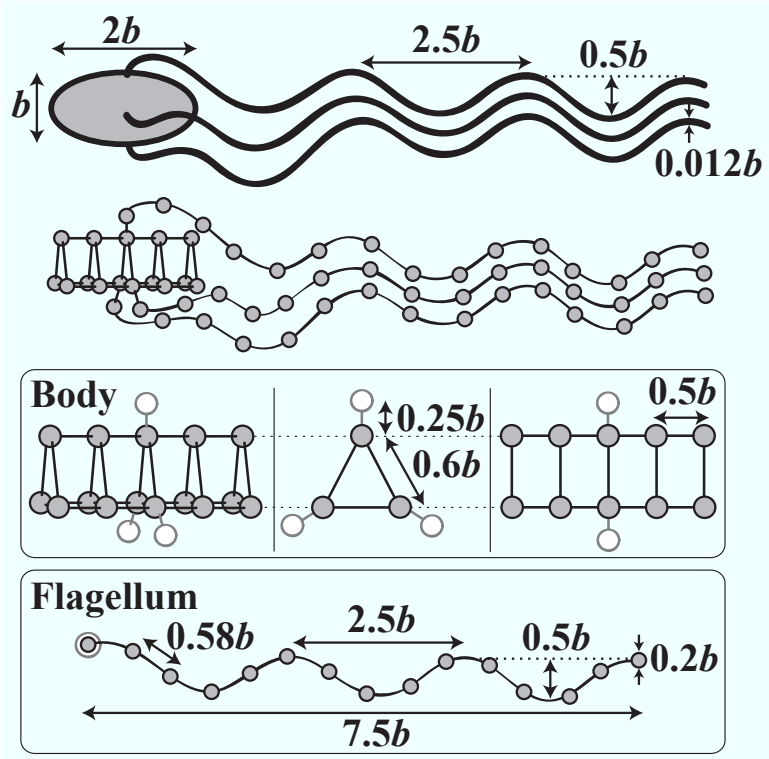

Figure 5.1: The geometry of *E. coli* with flagella of the normal state and the discretized model. b is half the length of the long axis of the body, which is the unit length scale in our simulation, and is typically 1μm for *E. coli*. Gray open circles in the diagram of the body represent the positions of first bead of each flagellum attached by a hook.

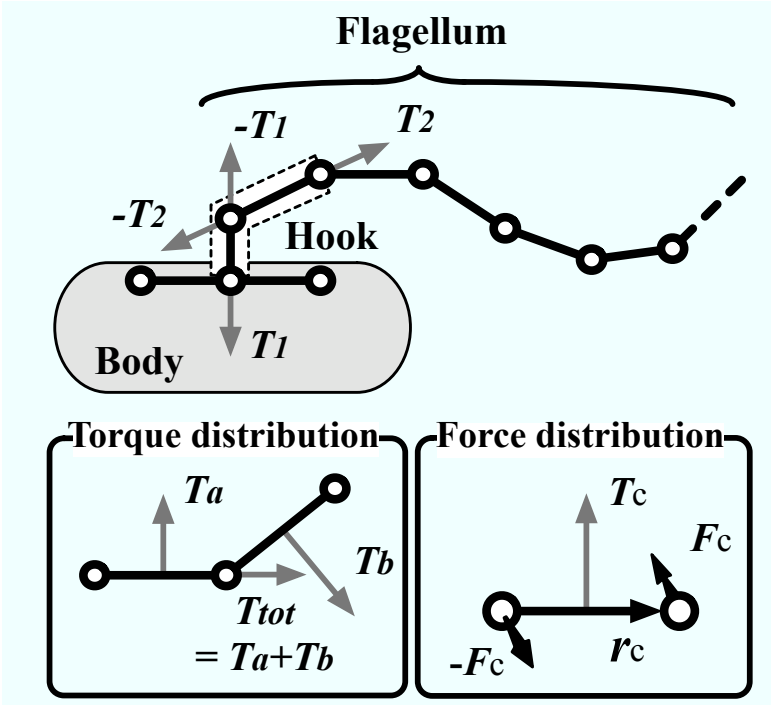

Figure 5.2: (Top) the model of a hook and the distribution of the torques from the action of a rotary motor. (Bottom left) the decomposition of a torque $\boldsymbol{T}_{\mathrm{tot}}$ into two torques $\boldsymbol{T}_{\mathrm{a}}$ and $\boldsymbol{T}_{\mathrm{b}}$, each of which is perpendicular to a spring. (Bottom right) the decomposition of a torque $\boldsymbol{T}_{\mathrm{c}}$ into a force couple $\boldsymbol{F}_{\mathrm{c}}$ and $-\boldsymbol{F}_{\mathrm{c}}$, with which $\boldsymbol{T}_{\mathrm{c}} = \boldsymbol{r}_{\mathrm{c}} \times \boldsymbol{F}_{\mathrm{c}}$ is satisfied.

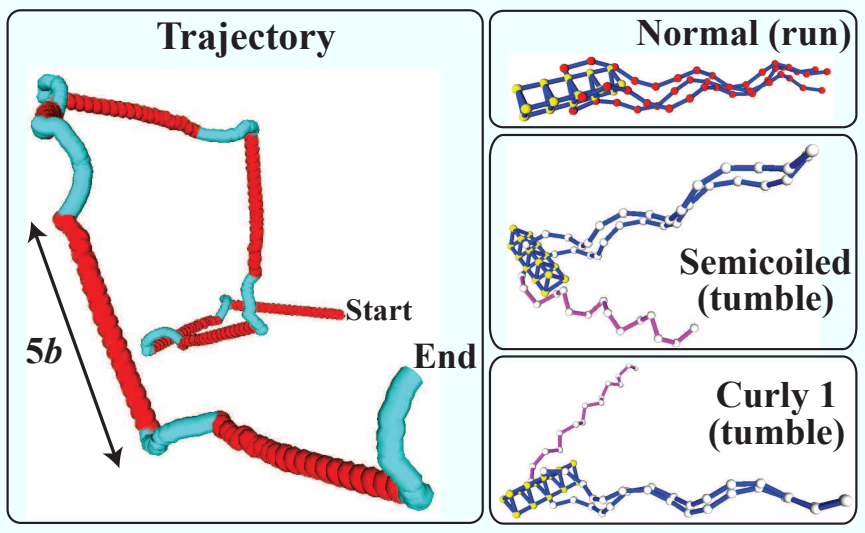

Figure 5.3: Typical trajectory of a modeled cell in run-and-tumble motion (left) and snapshots of cell conformations in different states during the motion (right). The red line in the trajectory represents a run state and the blue line a tumble state. The trajectory contains runs for 1200τ each and tumbles for 800τ each, the latter of which each consists of a semicoiled state for 400τ and a curly 1 state for 400τ.

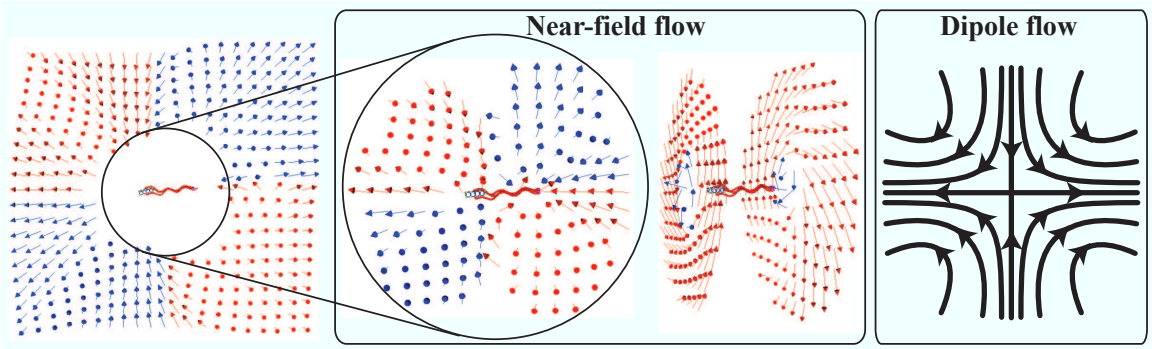

Figure 5.4: Time-averaged flow field around a modeled cell in a run. In this figure and Fig. 5.7, red arrows points into the paper and blue arrows the opposite. All arrows are unit flow-velocity vectors. In the near-field flow, all the shown velocity vectors have actual magnitude of velocity larger than $4.0 \times 10^{-5}\ b/\tau$. The far-field recovers the dipole flow (left), which is induced by a force dipole generated by the thrust from the rotating helical flagella and the drag force on the cell.

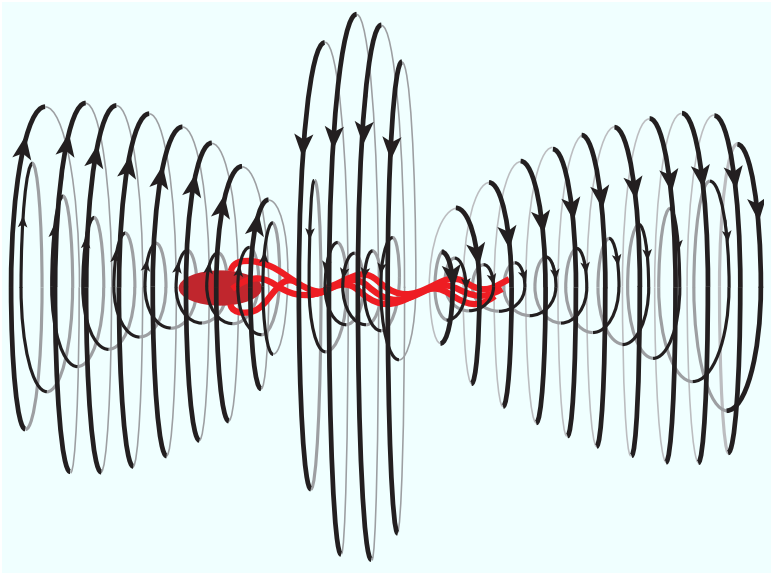

Figure 5.5: Streamlines implied by the near-field flow in Fig. 5.4.

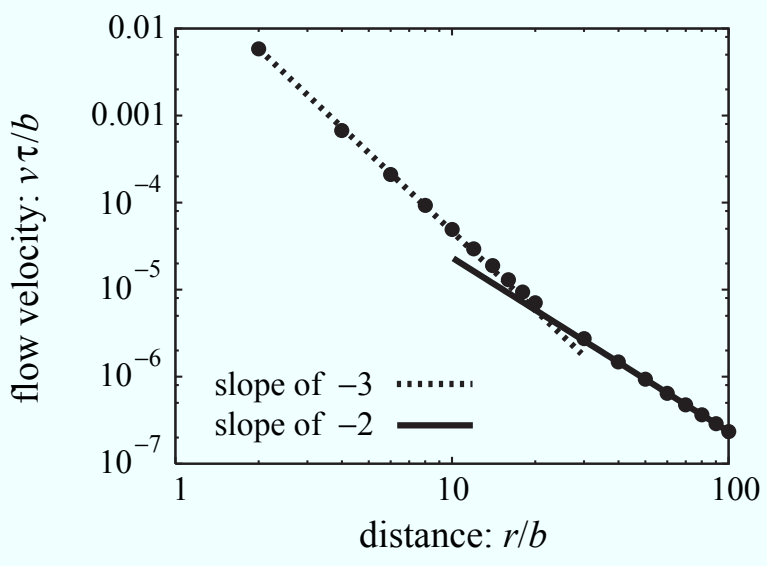

Figure 5.6: The decay of the magnitude of the time-averaged flow velocity v with distance. r is the distance from the center-of-mass $\boldsymbol{r}_{\rm cm}$ to a point on a plane that is perpendicular to the swimming axis and contains $\boldsymbol{r}_{\rm cm}$.

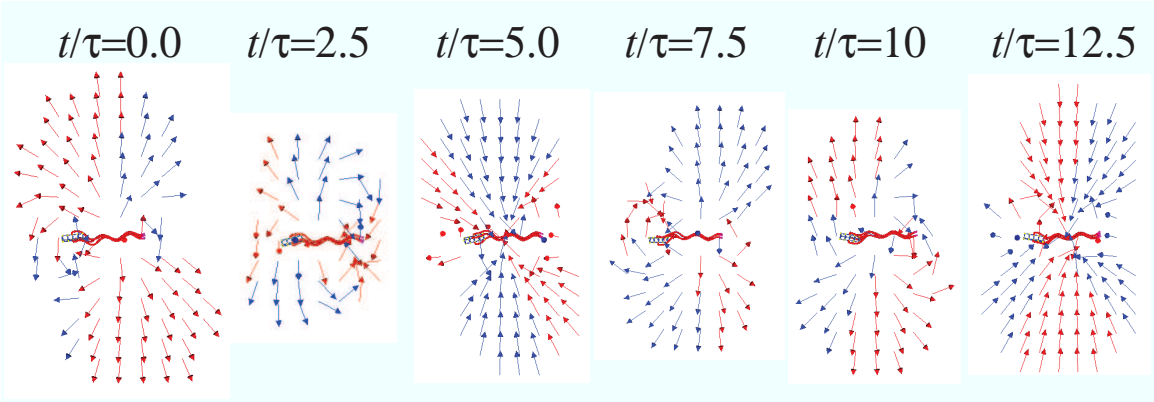

Figure 5.7: Time evolution of the flow field near a modeled cell. All arrows are unit flow-velocity vectors, each of whose actual magnitude of velocity is larger than $1.6 \times 10^{-3}\ b/\tau$. The period of rotation of the flagellar bundle around the swimming axis is approximately 10.4τ.

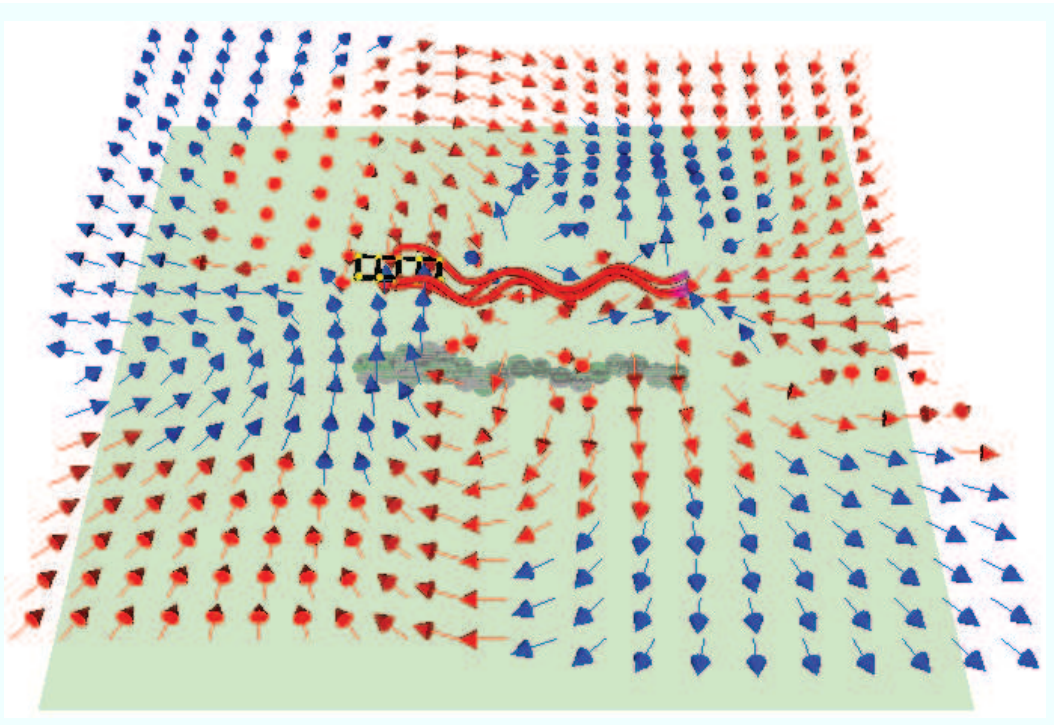

Figure 5.8: Time-averaged flow field around a modeled cell in a run near a wall. The cell and the shown velocity field are $2.7b$ away from the wall. Red arrows point toward the wall and blue arrows the opposite.

CHAPTER VI

Efficient models for micro-swimmers

6.1 Introduction

Micro-swimmers, including motile bacteria and artificial swimmers, swim at low Reynolds number by using a periodic non-reciprocal motion, i.e. motion lacking time-inversion symmetry. Since their motion is governed by the Stokes equation, which is linear, a reciprocal motion does not induce any time-average net migration of the center-of-mass [84]. Micro-swimmers break reciprocality of the motion, for example, by rotating one or more helical flagella attached to the cell body that counter-rotates as a result (e.g. *E. coli*), or by performing "power" and "recovery" strokes or the breaststroke motion with flagella (e.g. *Chlamydomonas*), or by propagating a wave on a flexible flagellum from the base of the cell body to the free end (e.g. sea urchin spermatozoon) [87]. These micro-swimmers can be categorized into "pullers", "pushers" or combinations of the two, depending on the swimming motion. We here define a puller/pusher as a micro-swimmer that on average pulls/pushes fluid to/away from the cell along the swimming axis over one period of its swimming motion. Examples of pullers are *Chlamydomonas* and *Chrysomonad*, and pushers include the sea urchin spermatozoon and *E. coli*. Some micro-swimmers, such as *E. coli* and *Chlamydomonas*, intersperse straight "running motion" with "tumbles" allowing them to reorient their movement stochastically towards a more favorable environment or possibly to reduce their chances of encountering predators [64, 88, 89]

The two-bead swimmer has been proposed as a simple model of a micro-swimmer to study the collective dynamics of the swimmers and their behavior near a wall [3, 70]. However, since the two-bead swimmer does not account for a periodic non-reciprocal swimming motion, it can not generate the time-dependent flow around the swimmer, which is stronger than the time-averaged flow [1] and which can induce synchronization of the swimming motions of multiple swimmers. Thus, the three-bead swimmer, which is the simplest model that accounts for a periodic non-reciprocal motion, has also been proposed [71] and used to study the interactions of multiple swimmers [72]. However, as we shall describe here, the swimming motion in these early studies on the three-bead swimmer is actually a combination of simpler puller and pusher swimming motions.

Here, we propose minimal one-, two- and three-dimensional puller/pusher micro-swimmer models, and two- and three-dimensional run-and-tumble swimming motions. By simulations using a bead-spring model, we find that the tumbling motion can be easily induced by breaking symmetry of the swimming motion with respect to the swimming axis.

Finally, we propose a five-bead swimmer as a minimal model for a swimmer with a helical flagellum and rotary motor attached to the cell body (i.e. "corkscrew swimmer" [84]). This five-bead swimmer accounts for the hydrodynamic effects of the rotation of the flagellum and the counter-rotation of the cell body as well as the periodic non-reciprocal swimming motion. It is found that this swimmer, when placed near a wall, reproduces the behavior of *E. coli*, which is attracted to the wall [69] and swims clockwise, when viewed perpendicular to the wall through the fluid [78], despite the fact that the swimmer does not have a helical tail nor helical motion.

6.2 Simulation method

Our minimal model of a one-dimensional swimmer consists of three colinear beads connected by two bonds whose lengths change in a non-reciprocal manner. This geometry is identical to that of previous studies [71, 72], but we induce different cycles (or periodic histories) of bond-lengths. Examples of non-reciprocal cycles of the two bond lengths, L_1 and L_2, that we impose are depicted in L_1-L_2 space in Fig. 6.1. This swimmer can swim at low Reynolds number by repeating a non-reciprocal cycle of bond-lengths.

We confirmed that the bond-length histories in Fig. 6.1 induce migration of the swimmer by simulations using the bead-spring model. In the simulations, three spherical beads with hydrodynamic radius a are connected by two FENE-Fraenkel springs [80] of time-dependent equilibrium lengths $L_1(t)$ and $L_2(t)$, which follow a configurational history shown in Fig. 6.1. The FENE-Fraenkel spring force $\boldsymbol{F}_{\mathrm{FF}}$ with equilibrium length L is written as:

$$\boldsymbol{F}_{\mathrm{FF}}(\boldsymbol{r}_{ij}) = H\,\frac{r_{ij}/L - 1}{1 - (1 - r_{ij}/L)^2/s^2}\frac{\boldsymbol{r}_{ij}}{r_{ij}} \qquad (6.1)$$
$$\text{for } (1-s) < r_{ij}/L < (1+s),$$

where i and j are indexes of beads, $\boldsymbol{r}_{ij}$ is a vector connecting $\boldsymbol{r}_j$ (position vector of bead j) to $\boldsymbol{r}_i$, H is the spring constant, and the deformed spring length r_{ij} is restricted to a range set by the parameter s, which is 0.01 in our simulations. The motion of each bead of the swimmer is computed according to the following equation with the

force distribution on beads given by the spring forces,

$$\boldsymbol{v}_i(t) = \sum_{j=1}^{N} \mathcal{H}_{ij}(\boldsymbol{r}_{ij}) \cdot \boldsymbol{f}_j, \tag{6.2}$$

$$\text{or} \quad \boldsymbol{r}_i(t+\Delta t) = \boldsymbol{r}_i(t) + \left\{ \sum_{j=1}^{N} \mathcal{H}_{ij}(\boldsymbol{r}_{ij}) \cdot \boldsymbol{f}_j \right\} \Delta t, \tag{6.3}$$

where $\boldsymbol{v}_i(t)$ is the velocity vector of bead i at time t, $\boldsymbol{r}_i$ is the position vector of bead i, $\boldsymbol{f}_j$ is the force on bead j, N is the total number of beads in the swimmer, Δt is the time increment in the simulation, and $\mathcal{H}_{ij}$ is a hydrodynamic interaction tensor. For $\mathcal{H}_{ij}$, we use the Oseen tensor [14] with the point-force approximation, or the Rotne-Prager-Yamakawa (RPY) tensor [32, 33] with more accurate hydrodynamics up to terms of order r_{ij}^{-3}.

By superposing the hydrodynamic interactions between beads, this equation with the spring forces on beads captures the dynamics of the swimmer. Although both cycles A and B in Fig. 6.1 induce migration of the center-of-mass at the same speed in the same direction, our simulations show that the resulting cycle-averaged flow fields differ. The far-field cycle-averaged flow of cycle A corresponds to that of a puller and cycle B to a pusher, and both flows decay as r^{-2}. The cycle-averaged flow of the pusher is surprisingly similar to that of a detailed bead-spring model of *E. coli* in a run [1] except that the flow of the three-bead swimmer does not have angular velocity components around the swimming axis (see Fig. 6.9).

By combining the cycle histories of the pusher and the puller, we can create a "square" history in L_1-L_2 space shown in Fig. 6.1:cycle C, which corresponds to the swimming motion of the Najafi Golestanian swimmer [71]. The cycle-averaged flow of this history is a combination of the flows of a puller and a pusher, which decays as r^{-3} because the dipole components of the flow cancel in a cycle that consists of puller and pusher swimming motions. It is also possible to generate a net puller or a pusher by setting different ranges for the changes in L_1 and L_2 [72] (i.e. by making

the "square" history into a "rectangular" one).

6.3 Migration speed of three-bead swimmer

Here, we evaluate the migration per cycle of a three-bead swimmer whose cycle is represented by an arbitrary closed path in L_1-L_2 space. Once a cycle motion is specified in L_1-L_2 space, the corresponding spring-force cycle in f_1^s-f_2^s space is also specified by Eq. 6.2, where f_i^s is the spring force connecting beads i and $i+1$, $\dot{L}_i$ is the time-derivative of L_i, and η is the solvent viscosity:

$$f_i^s = f_i^s(L_1, L_2, \dot{L}_1, \dot{L}_2, a, \eta). \tag{6.4}$$

Therefore, we can calculate the migration per cycle L_c requiring a cycle time T based on the histories of (L_1, L_2) and (f_1^s, f_2^s) as,

$$L_c = \int_0^T \frac{1}{3} \sum_{i=1}^{3} v_i(t) dt. \tag{6.5}$$

The migration per cycle does not depend on the cycle time T because of the linearity of the Stokes equation, and only depends on the cycle path in L_1-L_2 space (i.e. L_c is an invariant of a cycle). For example, if the time spent for a portion of a cycle becomes shorter (e.g. $\times 0.5$) following the same path, the migration speed becomes faster (e.g. $\times 2$). As a result, the migration during the portion of the cycle stays the same.

Now, we first calculate the migration for a small rectangular cycle, which we refer as C_r: (L_1, L_2)=(A, B)→$(A-\delta_1, B)$→$(A-\delta_1, B-\delta_2)$→$(A, B-\delta_2)$→(A, B). The Oseen tensor is used for $\mathcal{H}_{ij}$ in Eq. 6.2 to calculate the migration (L_r) and we find:

$$L_r = g(a, A, B)\delta_1\delta_2, \tag{6.6}$$

where $g(a, L_1, L_2)$ is a rational function (see Appendix A for the derivation), and $\delta_1, \delta_2 \ll a$. The contour plot of the function g is shown in Fig. 6.2. Note that $g(a, L_1, L_2)$ is always positive when the cycle is counter-clockwise (CCW) in L_1-L_2 space, and the migration along a clockwise (CW) cycle becomes $-L_r$. Since a cycle that does not enclose area in L_1-L_2 space induces no migration per cycle (i.e. the Scallop Theorem [84]), a cycle can be divided into two or more cycles whose migrations sum up to the migrations of the original cycle; see Fig. 6.3. Therefore, an arbitrary cycle can be divided into small rectangular cycles whose migrations sum to that of the original cycle, and the migration per arbitrary cycle (L_c) can be written as:

$$L_c = \iint_{\mathrm{A}} g(a, L_1, L_2) dL_1 dL_2, \tag{6.7}$$

where A is the area within the cycle. The result of L_c calculated using Eq. 6.7 for a CCW circular cycle centered at $(L_1, L_2) = (5a, 5a)$ with radius $0.5a < R_c < 3a$ is plotted in Fig. 6.4 along with our simulation results using the Oseen tensor and the RPY tensor. The theoretical result from Eq. 6.7 agrees well with the simulation results. Note that the simulation results obtained using the RPY tensor deviates from our theoretical results based on the Oseen tensor when R_c is large because the RPY tensor, which accounts for more accurate hydrodynamics, diverges from the Oseen tensor when the distance between beads becomes comparable to the bead radius a.

6.4 Dipolar-flow strength of three-bead swimmer

By taking advantage of the partitioning of a cycle described in the previous section, we here evaluate the cycle-averaged flow field around a swimmer. Once we find the analytical expression for the cycle-averaged flow for an arbitrary cycle, we can distinguish between puller and pusher swimming from the cycle path in L_1-L_2 space,

since its cycle-averaged far-field flow becomes dipolar as following:

$$\langle \boldsymbol{v}(\boldsymbol{r}) \rangle = \frac{p}{T} \left(3[\hat{\boldsymbol{n}} \cdot \hat{\boldsymbol{r}}]^2 - 1 \right) \frac{\hat{\boldsymbol{r}}}{r^2} + \mathcal{O}(r^{-3}), \tag{6.8}$$

where $\boldsymbol{r}$ is the position vector relative to the position of the center bead of a three-bead swimmer, $\hat{\boldsymbol{r}}$ is the unit vector of $\boldsymbol{r}$, $\hat{\boldsymbol{n}}$ is the unit vector pointing in the swimming direction, and p represents the strength of dipole, where the flow is that of a pusher when $p > 0$, that of a puller when $p < 0$, and neither a pusher nor a puller when $p = 0$. Note that the far-field fluid displacement per cycle $\boldsymbol{d}(\boldsymbol{r}) = T\langle \boldsymbol{v}(\boldsymbol{r}) \rangle$ is an invariant of a cycle. For a small CCW rectangular cycle C_r, the dipole strength p_r can be evaluated analytically in a similar way as in the previous section using the Oseen tensor, assuming $\delta_1, \delta_2 \ll a$ and $r \gg a$:

$$p_r = h(a, A, B)\delta_1\delta_2, \tag{6.9}$$

where $h(a, L_1, L_2)$ is a rational function (see Appendix A for the derivation). Since a cycle enclosing no area in L_1-L_2 space induces no cycle-averaged flow field, we can use the "cycle-division" to obtain the dipole strength induced by an arbitrary cycle:

$$p_c = \iint_{\mathrm{A}} h(a, L_1, L_2) dL_1 dL_2. \tag{6.10}$$

From the contour plot of the function $h(a, L_1, L_2)$ shown in Fig. 6.5, we find that 1) a cycle symmetric across the line $L_1 = L_2$ induces no dipolar flow and the perturbation flow decays as r^{-3}, which is the same as a Najafi-Golestanian swimmer, and 2) if a CCW cycle is entirely in the region $L_1 > L_2$, the cycle-averaged flow is that of a puller, and if entirely in $L_1 < L_2$, that of a pusher. The result of p_c calculated using Eq. 6.10 for a CCW circular cycle of radius $0.5a$ and centered at $(L_1, L_2) = (L_1^c, 5a)$ where $2a < L_1^c < 20a$ is plotted in Fig. 6.6 along with our simulation results using the Oseen

tensor and the RPY tensor. The theoretical result agrees well with the simulation results except that the simulation results with the RPY tensor diverges from the theoretical result because of its higher order accuracy compared to the Oseen tensor. Note also that if a CW cycle is entirely in the region $L_1 > L_2$, the cycle-averaged flow is that of a pusher, and if entirely in $L_1 < L_2$, that of a puller. A cycle-direction inversion (CCW $\leftrightarrow$ CW) reverses the migration direction ($+x \leftrightarrow -x$), and the sign of the flow dipole ($p_c \leftrightarrow -p_c$) as shown in Fig. 6.7. This is consistent with the fact that p_c (or the function $h(a, L_1, L_2)$) changes sign upon a reversal of the cycle-direction.

6.5 Rate of energy consumption of three-bead swimmer

The rate of energy consumption during a cycle can be written as:

$$\begin{aligned} e(s) &= f_1 v_1 + f_2 v_2 + f_3 v_3 \\ &= f_1^s (v_2 - v_1) + f_2^s (v_3 - v_2) = f_1^s \dot{L}_1 + f_2^s \dot{L}_2, \end{aligned} \tag{6.11}$$

where s is the distance coordinate along a cycle in L_1-L_2 space. Due to the linearity of the governing equation (i.e. the Stokes equation), each spring force is proportional to the time derivative of the spring length, $f_i^s = c_i(s)\dot{L}_i$. Using the chain rule of differentiation, we find:

$$\begin{aligned} e(s) &= c_1(s)\dot{L}_1^2 + c_2(s)\dot{L}_2^2 \\ &= c_1(s) \left(\frac{dL_1}{ds}\right)^2 \left(\frac{ds}{dt}\right)^2 + c_2(s) \left(\frac{dL_2}{ds}\right)^2 \left(\frac{ds}{dt}\right)^2 \\ &= \left(\frac{ds}{dt}\right)^2 \left[c_1(s) \left(\frac{dL_1}{ds}\right)^2 + c_2(s) \left(\frac{dL_2}{ds}\right)^2 \right]. \end{aligned} \tag{6.12}$$

Therefore,

$$\frac{ds}{dt} = \sqrt{e(s) \Big/ \left[c_1(s) \left(\frac{dL_1}{ds} \right)^2 + c_2(s) \left(\frac{dL_2}{ds} \right)^2 \right]}, \tag{6.13}$$

$$dt = ds \sqrt{\left[c_1(s) \left(\frac{dL_1}{ds} \right)^2 + c_2(s) \left(\frac{dL_2}{ds} \right)^2 \right] \Big/ e(s)}. \tag{6.14}$$

By integrating Eq.6.14 over a cycle, we obtain the cycle time T,

$$T = \oint \sqrt{\left[c_1(s) \left(\frac{dL_1}{ds} \right)^2 + c_2(s) \left(\frac{dL_2}{ds} \right)^2 \right] \Big/ e(s)} \; ds. \tag{6.15}$$

For a fixed cycle in L_1-L_2 space, ds/dt and T can be derived from Eq. 6.13 and 6.15 once $e(s)$ is specified. Since in the Stokes flow the rate of energy dissipation is quadratic in the velocity, It is easy to show that the most energy efficient cycle motion $s_{\text{eff}}(t)$ along a cycle in a cycle time T is achieved when the rate of energy consumption is constant through the cycle (see Appendix B for proof).

Assuming a constant rate of energy consumption e, the non-dimensional rate of energy consumption $\tilde{e}$ and the non-dimensional energy consumed per cycle $\tilde{E}$ can be defined as:

$$\tilde{e} = \frac{eT^2}{\eta a^3}, \tag{6.16}$$

$$\tilde{E} = \frac{ET}{\eta a^3}, \tag{6.17}$$

where $E = eT$, and these non-dimensional parameters only depend on the cycle path in L_1-L_2 space. Note that by setting e to be a constant through a cycle, its value can be easily calculated from Eq. 6.15 with given cycle time T.

6.6 Multi-dimensional swimmers

The swimming direction of the one-dimensional three-bead swimmer is restricted to one dimension because of its linear geometry. However, we can easily construct a two-dimensional swimmer by using beads that are not colinear (Fig. 6.1). Some micro-swimmers tumble and reorient the cell body by breaking symmetry of the swimming motion over the swimming axis. For example, *Chlamydomonas* swims straight with synchronous beating of two flagella and tumbles with asynchronous beating [88], and *E. coli* swims straight by rotating multiple helical flagella in a coherent rotational direction and tumbles by rotating at least one of the flagella in the reverse direction [64]. We confirmed by simulations using the bead-spring model with time-dependent equilibrium spring lengths analogous to the one-dimensional swimmer that our two-dimensional swimmer also tumbles by breaking symmetry of the swimming motion as shown in the cycle history in Fig. 6.1. Therefore, by alternating between the runs and tumbles, this two-dimensional swimmer can swim in a two-dimensional random-walk trajectory.

We can also create a three-dimensional swimmer by using four or more non-coplanar beads, for example, on the vertexes of a tetrahedron or "tetrumbbell" [90]. This three-dimensional swimmer can swim straight with a periodic non-reciprocal motion analogous to that of the two-dimensional swimmer and tumble by breaking symmetry of the swimming motion (see Fig. 6.1). It is worth noting that a tetrumbbell with constant equilibrium bond-lengths but different spring constants can migrate in a shear flow in the vorticity direction at low Reynolds number [90]. This migration (or "swimming") also results from a periodic non-reciprocal deformation induced by the shear flow on the tetrumbbell.

All of these models will be useful for studying the low Reynolds number hydrodynamics of micro-swimmers, the swimmer-swimmer interactions, and the collective dynamics of many swimmers. To study the multi-swimmer interactions of "corkscrew

swimmers" such as *E. coli*, however, we need to include the effect of the angular velocity around the swimmer induced by the rotation of the flagellum and the counter-rotation of the cell-body. In Fig. 6.8, we depict a five-bead swimmer that induces a time-average flow field corresponding to either a pusher or a puller plus this angular velocity. The five-bead swimmer swims via a periodic non-reciprocal motion of beads 2, 3 and 4, just as the three-bead swimmer does, by changing the bond-lengths L_1 and L_2. Additionally, torques $\boldsymbol{T}_1$ and $\boldsymbol{T}_2$, and counter-torques $-\boldsymbol{T}_1$ and $-\boldsymbol{T}_2$ are applied as shown in Fig. 6.8 to mimic the rotation of the flagellum and the counter-rotation of the cell-body. Note that, for the total torque to be zero, the magnitudes of torques $\boldsymbol{T}_1$ and $\boldsymbol{T}_2$ must be the same, and also that when beads 2, 3 and 4 are colinear, torques $-\boldsymbol{T}_1$ and $-\boldsymbol{T}_2$ cancel out. Each of these torques is first decomposed into two torques perpendicular to the bonds of the swimmer, and then each of these decomposed into forces on beads. For example, the force distribution on three connected beads i, j and k induced by a torque $\boldsymbol{T}_{\rm tot}$, which represents either $\boldsymbol{T}_1$, $\boldsymbol{T}_2$, $-\boldsymbol{T}_1$ or $-\boldsymbol{T}_2$, is (see Fig. 6.8),

$$\boldsymbol{F}_i = \frac{T_b}{r_{ij}} \frac{\boldsymbol{T}_{\rm tot} \times \boldsymbol{r}_{ij}}{|\boldsymbol{T}_{\rm tot} \times \boldsymbol{r}_{ij}|}, \tag{6.18}$$

$$\boldsymbol{F}_j = -\boldsymbol{F}_i - \boldsymbol{F}_k, \tag{6.19}$$

$$\boldsymbol{F}_k = \frac{T_a}{r_{jk}} \frac{\boldsymbol{T}_{\rm tot} \times \boldsymbol{r}_{ij}}{|\boldsymbol{T}_{\rm tot} \times \boldsymbol{r}_{ij}|}. \tag{6.20}$$

To restrict the deformation of the swimmer, bending potentials are applied: $\phi(\theta_{234}, 180^\circ)$, $\phi(\theta_{123}, \theta_{\rm e})$ and $\phi(\theta_{345}, \theta_{\rm e})$, where $\phi(\theta_{ijk}, \theta_0) = \frac{1}{2} k_{\rm b} (\cos\theta_{ijk} - \cos\theta_0)^2$, θ_{ijk} is the angle formed by beads i, j, and k, θ_0 is the equilibrium bending angle, $k_{\rm b}$ is the bending potential constant, and we choose $\theta_{\rm e} = 160^\circ$ for our simulations. Although the bending potentials allow small deformations of the swimmer [1], neither the time-averaged

[1] When the five-bead swimmer in Fig. 6.8 swims left to right with pusher motion, the magnitudes of time-averaged fluctuations of θ_{123}, θ_{234} and θ_{345} from the equilibrium bending angles are $\Delta\theta_{123} = (0.21 \pm 0.20)^\circ$, $\Delta\theta_{234} = (-8.0 \pm 1.6)^\circ$ and $\Delta\theta_{345} = (0.14 \pm 0.23)^\circ$, respectively. The values are the means $\pm$ standard deviations using bead-positions taken every 0.1τ over a period of 50τ. Simulation

flow field around the swimmer nor the swimming behavior are affected qualitatively for $k_{\rm b}$ values as large or larger than that used here. The time for L_1 and L_2 in a five-bead swimmer to traverse one side of a triangle in the configuration space is kept constant at the value t_0.

By solving Eq. 6.2 with the force distribution on beads obtained by adding together all forces associated with torques and all spring and bending forces, we obtain the time-averaged flow field around a five-bead pusher swimmer, which we find to be very similar to that obtained from a detailed bead-spring model (with 60 beads) of *E. coli* with multiple helical flagella in a run [1]. Input parameters with physical units in this simulation are R (maximum bond-length), η (solvent viscosity), and T (magnitude of torques). Therefore, we scale length and time with R and $\tau = \eta R^3/T$, respectively. We choose the simulation parameters a=0.2R, δ=0.5R, t_0=2.0τ, H=1000T/R, $k_{\rm b}$=2000T, $\theta_{\rm e}$=160° and Δt=$10^{-3}\tau$.

Simulations were also performed for the five-bead pusher near a wall by employing the RPY tensor with the wall effect included [85] and a short-range repulsive potential between each bead and the wall with cut-off length 0.2R. We find that the swimmer is attracted to the wall and swims clockwise (see Fig. 6.10) as observed in experiments and simulations with bacteria with helical flagella(um) (e.g. *E. coli*) [73, 74, 78], despite the fact that the five-bead swimmer does not have a helical tail nor helical motion. Therefore, the five-bead swimmer captures the experimentally observed behavior of *E. coli* qualitatively, and will allow us to simulate the collective dynamics of micro-swimmers more realistically than before at modest cost.

We also confirmed that a three-dimensional tumbling motion of the five-bead swimmer can be induced by temporarily connecting beads 2 and 4 with a FENE-Fraenkel spring of constant equilibrium length R while the bond-lengths L_1 and L_2 change in the same way as in a run, in other words, by forming a two-dimensional

parameters are a=0.2R, δ=0.5R, t_0=2.0τ, H=1000T/R, $k_{\rm b}$=2000T, $\theta_{\rm e}$=160° and Δt=$10^{-3}\tau$.

swimmer in a tumble with beads 2, 3 and 4. Simulations show that the trajectory of two five-bead pushers in a run, initially placed side by side and parallel to each other, agrees qualitatively with that obtained from a boundary element simulation of a modeled corkscrew swimmer, showing that two parallel swimmers first attract each other, and at the same time their swimming axes rotate in opposite directions [75]. We find that two side-by-side pullers behave similarly.

6.7 Summary and future directions

We have developed simple micro-swimmer models by extending the Najafi-Golestanian three-bead linear swimmer model to allow arbitrary history of bond-lengths (L_1, L_2), by making the beads noncolinear to introduce tumbling, and by adding two additional non-collinear end beads to which torque and counter-torque are applied to induce a helical flow field around it, thus mimicking the swimming of flagellated bacteria. We have shown that both the migration distance and optimum energy consumption per cycle is an invariant of the cycle path, and can be computed, respectively, by area and path integrals over the cycle. For three-bead swimmers, we have also developed a simple criterion to distinguish puller from pusher swimmers, based on the cycle in L_1-L_2 space. Finally, we have shown that our five-bead corkscrew swimmer spirals towards flat surfaces and interacts hydrodynamically with other five-bead swimmers in ways qualitatively similar to that of much more refined models of *E.coli*. These minimal models of micro-swimmers will help in the study of the collective dynamics of micro-swimmers with a simplified but qualitatively accurate hydrodynamics. These models can also be used to study the synchronization of multiple swimmers if the bond-lengths are changed by applying time-constant, equal and opposite forces on the beads at the ends of each bond until the bond-length reaches a designated length, as proposed in a previous work [91].

6.8 Appendix A: Analytical Expressions for the Migration and the Dipolar-Flow Strength Induced by a Small Rectangular Cycle

We analytically evaluate the migration per cycle induced by a small rectangular cycle C_r: $(L_1, L_2)=(A, B)\to(A-\delta_1, B)\to(A-\delta_1, B-\delta_2)\to(A, B-\delta_2)\to(A, B)$. Since the migration is independent of how the time is spent for strokes and determined only by the path in L_1-L_2 space because of the linearity of the governing equation, we assume the first stroke to be $(L_1, L_2) = (A - \frac{t}{T_1}\delta_1, B)$ where $0 < t < T_1$. By solving the following simultaneous equations derived from Eq. 6.2 with the Oseen tensor, we obtain $(f_1^s(t), f_2^s(t))$,

$$\dot{L}_1 = v_2 - v_1 = \frac{2f_1^s - f_2^s}{6\pi\eta a} + \frac{-2f_1^s + f_2^s}{4\pi\eta L_1} + \frac{f_2^s}{4\pi\eta L_2} + \frac{-f_2^s}{4\pi\eta(L_1+L_2)}, \tag{6.21}$$

$$\dot{L}_2 = v_3 - v_2 = \frac{2f_2^s - f_1^s}{6\pi\eta a} + \frac{-2f_2^s + f_1^s}{4\pi\eta L_2} + \frac{f_1^s}{4\pi\eta L_1} + \frac{-f_1^s}{4\pi\eta(L_1+L_2)}. \tag{6.22}$$

Then, we can calculate $(v_1(t), v_2(t), v_3(t))$ using $(f_1^s(t), f_2^s(t))$,

$$v_1 = \frac{-f_1^s}{6\pi\eta a} + \frac{f_1^s - f_2^s}{4\pi\eta L_1} + \frac{f_2^s}{4\pi\eta(L_1+L_2)}, \tag{6.23}$$

$$v_2 = \frac{f_1^s - f_2^s}{6\pi\eta a} + \frac{-f_1^s}{4\pi\eta L_1} + \frac{f_2^s}{4\pi\eta L_2}, \tag{6.24}$$

$$v_3 = \frac{f_2^s}{6\pi\eta a} + \frac{f_1^s - f_2^s}{4\pi\eta L_2} + \frac{-f_1^s}{4\pi\eta(L_1+L_2)}. \tag{6.25}$$

Finally, we find the center-of-mass migration velocity $v_{\mathrm{mig}}(t) = (v_1 + v_2 + v_3)/3$ to be

$$v_{\mathrm{mig}}(t) = \frac{a}{3}[-2L_1L_2(L_1+L_2)\{(2\dot{L}_1+\dot{L}_2)L_1^2 - (\dot{L}_1+2\dot{L}_2)L_2^2\}+$$
$$3a\{(2\dot{L}_1+\dot{L}_2)L_1^4+(2\dot{L}_1+\dot{L}_2)L_1^3L_2+(-\dot{L}_1+\dot{L}_2)L_1^2L_2^2-(\dot{L}_1+2\dot{L}_2)L_1L_2^3-(\dot{L}_1+2\dot{L}_2)L_2^4\}]/$$
$$\{-4L_1^2L_2^2(L_1+L_2)^2 + 4aL_1L_2(L_1+L_2)(L_1^2+3L_1L_2+L_2^2)+$$
$$3a^2(L_1^4 - 2L_1^3L_2 - 5L_1^2{L_2}^2 - 2L_1{L_2}^3 + {L_2}^4)\}. \tag{6.26}$$

Note that this solution for the migration velocity is different from that in Ref. [92] because we do not use approximation $a/L_i \ll 1$, which is used in their calculation.

We find the migration induced by the first stroke using Eq. 6.26,

$$\int_0^{T_1} v_{\rm mig}(t)dt = \frac{a\delta_1}{3}\{-2AB(-2A^3-2A^2B+AB^2+B^3)+ 3a(-2A^4-2A^3B+A^2B^2+AB^3+B^4)\}/ \{-4A^2B^2(A+B)^2+4aAB(A^3+4A^2B+4AB^2+B^3)+ 3a^2(A^4-2A^3B-5A^2B^2-2AB^3+B^4)\}+\mathcal{O}(\delta_1^2). \quad (6.27)$$

By adding up the migrations induced by the other three strokes in the cycle, which can be calculated in the same way, we find the total migration for this rectangular cycle to be $L_r = g(a,A,B)\delta_1\delta_2$, where $\delta_1, \delta_2 \ll a$ and $g(a,A,B)$ is

$$g(a,A,B) = \frac{1}{3}a\{16A^2B^2(A+B)^2(A^4+2A^3B+A^2B^2+2AB^3+B^4)+ 36a^2(A^2+3AB+B^2)(A^6+3A^5B+3A^4B^2+A^3B^3+3A^2B^4+3AB^5+B^6)- 27a^3(A+B)(2A^6+5A^5B+6A^4B^2-5A^3B^3+6A^2B^4+5AB^5+2B^6)- 12aAB(A+B)(4A^6+14A^5B+17A^4B^2+10A^3B^3+17A^2B^4+14AB^5+4B^6)\}/ \{-4A^2B^2(A+B)^2+4aAB(A+B)(A^2+3AB+B^2)+ 3a^2(A^4-2A^3B-5A^2B^2-2AB^3+B^4)\}^2. \quad (6.28)$$

The strength of the dipolar-flow induced by the same cycle C_r can be evaluated in a similar way by calculating the cycle-averaged flow:

$$\langle \boldsymbol{v}(\boldsymbol{r})\rangle = \frac{1}{T}\int_0^T \sum_{i=1}^{3} \mathcal{H}_{ij}(\boldsymbol{r}-\boldsymbol{r}_i(t))\cdot \boldsymbol{f}_i(t)dt \quad (6.29)$$

where $\boldsymbol{r}$ is the position vector originated at the position of the center bead of a

three-bead swimmer, and $\boldsymbol{r}_i(t)$ is obtained by $\boldsymbol{r}_i(t) = \boldsymbol{r}_i(0) + \int_0^t \boldsymbol{v}_i(t)dt$. We find the strength of dipolar flow to be $p_r = h(a, A, B)\delta_1\delta_2$ by comparing the result of Eq. 6.29 with Eq. 6.8 under conditions $\delta_1, \delta_2 \ll a$ and $r \gg a$, where $h(a, A, B)$ is

$$h(a,A,B) = \frac{1}{2}a^2(-A+B)\{-12aAB(A+B)(2A+B)(A+2B)(A^2+AB+B^2)^2+ 9a^2(A^2+3AB+B^2)(2A^3+3A^2B+AB^2+B^3)(A^3+A^2B+3AB^2+2B^3)+ 4A^2B^2(A+B)^2(2A^4+7A^3B+11A^2B^2+7AB^3+2B^4)\}/ \{-4A^2B^2(A+B)^2+4aAB(A+B)(A^2+3AB+B^2)+ 3a^2(A^4-2A^3B-5A^2B^2-2AB^3+B^4)\}^2. \quad (6.30)$$

6.9 Appendix B: Most Energy Efficient Cycle Motion of Three Bead Swimmer

Here, we show that the most energy efficient cycle motion $s_{\text{eff}}(t)$ along a cycle in a cycle time T is achieved when the rate of energy consumption is constant through the cycle. We show this by evaluating the change of the total energy consumed in a cycle when a portion of a cycle-motion is sped up and another is slowed down, while keeping the cycle time T constant. Let us change the time spent for two small line segments on a cycle, Δs_p and Δs_q, which is passed through during a small time interval ΔT, keeping the segment lengths constant.

$$\Delta T \to (1+\epsilon)\Delta T \qquad \text{in the segment } \Delta s_p. \quad (6.31)$$

$$\Delta T \to (1-\epsilon)\Delta T \qquad \text{in the segment } \Delta s_q. \quad (6.32)$$

As a result, we find the following changes:

$$\frac{\Delta s_p}{\Delta T} \to \frac{1}{1+\epsilon}\frac{\Delta s_p}{\Delta T},\ v_i \to \frac{v_i}{1+\epsilon},\ f_i^s \to \frac{f_i^s}{1+\epsilon} \qquad \text{in the segment } \Delta s_p, \tag{6.33}$$

$$\frac{\Delta s_q}{\Delta T} \to \frac{1}{1-\epsilon}\frac{\Delta s_q}{\Delta T},\ v_i \to \frac{v_i}{1-\epsilon},\ f_i^s \to \frac{f_i^s}{1-\epsilon} \qquad \text{in the segment } \Delta s_q. \tag{6.34}$$

These changes cause the changes in the rate of energy consumption,

$$e_p = \sum_{i=1}^{3} f_i v_i \to \frac{e_p}{(1+\epsilon)^2} \qquad \text{in the segment } \Delta s_p, \tag{6.35}$$

$$e_q = \sum_{i=1}^{3} f_i v_i \to \frac{e_q}{(1-\epsilon)^2} \qquad \text{in the segment } \Delta s_q. \tag{6.36}$$

The energy consumed in these segments becomes,

$$e_p \Delta T \to \frac{e_p}{(1+\epsilon)^2} \cdot (1+\epsilon)\Delta T = \frac{e_p}{(1+\epsilon)}\Delta T \qquad \text{in the segment } \Delta s_p, \tag{6.37}$$

$$e_q \Delta T \to \frac{e_q}{(1-\epsilon)^2} \cdot (1-\epsilon)\Delta T = \frac{e_q}{(1-\epsilon)}\Delta T \qquad \text{in the segment } \Delta s_q, \tag{6.38}$$

where e_p and e_q are the rate of energy consumption before the change of time interval in segments Δs_p and Δs_q, respectively. If we assume that the original rate of energy consumption are constant, or $e_p = e_q = e$, the change of the total energy consumed in a cycle after the change of time intervals is

$$\Delta E = \left\{ \frac{e\Delta T}{1+\epsilon} + \frac{e\Delta T}{1-\epsilon} \right\} - 2e\Delta T = 2\frac{\epsilon^2}{1-\epsilon^2} e\Delta T > 0. \tag{6.39}$$

Therefore, if the rate of energy consumption changes in the course of a cycle while keeping T constant, the energy consumed in a cycle increases. In other words, the most energy efficient cycle motion along a cycle in cycle time T is achieved when the rate of energy consumption is constant through the cycle.

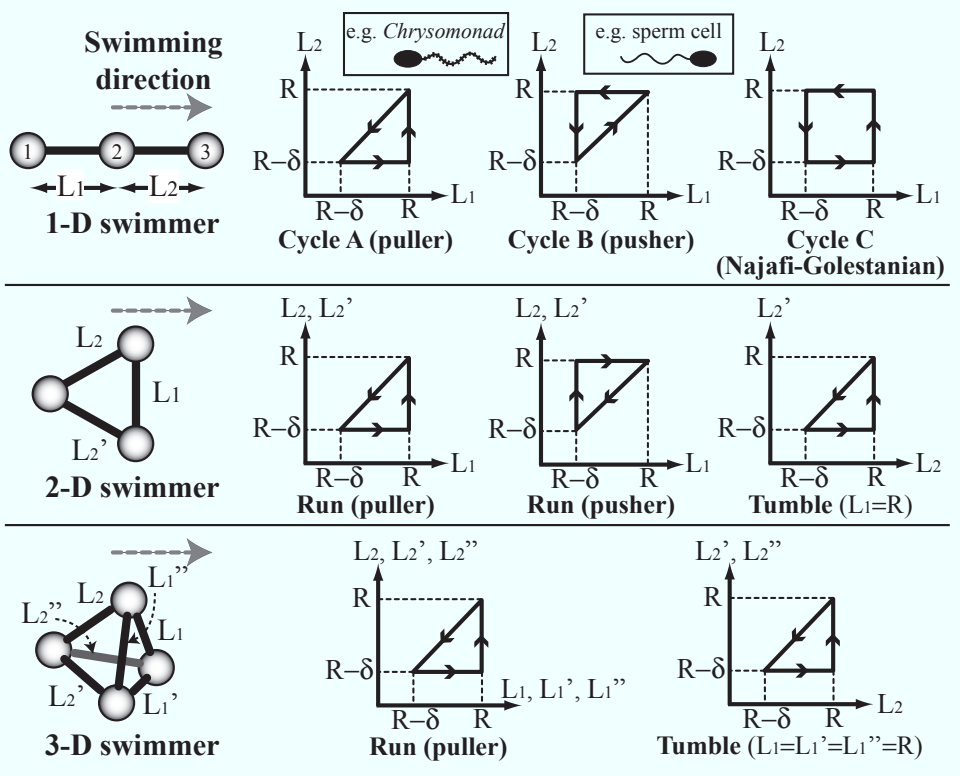

Figure 6.1: Minimal models of one-, two- and three-dimensional micro-swimmers and the cycle histories. *Chrysomonad* and sea urchin spermatozoon are examples of one-dimensional puller and pusher, respectively. Note that tumbling is induced in the 2D- and 3D-swimmers by holding the equilibrium lengths of one (2D) or three (3D) bond-lengths fixed while varying the lengths of the other bonds.

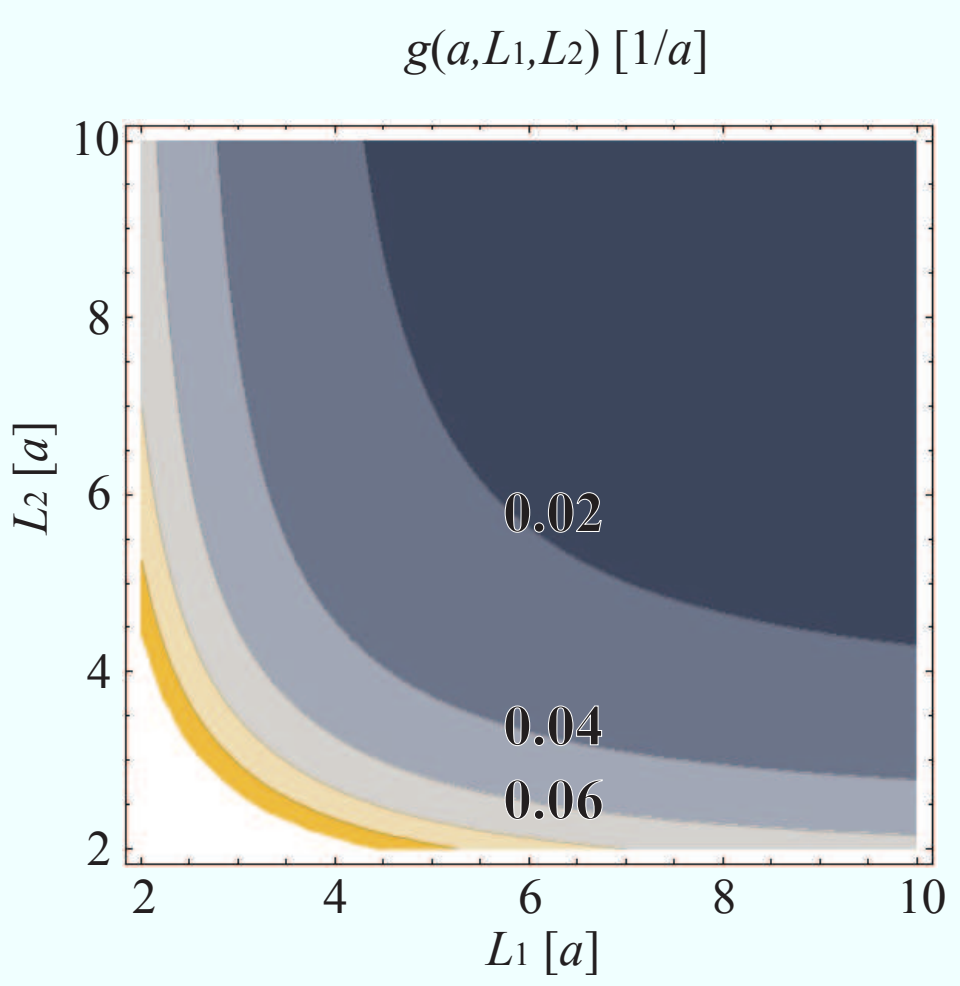

Figure 6.2: (color online). Contour plot of function $g(a, L_1, L_2)$ in Eq. 6.7.

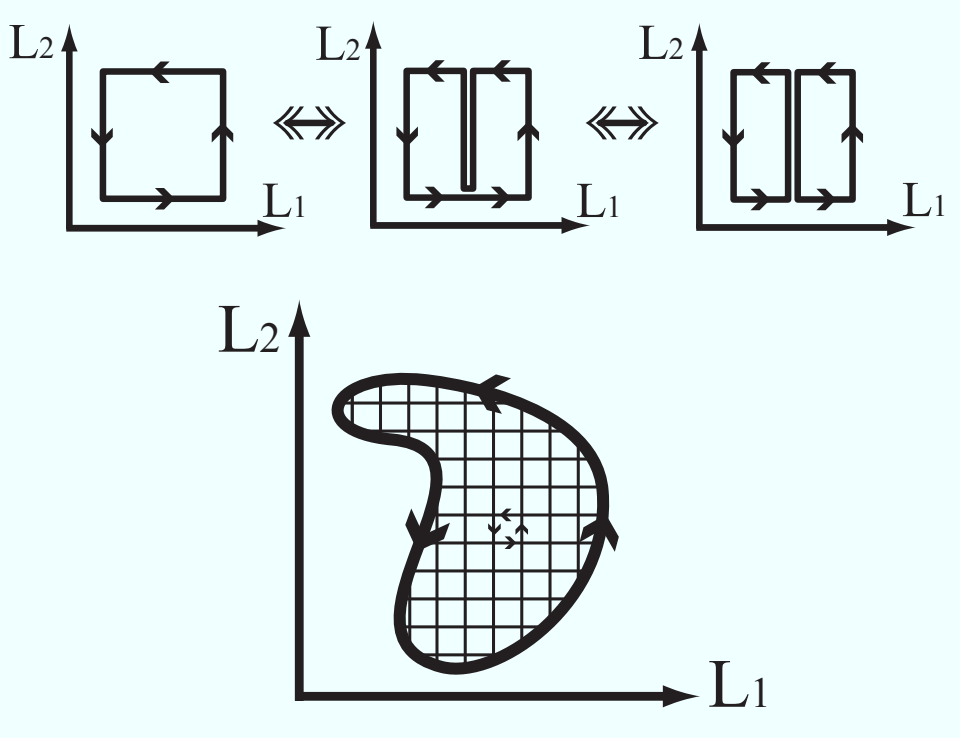

Figure 6.3: The top three figures illustrate that since in Stokes flow no net migration is produced by any bead motions that merely reverse themselves, the migration in any single cycle can be obtained as the sum of the migrations in two cycles into which the original cycle is divided. Extending this principle, the bottom figure illustrates that the migration in a cycle of arbitrary shape approaches that of the sum of migrations in small rectangular cycles into which the original cycle is divided.

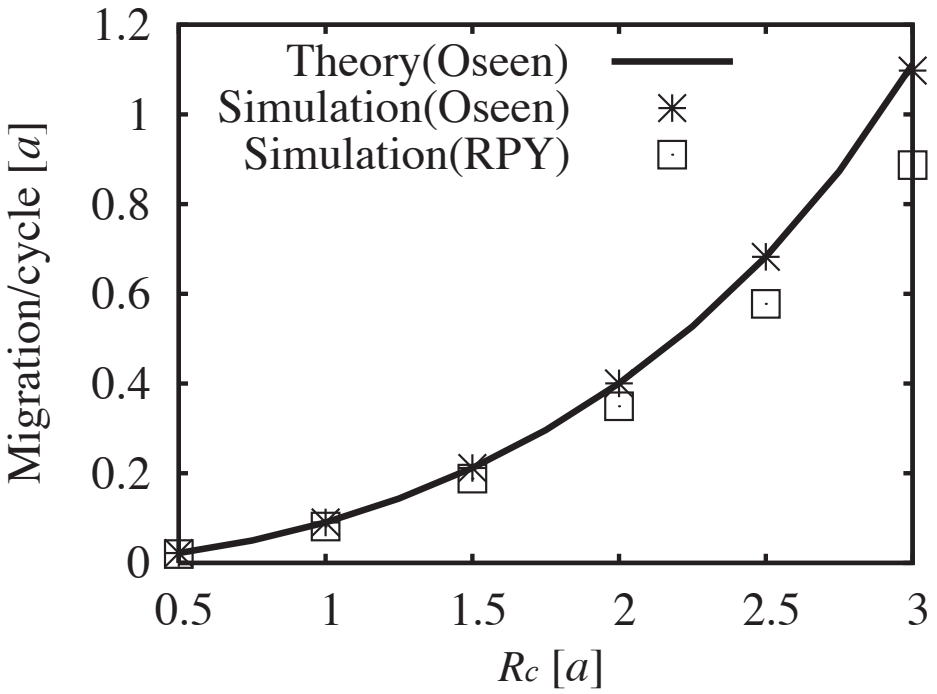

Figure 6.4: The migration per cycle for a CCW circular cycle centered at $(L_1, L_2) = (5a, 5a)$ with radius $0.5a < R_c < 3a$, obtained from Eq. 6.7 (Theory), simulations with the Oseen tensor and the RPY tensor.

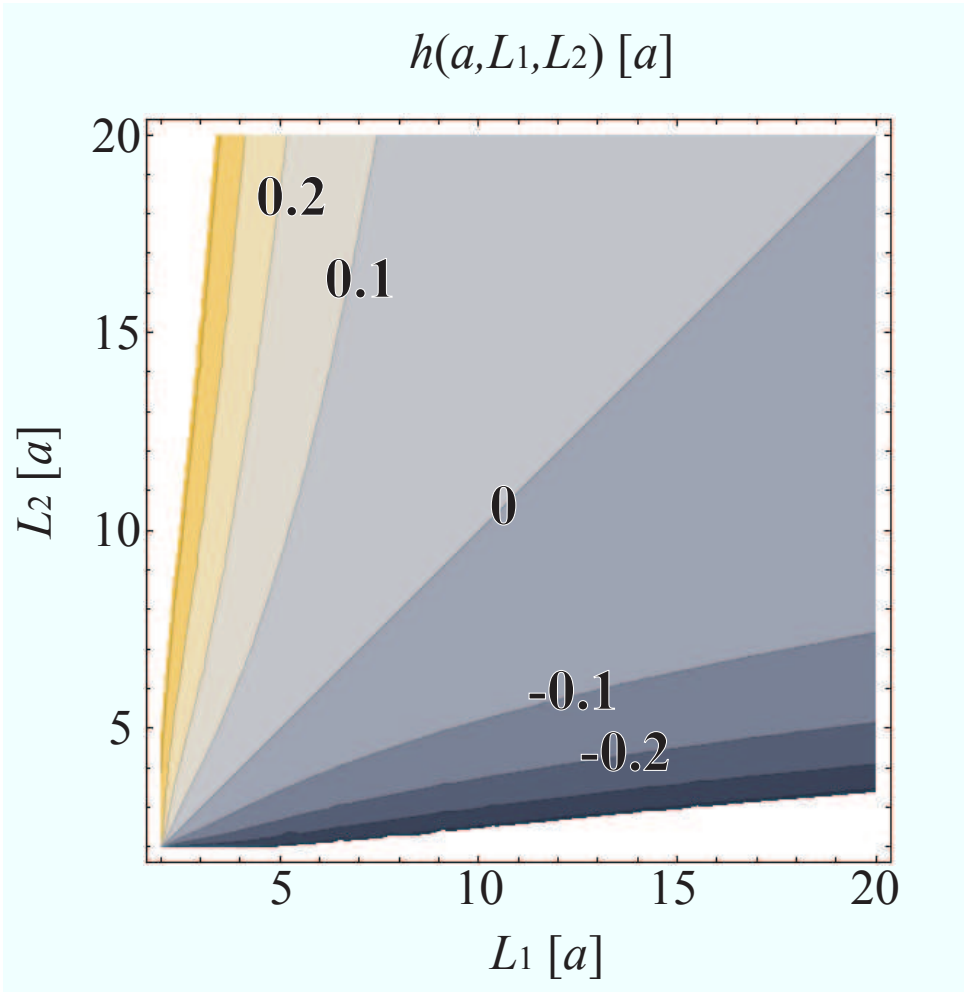

Figure 6.5: (color online). Contour plot of function $h(a, L_1, L_2)$ in Eq. 6.10.

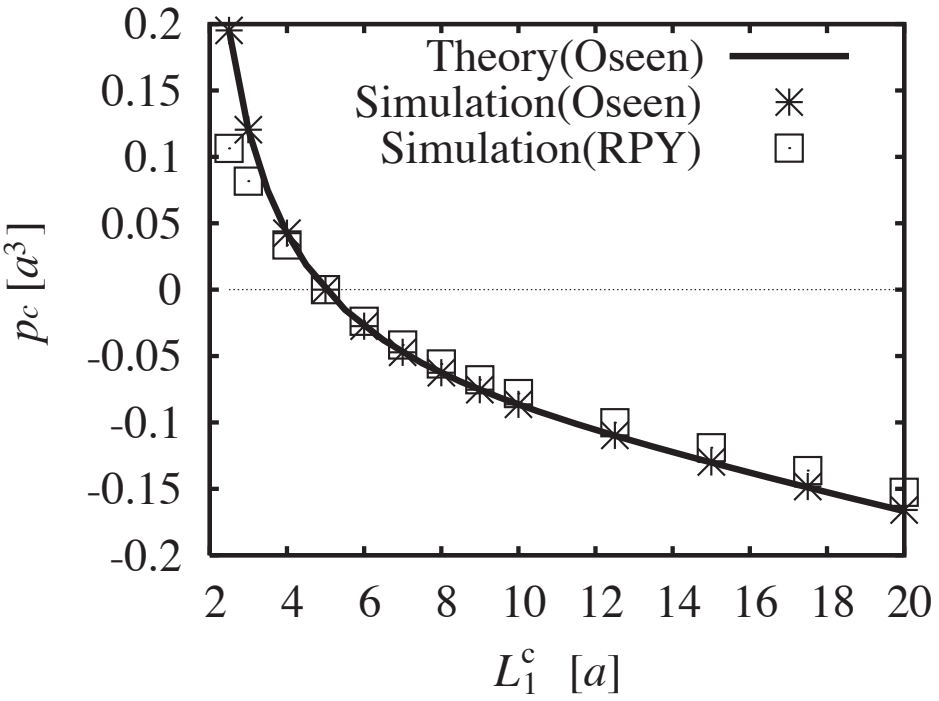

Figure 6.6: The strength of dipole flow, p_c, for a CCW circular cycle with radius $0.5a$ and centered at $(L_1, L_2) = (L_1^c, 5a)$ where $2a < L_1^c < 20a$, obtained from Eq. 6.7 (Theory), simulations with the Oseen tensor and the RPY tensor

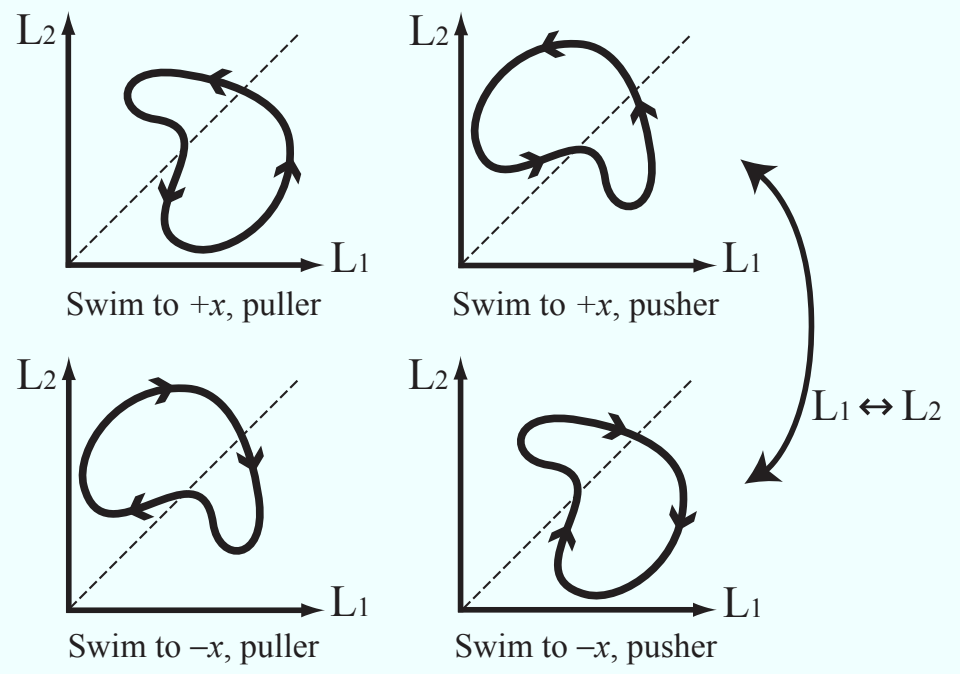

Figure 6.7: The change of the swimming behaviors by an inversion of the cycle-direction or an exchange of L_1 and L_2.

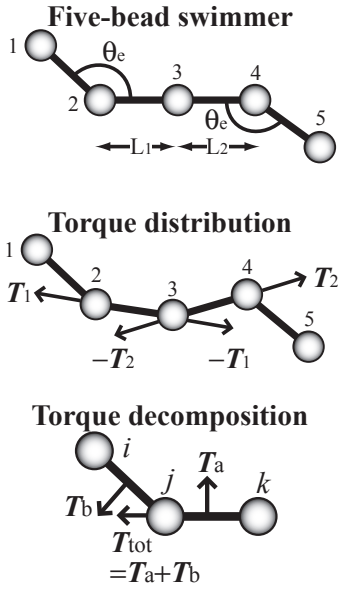

Figure 6.8: (Top) the configuration of the five-bead model. (Middle) the torque distribution on the swimmer. (Bottom) a decomposition of a torque $\boldsymbol{T}_{\rm tot}$ on three connected beads, which represents either $\boldsymbol{T}_1$, $\boldsymbol{T}_2$, $-\boldsymbol{T}_1$ or $-\boldsymbol{T}_2$ in the middle figure, into two torques $\boldsymbol{T}_a$ and $\boldsymbol{T}_b$ acting perpendicular to adjacent bonds.

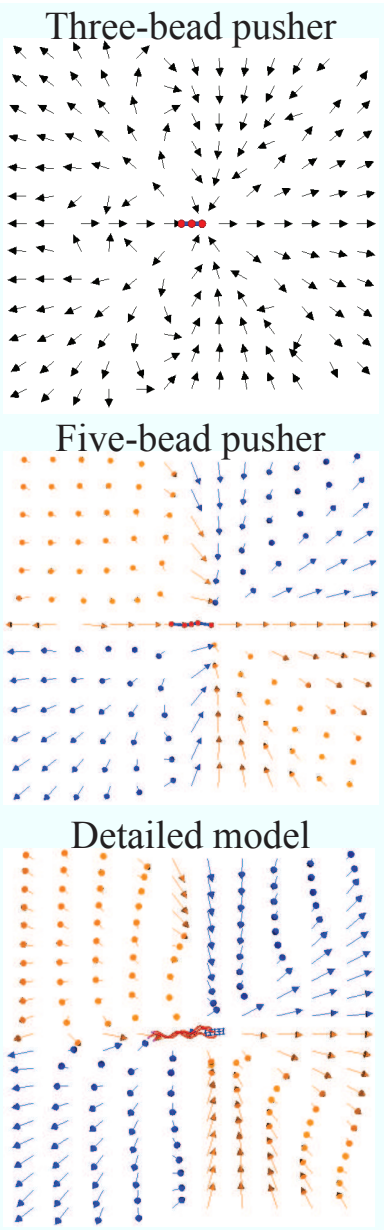

Figure 6.9: (color online). The time-averaged flow field around a three-bead pusher (top), around a five-bead pusher (middle) and around a detailed bead-spring model of *E. coli* in a run [1] (bottom). All arrows are unit flow-velocity vectors. Red (or light gray) arrows point into the paper, blue (or dark gray) arrows the opposite, and black arrows only have in-plane velocities. Swimming is from left to right.

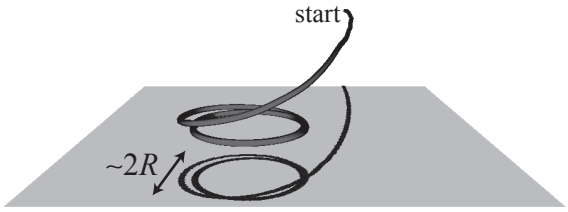

Figure 6.10: A trajectory of the five-bead swimmer near a wall. The trajectory is projected onto the wall to show the radius of the circular motion. The swimmer is initially placed $2R$ away from and parallel to the wall. Simulation parameters are a=0.2R, δ=0.5R, t_0=2.0τ, H=1000T/R, k_b=2000T, θ_e=160° and Δt=$10^{-3}\tau$.

CHAPTER VII

Shear-induced chiral migration of particles with anisotropic rigidity

7.1 Introduction

Microscopic biological objects, including cells, often have complex and anisotropic internal structures. The mechanical response of such an object to an external field will differ significantly from that of an object with uniform internal structure. Although the dynamics in flows of rigid particles with axisymmetric or chiral shape [68, 86, 93–95] and of flexible particles or droplets with isotropic mechanical properties [96–98] have been studied, there has been very little investigation of the effect of *anisotropic structure* or rigidity on the dynamics of a deformable particle in a flow. Here, we therefore develop a very simple model of an achiral particle with anisotropic rigidity and show by computer simulations that in a shear flow at vanishing Reynolds number it can deform into chiral shape and migrate in the vorticity direction.

7.2 Method

Fundamental studies of the dynamics of deformable objects, such as polymer molecules, have long been conducted using simple dumbbell, trumbbell and multi-spring models with minimal degrees of freedom [29, 99, 100]. A minimal model of a deformable object with three-dimensional anisotropic structure is a tetrahedron con-

taining four beads and six springs, which we call "tetrumbbell" (see Fig. 7.1). Each of the six springs is a "FENE-Fraenkel (FF) spring" [80] with the same equilibrium length L but different spring constant k, and its deformed spring length Q is restricted to a range set by the parameter s:

$$\boldsymbol{f}^{\mathrm{FF}} = k\,\frac{Q-L}{1-(1-Q/L)^2/s^2}\frac{\boldsymbol{Q}}{Q} \qquad \text{for } (1-s) < Q/L < (1+s), \tag{7.1}$$

The FF spring avoids overlaps of beads or springs, which would be unavoidable with Hookean springs under a strong external flow. Note that the shape of the tetrumbbell is achiral in equilibrium (i.e. it is a regular tetrahedron), since all beads have identical hydrodynamic radius and all springs have identical equilibrium length.

The shear-induced motion of a tetrumbbell is computed according to the following discretized differential equation for each bead:

$$\boldsymbol{r}_i(t+\Delta t) = \boldsymbol{r}_i(t) + \left\{ \boldsymbol{v}_{\mathrm{flow}}(\boldsymbol{r}_i) + \sum_{j=1}^{4} \mathcal{H}_{ij}\cdot\boldsymbol{f}_j \right\} \Delta t. \tag{7.2}$$

where $\boldsymbol{r}_i(t)$ is the position of bead i $(=1,2,3,4)$ at time t, $\boldsymbol{f}_i$ is the summation of the FF spring forces on bead i and the flow velocity field $\boldsymbol{v}_{\mathrm{flow}}$ is $\boldsymbol{v}_{\mathrm{flow}}(\boldsymbol{r}) = \dot{\gamma}_{xy} r_y \boldsymbol{e}_x$ with $\dot{\gamma}_{xy}$ and $\boldsymbol{e}_x$ being the shear rate and the unit vector in the x-direction, respectively. $\mathcal{H}_{ij}$ is the RPY hydrodynamic interaction tensor [29, 32, 33] given by:

$$\mathcal{H}_{ii} = \frac{1}{6\pi\eta a}\mathcal{I}, \tag{7.3}$$

$$\mathcal{H}_{ij} = \frac{1}{8\pi\eta r_{ij}}\left[\left(1+\frac{2a^2}{3r_{ij}^2}\right)\mathcal{I} + \left(1-\frac{2a^2}{r_{ij}^2}\right)\frac{\boldsymbol{r}_{ij}\boldsymbol{r}_{ij}}{r_{ij}^2}\right] \text{ if } i\neq j \text{ and } r_{ij}\geq 2a, \tag{7.4}$$

$$\mathcal{H}_{ij} = \frac{1}{6\pi\eta a}\left[\left(1-\frac{9r_{ij}}{32a}\right)\mathcal{I} + \frac{3}{32}\frac{\boldsymbol{r}_{ij}\boldsymbol{r}_{ij}}{a r_{ij}}\right] \text{ if } i\neq j \text{ and } r_{ij}< 2a, \tag{7.5}$$

Here, $\boldsymbol{r}_{ij} = \boldsymbol{r}_i - \boldsymbol{r}_j$, $\mathcal{I}$ is the 3×3 identity matrix, and a is the bead radius. Using this model, we compute the response of a tetrumbbell to shear taking into account

its hydrodynamic interactions through solvent motion. Brownian motion and inertia are both neglected in this study. Nevertheless, the dynamics of the tetrumbbell is not time-reversible due to two sources of non-linearity, namely, the non-linearity of the FF spring force and the non-linearity that arises from the finite relaxation time of the deformation of the tetrumbbell.

The model has three input parameters with physical units: a (bead radius), η (solvent viscosity), and k (typical FF spring constant). Therefore, we scale length and time by a and $\tau = a\eta/k$, respectively. The dimensionless shear rate and the migration velocity in the vorticity direction are given by $\Pi_{\rm s} = \dot{\gamma}_{xy}\eta a/k$ and $\Pi_{\rm vz} = V_z^{\rm cm}\eta/k$, where $V_z^{\rm cm}$ is the center-of-mass velocity of the tetrumbbell in the vorticity direction.

The spring parameters (k_n, s_n), where n is spring index ($n = 1, 2 \cdots 6$), are chosen to be either "hard" $(k_{\rm hard}, s_{\rm hard}) = (1000k, 0.001)$ or "soft" $(k_{\rm soft}, s_{\rm soft}) = (k, 0.5)$ for simplicity, and the equilibrium length of the FF springs is set to $L = 5a$. Within theses specifications, ten distinguishable structures of tetrumbbells can be constructed, which are shown in Fig 7.1. Note that the structures (3c) and (3c') in Fig. 7.1 have hard backbones that possess chirality through three hard springs, but the others lack chirality in either particle or backbone shape, in the absence of flow. We computed the motion of tetrumbbells with structure (1a), (2a) $\cdots$ (5a) in a shear flow of strength $0.002 \leq |\Pi_s| \leq 0.2$ with time step Δt=10^{-3}, with various initial orientations of the tetrumbbell relative to the shear direction.

7.3 Results

We find that all tetrumbbells except for (3b), (4a) and (5a) migrate in the vorticity direction in shear flow. Five types of migration are observed:

- Type M: the tetrumbbell migrates in the vorticity direction and the direction of the migration (i.e. the $+z$ or $-z$ direction) depends on the initial orientation

of the tetrumbbell.

- Type A: the tetrumbbell migrates in the vorticity direction in shear flow only above a threshold shear rate, which is dependent on the initial orientation of the tetrumbbell, and the direction of the migration also depends on the initial orientation.

- Type C: the tetrumbbell migrates in the vorticity direction and the direction of the migration does not depend on the initial orientation of the tetrumbbell.

- Type N: the tetrumbbell does not migrate in the vorticity direction in shear flow.

- Type M/N: the tetrumbbell shows migration of either type M or N depending on the initial orientation of the tetrumbbell.

Table 7.1 shows the migration type for each tetrumbbell structure, and a typical migration history is shown in Figs. 7.2 and 7.3 in terms of the center-of-mass position, velocity and conformation. In a steady shear flow, tetrumbbells of migration type M, C and A deform and change their conformation and migration velocity periodically, with each cycle producing a net migration in the vorticity direction. The tetrumbbell does not migrate when the hydrodynamic interaction is turned off (i.e. $\mathcal{H}_{ij} = 0$ for $i \neq j$). It is also worth noting that the unit vector pointing from the center-of-mass to a specific bead of the tetrumbbell follows a closed orbit at steady state, analogous to the Jeffery orbit of a axisymmetric particle in shear flow [86]. Since a particle with achiral shape does not migrate in shear flow in the vorticity direction because of the reflection symmetry of hydrodynamics in shear flow [93], the migration of tetrumbbell can be attributed to the chiral deformation induced by the shear flow. To quantify

the chirality of a tetrumbbell in motion, we introduce a chiral deflection index χ,

$$\chi = \sqrt[3]{G_0}, \tag{7.6}$$

$$G_0 = \frac{1}{3}\left[\sum_{i,j,k,l=1\cdots4} \frac{[(\boldsymbol{r}_{ij}\times\boldsymbol{r}_{kl})\cdot\boldsymbol{r}_{il}]\,(\boldsymbol{r}_{ij}\cdot\boldsymbol{r}_{jk})(\boldsymbol{r}_{jk}\cdot\boldsymbol{r}_{kl})}{(r_{ij}r_{jk}r_{kl})^2\ r_{il}}\right]. \tag{7.7}$$

Here, G_0 is a chirality index proposed in Ref. [101] for molecules, and χ is the cube root of G_0, making it proportional to the shear rate $\dot{\gamma}_{xy}$ at low shear rate for tetrumbbells. The chiral deflection index differs from zero if the tetrumbbell deforms into a chiral geometry, and is invariant under rotation, translation and dilation, but changes sign on reflection. As shown in Fig. 7.3, the tetrumbbell has chiral shape in shear flow, and the instantaneous chirality induces migration in the vorticity direction.

To evaluate the migration velocity of tetrumbbells of migration types M, A and C at steady state, the center-of-mass velocity in the vorticity direction was averaged over time for one cycle of deformation process (T_{cycle}),

$$|\Pi_{\text{vz}}^{\text{ave}}| = \left|\frac{1}{T_{\text{cycle}}}\int_{t}^{t+T_{\text{cycle}}} \Pi_{\text{vz}}(t')dt'\right|, \tag{7.8}$$

and plotted in Fig. 7.4. From dimensional analysis, we expect

$$|\Pi_{\text{vz}}^{\text{ave}}| = func(\Pi_{\text{s}}, s_{\text{soft}}, s_{\text{hard}}, k_{\text{hard}}/k_{\text{soft}}, L/a). \tag{7.9}$$

Since we hold s_{soft}, s_{hard}, $k_{\text{hard}}/k_{\text{soft}}$ and L/a constant through our simulations, this simplifies to $|\Pi_{\text{vz}}^{\text{ave}}| = func(\Pi_{\text{s}})$. When the shear rate is small enough that the nonlinearity of the spring force and the effect of relaxation time of tetrumbbell deformation are not significant, the relation between $|\Pi_{\text{vz}}^{\text{ave}}|$ and Π_{s} follows a quadratic

power-law:

$$|\Pi_{\rm vz}^{\rm ave}| = C_{\rm str}\ {\Pi_{\rm s}}^2, \qquad \text{or} \tag{7.10}$$

$$|V_{\rm z}^{\rm cm,ave}| = C_{\rm str}(\eta a^2/k)\dot{\gamma}_{xy}^2, \tag{7.11}$$

where $C_{\rm str}$ is a positive constant unique to each structure of tetrumbbell, and $V_{\rm z}^{\rm cm,ave}$ is the time-averaged center-of-mass velocity in the vorticity direction.

In the regime $|\Pi_{\rm s}| < 0.02$ where the quadratic power-law holds, the stretch of the soft spring $Q_{\rm soft}$ is $0.85L \lesssim Q_{\rm soft} \lesssim 1.15L$, and the Weissenberg number Wi is less than 0.3, where $Wi = \dot{\gamma}_{xy}\tau_{\rm relax}$ with $\tau_{\rm relax}$ being the relaxation time of the tetrumbbell deformation [1]. Since the non-linear effects in this regime of shear rate are small, the magnitude of the chiral deflection of the tetrumbbell is proportional to the shear rate. In general, the migration velocity of a rigid chiral object $V_z^{\rm rigid}$ is a product of the shear rate $\dot{\gamma}_{xy}$ and a constant g that is determined by the shape of the object [93],

$$V_z^{\rm rigid} = g\dot{\gamma}_{xy}. \tag{7.12}$$

Therefore, the quadratic power law for the tetrumbbell results from the proportionality between the perturbation of g and the shear rate $\dot{\gamma}_{xy}$.

In the high shear rate regime ($|\Pi_{\rm s}| \gtrsim 0.02$), the quadratic power law no longer holds because the magnitude of the chiral deflection is non-linear in the shear rate, and the time-delayed motion caused by a finite Wi becomes non-negligible. Also, the migrations type A of structures (1a) and (2a) are triggered by a non-linear effect because the migration of type A can not be observed at all in the low shear rate regime.

[1] The relaxation time of the tetrumbbell deformation was computed from a history of the chiral deflection index of a tetrumbbell under no flow with its initial configuration having a non-zero chiral deflection index.The history was fitted by the following equation to obtain the longest relaxation time: $\chi(t) = \chi(0)\exp(-t/\tau_{\rm relax})$ when $\chi(t)/\chi(0) \leq 0.7$.

The quadratic power law, however, does not tell us the direction of migration of a tetrumbbell. Although the magnitude of the migration velocity only depends on the shear rate, the direction of migration depends on the initial orientation of the tetrumbbell except for (3c) and (3c'), which have intrinsic chirality in their backbone and always migrate in a direction that is determined by this backbone chirality. Note that the backbone chirality, by itself, does not lead to migration, since at rest the bead positions, which produce the hydrodynamic effects, are achiral. The chiral backbone does, however, determine the shear deformation of the tetrumbbell, including its shear-induced chirality.

Also, surprisingly, a switch of the shear direction from $\Pi_s = \Pi_{s0}$ to $-\Pi_{s0}$ does not necessarily change the direction of migration. Although the tetrumbbells of migration types A and C do change migration direction (i.e. from $+z$ to $-z$ direction or vice versa) upon reversal of the shear direction, the tetrumbbells of migration type M do not (see Fig. 7.2). This is because the tetrumbbells of migration type M change sign of the chiral deflection index upon reversal of the shear direction, but those of migration type A and C do not, as we confirmed by plotting the chiral deflection index (see Fig. 7.3 for type M). For a rigid chiral particle, which has an intrinsic chirality, the migration direction must change when the shear direction is reversed according to Eq. (7.12). The response of a tetrumbbell of migration type M to reversal of the shear direction is possible because the chirality is not intrinsic but shear-induced.

7.4 Summary

Our simulation results for simple tetrumbbells show the possibility that an achiral deformable object with anisotropic rigidity can migrate in the vorticity direction in a shear flow due to shear-induced chirality. By setting the simulation parameters to be a=20[μm], η=100[cP] and k=1[mN/m], we find a migration velocity of 3[μm/sec] at a shear rate of 10[sec^{-1}] using the result of our simulation $(|\Pi_{vz}^{ave}|, \Pi_s) = (3 \times 10^{-4}, 0.02)$

in Fig. 7.4. In practice, migration due to the shear-induced chirality might be observed for a multiphasic particle [102, 103], which has two or more distinct compartments of different elastic moduli. Another example will be an oil droplet in water under shear, if the droplet encases a solid object of comparable dimension to the droplet (see Fig. 7.5). An oil droplet enclosing a solid object could act as a particle with anisotropic rigidity. Depending on the shape of the solid object, the complex might migrate in the vorticity direction in a shear flow. Such a phenomenon might be used to separate small objects with polydispersity in size or shape.

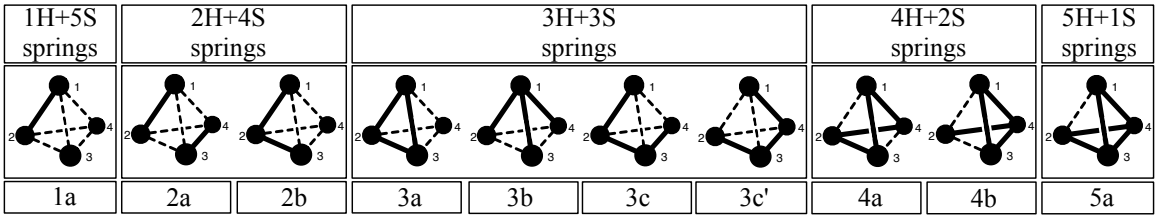

Figure 7.1: The ten distinguishable tetrumbbell structures constructed from four beads and six springs, each of which is either a hard (H, solid line) or soft (S, dotted line) spring.

Structure of tetrumbbell	1a	2a	2b	3a	3b	3c	3c'	4a	4b	5a
Migration type	A	A	M/N	M	N	C	C	N	M	N

Table 7.1: Types of shear migration of different tetrumbbell structures.

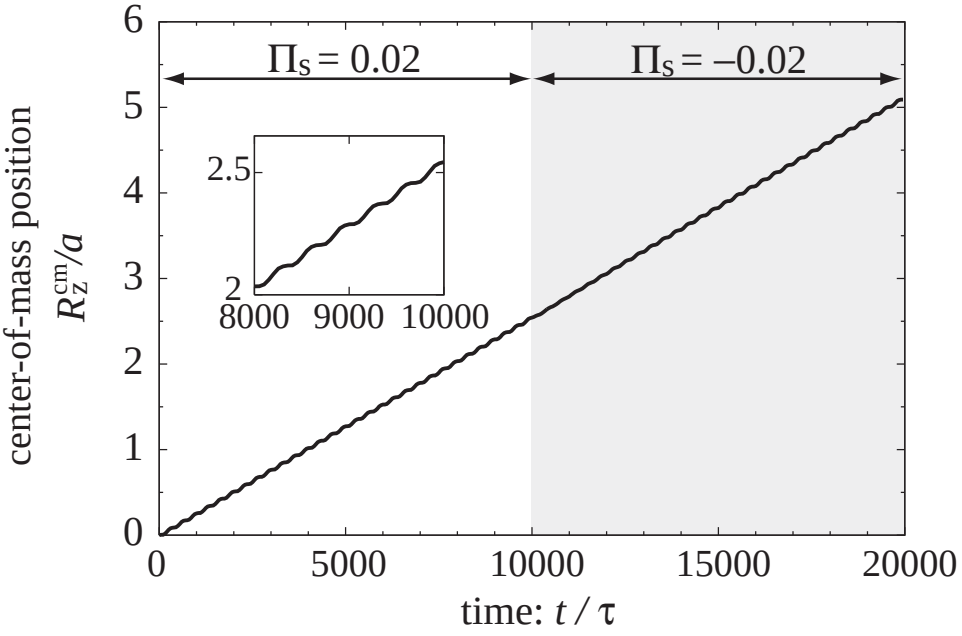

Figure 7.2: History of the center-of-mass position of tetrumbbell (2b) of migration type M in the vorticity direction (R_z^{cm}). The shear rate is changed from $\Pi_s = 0.02$ to $\Pi_s = -0.02$ at time $t/\tau = 10000$.

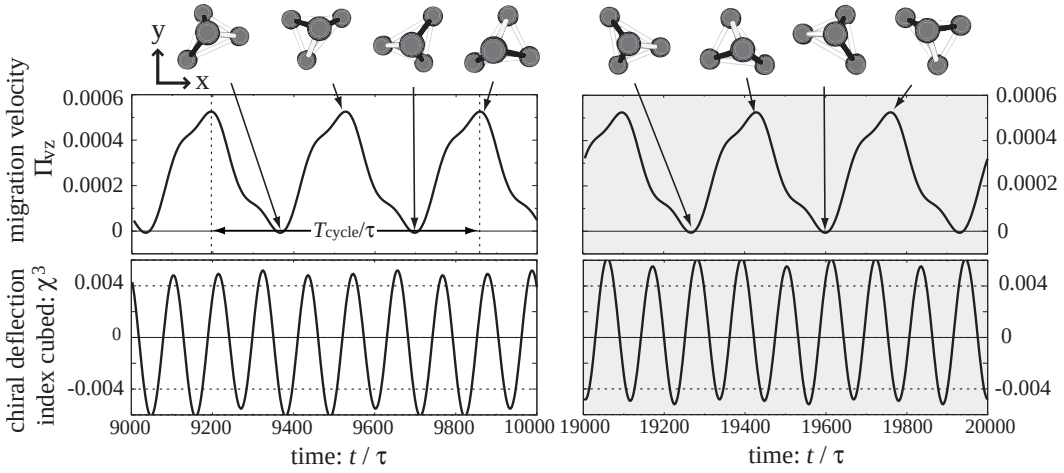

Figure 7.3: History of the conformation change, the migration velocity in the vorticity direction, and the chiral deflection index of tetrumbbell (2b) of migration type M, which corresponds to the migration history in Fig. 7.2. The shear rate is $\Pi_s = 0.02$ for the plots on the left side and $\Pi_s = -0.02$ for those on the right side. The black and white bonds in the figures of the tetrumbbell conformation show the hard and soft springs, respectively. Note that the history of chiral deflection index changes sign upon reversal of the shear direction. In this case, $T_{\rm cycle}/\tau \simeq 670$.

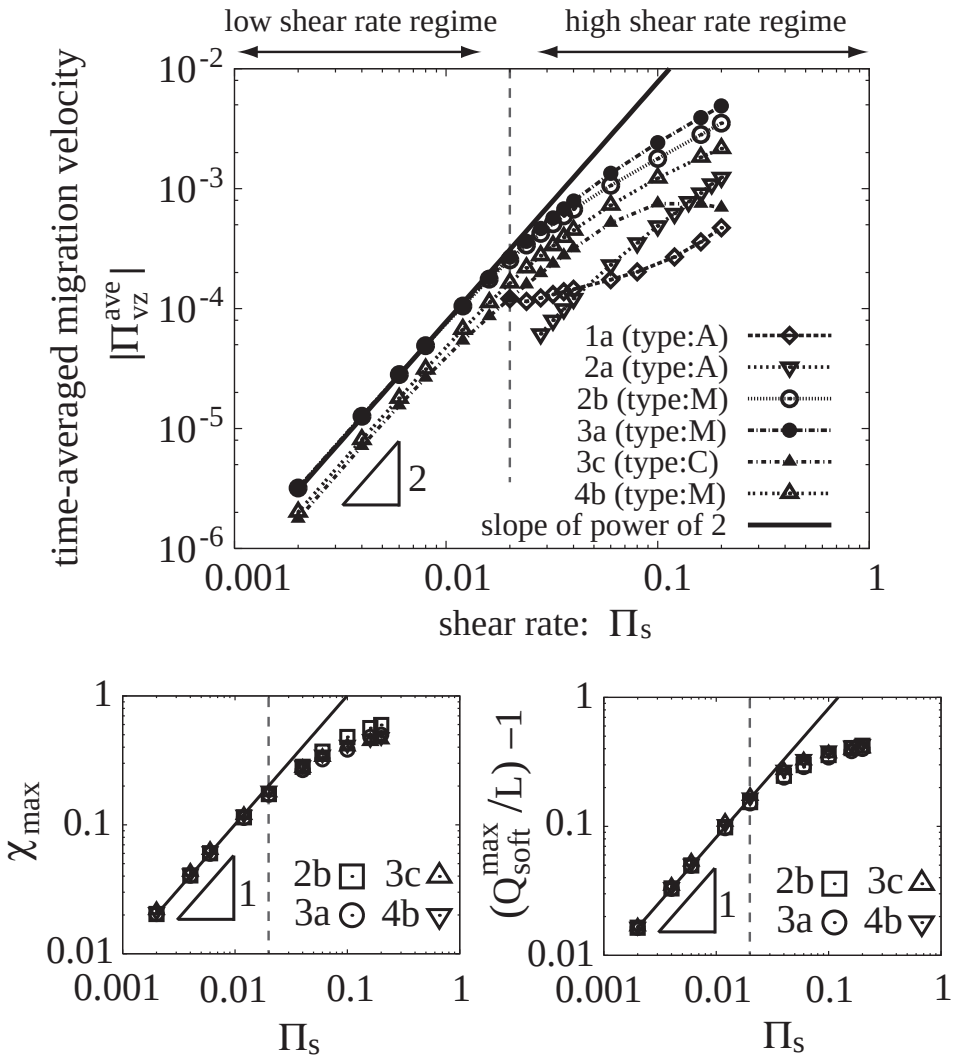

Figure 7.4: (top) The time-averaged migration velocity $|\Pi_{vz}^{ave}|$ as a function of shear rate Π_s for each type of tetrumbbell. (bottom left) The maximum of the chiral deflection index (χ_{max}) in one cycle of deformation as a function of the shear rate. The solid line has the slope of power of 1. (bottom right) The maximum stretch ratio of soft spring $(Q_{soft}^{max} - L)/L$ in one cycle of deformation as a function of the shear rate.

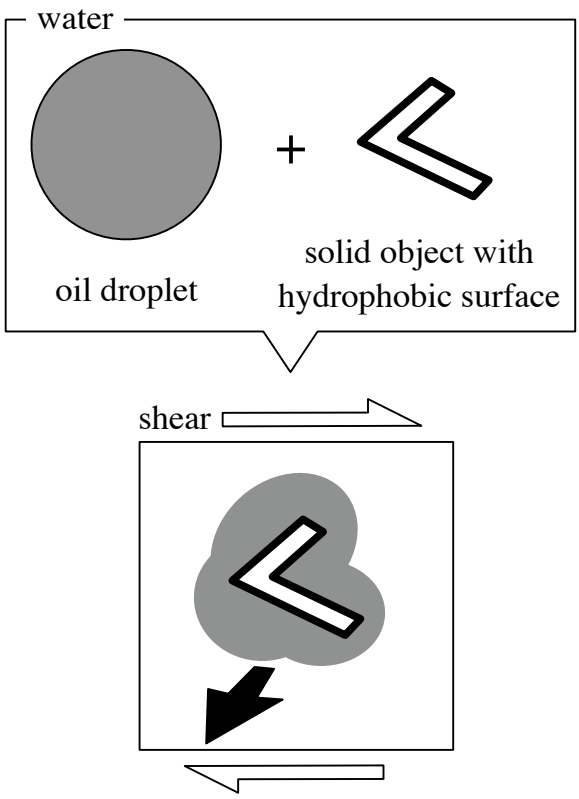

Figure 7.5: Sketch of possible migration of a droplet enclosing a solid object in shear flow.

CHAPTER VIII

Summary and Future Work

In this study, the bead-spring model with hydrodynamic interactions (HIs) was used to simulate the dynamics of a deformable object in fluid. It was found that bead-spring modeling for a deformable object is so versatile that various types of objects can be modeled and simulated, such as bacteria, bio-polymers, and modeled droplets. We employed two different methods depending on the boundary condition of the problem to account for HI, i.e. using 1) HI tensor or 2) Stochastic Rotation Dynamics (SRD). Using the HI tensor, the flow perturbation is accurate up to $1/r^3$, where r is the distance from a bead, at zero Reynolds number, and the computation is quite simple since the flow perturbation at a position is simply the superposition of the perturbations from all beads. Therefore, the bead-spring model with HI tensor is a powerful method for prediction of the dynamics of a deformable object in a flow without any boundary wall, or with just a planer wall. However, there are some difficulties to extend this method to address problems such as the dynamics under the presence of complex boundary and the collective dynamics of deformable objects. Since there is no simple analytical expression of HI tensor that accounts for the presence of more than one wall, it requires some simplification or additional assumption to simulate, for example, the dynamics of a DNA molecule in a micro-channel with two parallel planer wall. A possible assumption for this case may be to take into

account the presence of only one wall closer to the DNA molecule and the neglect the other. This assumption becomes effective only when the two walls are far enough that the effect of walls is negligible at the center of the channel.

To study the multi-body interactions of deformable objects using HI tensor, it should be noted that the computational cost increases as N^2 where N is the number of beads. To avoid this rapid increase in the computational cost, it might be effective to apply a periodic boundary condition. A HI tensor accounting for the effect of periodic images has been proposed in Ref. [104], although we have not implemented this for our study so far. Employing this "periodic HI tensor" will enable us to study the collective dynamics of deformable objects in a dilute or even a concentrated system with efficient computation.

On the other hand, using SRD, a periodic boundary condition and a complex boundary condition can be easily introduced (see Chapter II). Therefore, SRD can be a powerful method for studying collective dynamics of deformable objects with or without a complex boundary. However, SRD has some limitations when used for the simulation of deformable objects. First, since SRD intrinsically includes Brownian motion, a long time-averaging might be needed to average out Brownian fluctuations and obtain reliable results, such as flow field induced by an deformable object. Interestingly, the automatic inclusion of HI in the SRD method can also be an advantage over other simulation methods for hydrodynamics that require some additional work to include the Brownian motion to study its effect. A second drawback of SRD it that, since it is a particle-based simulation method and the viscosity of the fluid is associated with the density of the SRD particles, the viscosity, or the Reynolds number, cannot be controlled independently from the SRD particle density. This can limit the range of the Reynolds numbers one can explore with SRD. For example, the regime where the Reynolds number close to zero may cost more computational time since for this case a high density of SRD particles is needed.

As mentioned in Chapter V, bead-spring modeling for a thin helical filament becomes more accurate when more beads with smaller hydrodynamic radius are used, which costs more computational time. This increase of the computational cost for modeling thin objects may be avoided by introducing rod-like elements [105] instead of beads. Moreover, the use of rod-like elements may allow us to obtain a model with more accurate mobility coefficient with less number of elements compared with beads, especially for thin object. This possibility should be pursued for a future work.

BIBLIOGRAPHY

BIBLIOGRAPHY

[1] N. Watari and R. G. Larson. The hydrodynamics of a run-and-tumble bacterium propelled by polymorphic helical flagella. *Biophysical Journal*, 98:12–17, 2010.

[2] R. M. Jendrejack, D. C. Schwartz, J. J. de Pablo, and M. D. Graham. Shear-induced migration in flowing polymer solutions: Simulation of long-chain DNA in microchannels. *Journal of Chemical Physics*, 120:2513, 2004.

[3] J. P. Hernandez-Ortiz, C. G. Stoltz, and M. D. Graham. Transport and collective dynamics in suspensions of confined swimming particles. *Physical Review Letters*, 95:204501, 2005.

[4] Ingmar H. Riedel, Karsten Kruse, and Jonathon Howard. A self-organized vortex array of hydrodynamically entrained sperm cells. *Science*, 309:300–303, 2005.

[5] J. R. Blake. A note on the image system for a stokeslet in a no-slip boundary. *Mathematical Proceedings of the Cambridge Philosophical Society*, 70:303–310, 1971.

[6] J. T. Padding and A. A. Louis. Hydrodynamic interactions and brownian forced in colloidal suspensions: Coarse-graining over time and length scales. *Physical Review E*, 74:031402, 2006.

[7] N. Kikuchi. *A mesoscale model for polymer hydrodynamics*. PhD thesis, University of Oxford, 2003.

[8] H. Noguchi and G. Gompper. Dynamics of fluid vesicles in shear flow: Effect of membrane viscosity and thermal fluctuations. *Physical Review E*, 72:011901, 2005.

[9] J. Hirabayashi, N. Ito, K. Noguchi, and K. Kasai. Slalom chromatography: Size-dependent separation of DNA molecules by a hydrodynamic pheonomenon. *Biochemistry*, 29:9515, 1990.

[10] G. Stegeman, J. C. Kraak, and H. Poppe. Hydrodynamic chromatography of polymers in packed columns. *Journal of Chromatography A*, 657:283, 1993.

[11] J. Han and H. G. Craighead. Separation of long DNA molecules in a microfabricated entropic trap array. *Science*, 288:1026, 2000.

[12] L. Fang, H. Hu, and R. G. Larson. DNA configurations and concentration in shearing flow near a glass surface in a microchannel. *Journal of Rheology*, 49:127, 2005.

[13] B. H. Zimm. Dynamics of polymer molecules in dilute solution: Viscoelasticity, flow birefringence and dielectric loss. *Journal of Chemical Physics*, 24:269, 1956.

[14] M. Doi and S. F. Edwards. *The Theory of Polymer dynamics*. Oxford University Press, 1986.

[15] D. L. Ermak and J. A. McCammon. Brownian dynamics with hydrodynamic interactions. *Journal of Chemical Physics*, 69:1352, 1978.

[16] A. Malevanets and R. Kapral. Mesoscopic model for solvent dynamics. *Journal of Chemical Physics*, 110:8605, 1999.

[17] T. Ihle and D. M. Kroll. Stochastic rotation dynamics: A galilean-invariant mesoscopic model for fluid flow. *Physical Review E*, 63:020201, 2001.

[18] N. Kikuchi, C. M. Pooley, J. F. Ryder, and J. M. Yeomans. Transport coefficients of a mesoscopic fluid dynamics model. *Journal of Chemical Physics*, 119:6388, 2003.

[19] M. Ripoll, K. Mussawisade, R. G. Winkler, and G. Gompper. Dynamic regimes of fluids simulated by multiparticle-collision dynamics. *Physical Review E*, 72:016701, 2005.

[20] K. Mussawisade, M. Ripoll, R. G. Winkler, and G. Gompper. Dynamics of polymers in a particle-based mesoscopic solvent. *Journal of Chemical Physics*, 123:144905, 2005.

[21] R. G. Larson, T. T. Perkins, D. E. Smith, and S. Chu. Hydrodynamics of a DNA molecule in a flow field. *Physical Review E*, 55:1794, 1997.

[22] J. F. Marko and E. D. Siggia. Stretching DNA. *Macromolecules*, 28:8759, 1995.

[23] A. Lamura and G. Gompper. Numerical study of the flow around a cylinder using multi-particle collision dynamics. *European Physical Journal E*, 9:477, 2002.

[24] T. T. Perkins, D. E. Smith, and S. Chu. Single polymer dynamics in an elongational flow. *Science*, 276:2016, 1997.

[25] C. M. Schroeder, H. P. Babcock, E. S. G. Shaqfeh, and S. Chu. Observation of polymer conformation hysteresis in extensional flow. *Science*, 301:1515, 2003.

[26] V. A. Beck and E. S. G. Shaqfeh. Ergodicity breaking and conformational hysteresis in the dynamics of a polymer tethered at a surface stagnation point. *Journal of Chemical Physics*, 124:094902, 2006.

[27] J. Kreft, Y. L. Chen, and H. C. Chang. Conformation and trapping rate of DNA at a converget stagnation point. *Physical Review E*, 77:030801(R), 2008.

[28] G. I. Taylor. On the decay of vortices in a viscous fluid. *Philosophical Magazine*, 46:671, 1923.

[29] R.M. Jendrejack, J. J. de Pablo, and M. D. Graham. Stochastic simulations of DNA in flow: Dynamics and the effects of hydrodynamic interactions. *Journal of Chemical Physics*, 116:7752, 2002.

[30] K. A. Dill and B. H. Zimm. A rheological separator for very large DNA molecules. *Nucleic Acids Research*, 7(3):735, 1979.

[31] R. G. Larson. Flow-induced mixing, demixing, and phase transitions in polymeric fluids. *Rheologica Acta*, 31(6):497, 1992.

[32] J. Rotne and S. Prager. Variational treatment of hydrodynamic interaction in polymers. *Journal of Chemical Physics*, 50:4831–4837, 1969.

[33] H. Yamakawa. Transport properties of polymer chains in dilute solution: Hydrodynamic interaction. *Journal of Chemical Physics*, 53:436–443, 1970.

[34] A. Ajdari. Electro-osmosis on inhomogeneously charged surfaces. *Physical Review Letters*, 75(4):755, 1995.

[35] A. S. Panwar and S. Kumar. Brownian dynamics simulations of polymer stretching and transport in a complex electroosmotic flow. *Journal of Chemical Physics*, 118(2):925, 2003.

[36] A. D. Strook, S. K. W. Dertinger, A. Ajdari, I. Mezic, H. A. Stone, and G. M. Whitesides. Chaotic mixer for microchannels. *Science*, 295:647, 2002.

[37] C. Hsieh, L. Li, and R. G. Larson. Modeling hydrodynamic interaction in brownian dynamics: simulations of extensional flows of dilute solutions of DNA and polystyrene. *Journal of Non-Newtonian Fluid Mechanics*, 113:147, 2003.

[38] J. M. Deutsch. Theoretical studies of DNA during gel electrophoresis. *Science*, 240:922–924, 1988.

[39] G. C. Randall and P. S. Doyle. Electrophoretic collision of a DNA molecule with an insulating post. *Physical Review Letters*, 93:058102, 2004.

[40] Y. J. Juang, S. Wang, X. Hu, and L. J. Lee. Dynamics of single polymers in a stagnation flow induced by electrokinetics. *Physical Review Letters*, 93:268105, 2004.

[41] J. Gehl. Electroporation: theory and methods, perspectives for drug delivery, gene therapy and research. *Acta Physiologica Scandinavica*, 177:437–447, 2003.

[42] W. D. Volkmuth and R. H. Austin. DNA electrophoresis in microlithographic arrays. *Nature*, 358:600–602, 1992.

[43] J. Han and H. G. Craighead. Separation of long DNA molecules in a microfabricated entropic trap array. *Science*, 288:1026–1029, 2000.

[44] J. S. Bader, R. W. Hammond, S. A. Henck, M. W. Deem, G. A. McDermott, J. M. Bustillo, J. W. Simpson, G. T. Mulhern, and J. M. Rothberg. DNA transport by a micromachined brownian ratchet device. *Proceedings of the National Academy of Sciences of the United States of America*, 96:13165–13169, 1999.

[45] J. L. Viovy. Electrophoresis of DNA and other polyelectrolytes: Physical mechanisms. *Reviews of Modern Physics*, 72:813–872, 2000.

[46] D. Long and A. Ajdari. A note on the screening of hydrodynamic interactions, in electrophoresis, and in porous media. *European Physical Journal E*, 4:29–32, 2001.

[47] O. B. Usta, J. E. Butler, and A. J. C. Ladd. Transverse migration of a confined polymer driven by an external force. *Physical Review Letters*, 98:098301, 2007.

[48] J. J. Zheng and E. S. Yeung. Anomalous radial migration of single DNA molecules in capillary electrophoresis. *Analytical Chemistry*, 74:4536–4547, 2002.

[49] J. J. Zheng and E. S. Yeung. Mechanism for the separation of large molecules based on radial migration in capillary electrophoresis. *Analytical Chemistry*, 75:3675–3680, 2003.

[50] J. P. Landers. *Handbook of capillary electrophoresis*. CRC Press, Boca Raton, 1997.

[51] T. Takagi. Electrophoretic light scattering. *Electrophoresis*, 14:1255–1256, 1993.

[52] R. Lindken, M. Rossi, S. Grosse, and J. Westerweel. Micro-particle image velocimetry (μPIV): Recent developments, applications, and guidelines. *Lab on a Chip*, 9:2551–2567, 2009.

[53] X. Hu, S. N. Wang, and L. J. Lee. Single-molecule DNA dynamics in tapered contraction-expansion microchannels under electrophoresis. *Physical Review E*, 79:041911, 2009.

[54] P. G. de Gennes. Molecular individualism. *Science*, 276:1999–2000, 1997.

[55] T. T. Perkins, D. E. Smith, R. G. Larson, and S. Chu. Stretching of a single tethered polymer in a uniform flow. *Science*, 268:83–87, 1995.

[56] D. E. Smith, T. T. Perkins, and S. Chu. Dynamical scaling of DNA diffusion coefficients. *Macromolecules*, 29:1372–1373, 1996.

[57] W. B. Russel, D. A. Saville, and W. R. Schowalter. *Colloidal dispersions*. Cambridge University Press, Cambridge, 1989.

[58] B. J. Yoon and S. Kim. Electrophoresis of spheroidal particles. *Journal of Colloid and Interface Science*, 128:275–288, 1989.

[59] M. Doi and S. F. Edwards. *The theory of polymer dynamics*. Oxford University Press, 1986.

[60] C. Bustamante, J. F. Marko, E. D. Siggia, and S. Smith. Entropic elasticity of lambda-phage DNA. *Science*, 265:1599–1600, 1994.

[61] J. F. Marko and E. D. Siggia. Stretching DNA. *Macromolecules*, 28:8759–8770, 1995.

[62] J. E. Butler, O. B. Usta, R. Kekre, and A. J. C. Ladd. Kinetic theory of a confined polymer driven by an external force and pressure-driven flow. *Physics of Fluids*, 19:113101, 2007.

[63] T. T. Perkins, D. E. Smith, and S. Chu. Single polymer dynamics in an elongational flow. *Science*, 276:2016–2021, 1997.

[64] H. C. Berg. *E. coli in motion*. Springer-Verlag, New York, 2004.

[65] N. C. Darnton, L. Turner, S. Rojevsky, and H. C. Berg. On torque and tumbling in swimming escherichia coli. *Journal of Bacteriology*, 189(5):1756–1764, 2007.

[66] H. C. Berg. The rotary motor of bacterial flagella. *Annual Review of Biochemistry*, 72:19–54, 2003.

[67] L. Turner, W. S. Ryu, and H. C. Berg. Real-time imaging of fluorescent flagellar filaments. *Journal of Bacteriology*, 182(10):2793–2801, 2000.

[68] J. Lighthill. Helical distributions of stokeslets. *Journal of Engineering Mathematics*, 30:35–78, 1996.

[69] A. P. Berke, L. Turner, H. C. Berg, and E. Lauga. Hydrodynamic attraction of swimming microorganisms by surfaces. *Physical Review Letters*, 101:038102, 2008.

[70] P. T. Underhill, J. P. Hernandez-Ortiz, and M. D. Graham. Diffusion and spacial correlations in suspensions of swimming particles. *Physical Review Letters*, 100:248101, 2008.

[71] A. Najafi and R. Golestanian. Simple swimmer at low reynolds number: Three linked spheres. *Physical Review E*, 69:062901, 2004.

[72] C. M. Pooley, G. P. Alexander, and J. M. Yeomans. Hydrodynamic interaction between two swimmers at low reynolds number. *Physical Review Letters*, 99:228103, 2007.

[73] M. Ramia, D. L. Tullock, and N. Phan-Thien. The role of hydrodynamic interaction in the locomotion of microorganisms. *Biophysical Journal*, 65:755–778, 1993.

[74] E. Lauga, W. R. DiLuzio, G. M. Whitesides, and H. A. Stone. Swimming in circles: Motion of bacteria near solid boundaries. *Biophysical Journal*, 90:400–412, 2006.

[75] T. Ishikawa, G. Sekiya, Y. Imai, and T. Yamaguchi. Hydrodynamic interactions between two swimming bacteria. *Biophysical Journal*, 93:2217–2225, 2007.

[76] S. Chattopadhyay, R. Moldovan, C. Yeung, and L. Wu. Swimming efficiency of bacterium escherichia coli. *Proc. Natl. Acad. Sci. USA*, 103(37):13712–13717, 2006.

[77] H. Flores, E. Lobaton, S. Mendez-Diez, S. Tlupova, and R. Cortez. A study of bacterial flagellar bundling. *Bulletin of Mathematical Biology*, 67:137–168, 2005.

[78] P. D. Frymier, R. M. Ford, H. C. Berg, and P. T. Cummings. Three-dimensional tracking of motile bacteria near a solid planar surface. *Proc. Natl. Acad. Sci. USA*, 92:6195–6199, 1995.

[79] W. R. DiLuzio, L. Turner, M. Mayer, P. Garstecki, D. B. Weibel, and H. C. Berg. Escherichia coli swim on the right-hand side. *Nature*, 435:1271–1274, 2005.

[80] C. Hsieh, S. Jain, and R. G. Larson. Brownian dynamics simulations with stiff finitely extensible nonlinear elasic-fraenkel springs as approximations to rods in bead-rod models. *Journal of Chemical Physics*, 124:044911–044920, 2006.

[81] H. Bekker, H. J. C. Berendsen, and W. F. van Gunsteren. Force and virial of torsional-angle-dependent potentials. *Journal of Computational Chemistry*, 16:527–533, 1995.

[82] S. P. Holleran and R. G. Larson. Using spring repulsions to model entanglement interactions in brownian dynamics simulations of bead-spring chains. *Rheologica Acta*, 47:3–17, 2008.

[83] M. Manghi, X. Schlagberger, and R. R. Netz. Propulsion with a rotating elastic nanorod. *Physical Review Letters*, 96:068101, 2006.

[84] E. M. Purcell. Life at low reynolds number. *American Journal of Physics*, 45:3–11, 1977.

[85] N. Hoda and S. Kumar. Brownian dynamics simulations of polyelectrolyte adsorption in shear flow with hydrodynamic interaction. *Journal of Chemical Physics*, 127:234902–234916, 2007.

[86] S. Kim and S. J. Karrila. *Microhydrodynamics: Principles and Selected Applications*. Butterworth-Heinemann, Stoneham, 1991.

[87] D. Bray. *Cell movements: from molecules to motility*. Garland, NewYork, 2nd edition edition, 2001.

[88] M. Polin, I. Tuval, K. Drescher, J. P. Gollub, and R. E. Goldstein. Chlamydomonas swims with two "gears" in a eukaryotic version of run-and-tumble locomotion. *Science*, 325:487–490, 2009.

[89] R. Stocker and W. M. Durham. Tumbling for stealth? *Science*, 325:400–402, 2009.

[90] N. Watari and R. G. Larson. Shear-induced chiral migration of particles with anisotropic rigidity. *Physical Review Letters*, 102:246001, 2009.

[91] V. B. Putz and J. M. Yeomans. Hydrodynamic synchronisation of model microswimmers. *Journal of Statistical Physics*, 137:1001, 2009.

[92] R. Golestanian and A. Ajdari. Analytic results for the three-sphere swimmer at low reynolds number. *Physical Review E*, 77:036308, 2008.

[93] M. Makino and M. Doi. Migration of twisted ribbon-like particles in simple shear flow. *Physics of Fluids*, 17:103605, 2005.

[94] M. Makino, L. Arai, and M. Doi. Shear migration of chiral particle in parallel-disk. *Journal of the Physical Society of Japan*, 77(6):064404, 2008.

[95] M. Kostur, M. Schindler, P. Talkner, and P. Hanggi. Chiral separation in microflows. *Physical Review Letters*, 96:014502, 2006.

[96] H. Noguchi and G. Gompper. Fluid vesicles with viscous membranes in shear flow. *Physical Review Letters*, 93:258102, 2004.

[97] H. A. Stone. Dynamics of drop deformation and breakup in viscous fluids. *Annual Reviews in Fluid Mechanics*, 26:65, 1994.

[98] M. R. Kennedy, C. Pozrikidis, and R. Skalak. Motion and deformation of liquid drops, and the rheology of dilute emulsions in simple shear flow. *Computer and Fluids*, 23:251, 1994.

[99] R. B. Bird, C. F. Curtis, R. C. Armstrong, and O. Hassager. *Dynamics of Polymeric Liquids. Volume 2: Kinetic Theory, 2nd ed.* Wiley-Interscience, New York, 1987.

[100] K. Nagasaka and H. Yamakawa. Dynamics of weakly bending rods: A trumbbell model. *Journal of Chemical Physics*, 83:6480, 1985.

[101] M. Solymosi and R. J. Low. A generalized scaling of a chiral index for molecules. *Journal of Chemical Physics*, 116(22):9875, 2002.

[102] K. H. Roh, D. C. Martin, and J. Lahann. Biphasic janus particles with nanoscale anisotropy. *Nature Materials*, 4:759, 2005.

[103] K. H. Roh, D. C. Martin, and J. Lahann. Triphasic nanocolloids. *Journal of the American Chemical Society*, 128:6796, 2006.

[104] C. W. J. Beenakker. Ewald sum of the rotne-prager tensor. *Journal of Chemical Physics*, 85:1581–1582, 1986.

[105] Christian F. Schmid, Leonard H. Switzer, and Daniel J. Klingenberg. Simulations of fiber flocculation: Effects of fiber properties and interfiber friction. *Journal of Rheology*, 44:781–809, 2000.